Materials Science in Additive Manufacturing

eISSN: 2810-9635

Volume 3 Issue 1, March 2024

ACCSCIENCE PUBLISHING

ACCSCIENCE PUBLISHING

Materials Science in Additive Manufacturing

Online ISSN: 2810-9635

Materials Science in Additive Manufacturing aims to bridge the cutting-edge research between additive manufacturing and the entire spectrum of materials science. The journal covers all applied and fundamentals of processing, synthesis, structure, composition, properties and performance of materials designed or manipulated for additive manufacturing. The journal covers a wide scope of innovative techniques, processes, methods, and applications.

About the Publisher

AccScience Publishing is a publishing company based in Singapore. We publish a range of high-quality, open-access, peer-reviewed journals and books from a broad spectrum of disciplines.

Contact Us

Managing Editor
msam.office@accscience.sg

AccScience Publishing
8 Burn Road, #15-03 Trivex, Singapore 369977.

Volume 3 • Issue 1 • March 2024
ISSN 2810-9635 (online)

MATERIALS SCIENCE IN ADDITIVE MANUFACTURING

Editor-in-Chief

Chee Kai Chua

Singapore University of Technology and Design, Singapore

ACCSCIENCE PUBLISHING

MATERIALS SCIENCE IN ADDITIVE MANUFACTURING

ISSN: 2810-9635 (online)

Editorial and Production Credits

Publisher: AccScience Publishing
Managing Editor: Ginger Lv
Editorial Assistant: Flora Kang
Production Editor: Chi Tat Poon
Article Layout and Typeset: Sinjore Technologies (India)
Cover Design: BUTTON GRAPHIC DESIGN STUDIO (Malaysia)

For all advertising queries, contact msam.office@accscience.sg.

Supplementary file

Supplementary files of articles can be obtained at https://accscience.com/journal/MSAM/3/1.

About the Cover

Directed energy deposition in progress

Disclaimer

AccScience Publishing is not liable to the statements, perspectives, and opinions contained in the publications. The appearance of advertisements in the journal shall not be construed as a warranty, endorsement, or approval of the products or services advertised and/or the safety thereof. AccScience Publishing disclaims responsibility for any injury to persons or property resulting from any ideas or products referred to in the publications or advertisements. AccScience Publishing remains neutral with regard to jurisdictional claims in published maps and institutional affiliations.

Material Science in Additive Manufacturing

Editorial Board

ACCSCIENCE PUBLISHING

Volume 3 | Issue 1 | March 2024 |

Materials Science in Additive Manufacturing

https://accscience.com/journal/msam

CONTENTS

ACCSCIENCE PUBLISHING

Materials Science in Additive Manufacturing

REVIEW ARTICLE

Porous titanium alloys for medical application: Progress in preparation process and surface modification research

Binghao Wang[1,2], Miao Luo[1,2], Zheng Shi[3], Yuwei Cui[4], Yuting Lv[3], Chengliang Yang[1,2,4]*, and Liqiang Wang[4,5]*

[1]Life Sciences and Clinical Medicine Research Centre, Affiliated Hospital of Youjiang Medical University for Nationalities, Baise, Guangxi, China

[2]Guangxi Key Laboratory for Preclinical and Translational Research of Bone and Joint Degenerative Diseases, Guangxi Biomedical Materials Engineering Research Center for Bone and Joint Degenerative Diseases, Baise, Guangxi, China

[3]College of Mechanical and Electronic Engineering, Shandong University of Science and Technology, Qingdao, Shandong, China

[4]State Key Laboratory of Metal Matrix Composites, Shanghai Jiao Tong University, Shanghai, China

[5]National Center for Translational Medicine, Shanghai Jiao Tong University, Shanghai, China

Abstract

Excellent mechanical properties and biocompatibility are the most sought-after attributes in biomedical materials for the regeneration of damaged tissues. However, conventional dense titanium alloys possess a modulus significantly higher than that of human tissues, leading to potential stress-shielding effects. Medical porous titanium alloys can reduce the elastic modulus of the material, promote tissue fixation and vascular regeneration, and improve the suitability for human tissue properties. With the continuous development of technology, the preparation process of porous titanium alloys has undergone a series of multifaceted transformations and improvements in the aspects of powder sintering, fiber preparation, and additive manufacturing processes, and its structural characteristics and mechanical properties are constantly evolving in a controllable direction. Alongside the enhancement of the material's mechanical properties through porous design, optimization of the properties at the implant-tissue interface also leads to improved antimicrobial and osteogenic properties of porous titanium. Due to the complex internal structure of porous titanium alloys, surface modification is mainly carried out in fluid media, which is realized by morphological modification and the introduction of functional substances. Over time, the surface modification of porous titanium alloys for medical applications has progressed from morphological modification and introduction of chemical composition to the loading of bioactive substances. This evolution aims to enhance safety and efficiency in the use of these materials. This paper reviews the preparation and surface modification processes of porous titanium alloys for medical use and summarizes the advantages, disadvantages, and influencing factors among different processes, with a view to providing new ideas for the development of porous implants for medical use.

Keywords: Medical implants; Porous titanium alloy; Preparation process; Surface modification

***Corresponding authors:**
Chengliang Yang
(stbyyl@126.com)
Liqiang Wang
(Wang_liqiang@sjtu.edu.cn)

Citation: Wang B, Luo M, Shi Z, *et al*. Porous titanium alloys for medical application: Progress in preparation process and surface modification research. *Mater Sci Add Manuf*. 2024;3(1):2753. doi: 10.36922/msam.2753

Received: January 16, 2024

Accepted: March 8, 2024

Published Online: March 28, 2024

1. Introduction

Millions of people around the world suffer from incurable injuries due to infection debridement, cardiovascular and cerebrovascular diseases, degenerative orthopedic diseases, and oral and maxillofacial diseases every year, posing a huge socio-economic burden on society and the health-care system.[1] Biomedical materials, which are used in fixing, supporting, and repairing damaged parts, are key players in moving medical advancements forward. As clinical product technology and quality requirements continue to improve, there is a growing demand for biomedical materials that are cost-effective, of higher quality, and can be processed more conveniently.

According to the type of material, biomedical materials can be divided into metal materials,[2] ceramic materials,[3] and polymer materials.[4] Among them, metal materials have many excellent properties, such as high strength, good wear resistance, and easy processing, occupying 70 – 80% of the entire market share of medical materials.[5] Commonly used medical metal materials include titanium and titanium alloy, stainless steel, nickel-cobalt alloy, and magnesium alloy.[6] Titanium and its alloys have the advantages of high strength and low modulus, high fatigue performance, and excellent biocompatibility, attributes that make them the most widely used medical metal materials for being able to meet most medical needs.[7]

However, it is found that titanium alloy as an endoprosthesis is prone to loosening when it has been implanted in the human body for a long period of time.[8] The loosening occurs due to two major factors: (i) Dense titanium and titanium alloys have high elastic modulus compared with human bone/tissue, which will cause a "stress shielding" effect;[7] (ii) traditional titanium and titanium alloys are bioinert metal materials, and implants cannot form a good biological fixation with the surrounding tissues of the human body.[9]

To address the above clinical problems, researchers integrated three-dimensional (3D) porous structures into titanium alloy implants to effectively reduce the elastic modulus of implants, reduce the "stress shielding" effect, and improve the bonding strength between implants and human tissues.[10] Therefore, porous titanium has been used as a promising new biomedical material for artificial joints, spinal fusion devices, dental implants, and cardiovascular scaffolds and in other fields.[11]

However, introducing a porous structure to reduce the modulus alone cannot alter the bioinert nature of titanium alloy, which still lacks the capacity to promote cell adhesion, tissue differentiation, and bacterial suppression.[12] To enhance the biological performance of porous titanium scaffolds, it is crucial to improve the physicochemical properties at the interface between the scaffold and the surrounding tissue. Surface modification technology is a method to change the surface properties of materials by physical or chemical means, which plays an important role in the functional transformation of titanium alloys.[13]

Medical porous titanium alloy implants have gradually emerged as a critical ingredient in the orthopedic, stomatologic, cardio-cerebrovascular, and other fields. Researchers have focused on improving the mechanical and biological properties of materials by optimizing the preparation process and surface modification process.[14,15] Despite the continuous technological advancements, there is still a lack of comprehensive and in-depth summary in the field of processing and surface modification of medical porous titanium alloys, especially about (i) the complexity of the preparation process of porous scaffolds and the comparison of advantages and disadvantages; (ii) the application scenarios and influencing factors of various surface modification methods; and (iii) the synergistic effect between the preparation method of porous structure and the surface modification. This paper aims to provide a timely, comprehensive, and critical review of the preparation and surface modification of medical porous titanium alloy scaffolds. The overall content of the paper is shown in Figure 1. The paper first outlines the performance requirements, structural requirements, and influencing factors of the medical titanium alloy porous scaffold (Section 2). Then, the preparation methods of porous scaffolds and their advantages and disadvantages

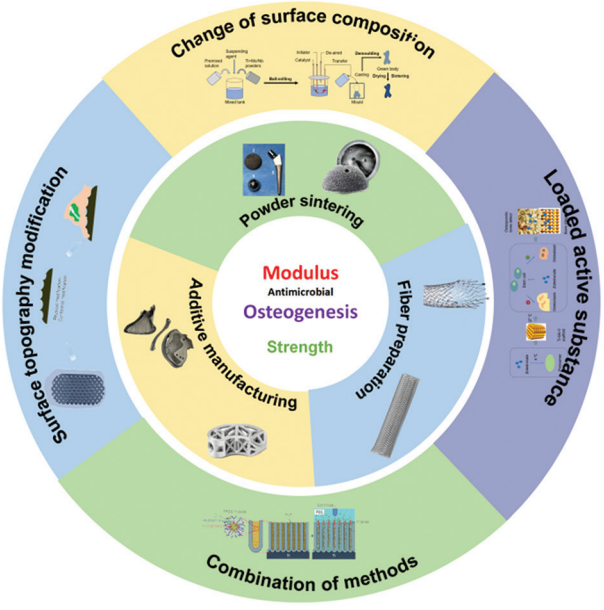

Figure 1. Overview of performance requirements preparation processes, and modification methods for medical porous titanium implants.[2]

are introduced (Section 3). Subsequently, the current surface modification methods of medical porous titanium alloys are reviewed (Section 4), and finally, the future development direction is summarized (Section 5).

2. Performance requirements and influencing factors of porous titanium alloy

Compared with the external environment, the physical and chemical environments of various tissues and organs in the human body are vastly different from each other and in a complex and dynamic state.[16] To ensure durable functionality, human bones must be able to withstand pressure, tension, and other load changes encountered in daily life. After being implanted in the human body, more stable metal materials are also prone to corrosion, wear, fatigue fracture, and other failures. Therefore, higher requirements are put forward for porous titanium alloys in clinical practice, and ideal titanium implants should have mechanical properties, morphology, structure, and physical and chemical properties similar to those of the human body.[17]

2.1. Performance requirements of porous titanium alloys

Porous titanium alloys must fulfill the necessary functions or specific requirements in tissue engineering. In these standards, mechanical properties such as strength, elastic modulus, and flexibility are the basic requirements for maintaining structural function and durability.[18] Considering the influence of different parts and age factors, the strength of human bone ranges from 33 to 193 MPa, and its modulus is between 0.3 and 30 GPa.[19] To qualify as a medical metal material, its properties should fall within the above-mentioned ranges.

Biocompatibility is also an essential variable guaranteeing the function of porous titanium.[20] Porous titanium alloy's biological properties are mainly reflected in two aspects: (i) The material is non-toxic and will not cause local or systemic immune reactions and (ii) it can promote intracellular protein expression and accelerate tissue recovery and growth.[21]

Wear and corrosion resistance play a decisive role in the lifespan of joint implants.[22] Low wear resistance will produce extremely severe wear, causing loosening of the fit. In addition, metal particles generated by wear or metal ions generated by corrosion will also lead to adverse reactions in the cellular organization. Therefore, titanium alloy materials must have excellent wear resistance.

2.2. Structural characteristics of porous titanium alloys

Human bones, teeth, and other tissues and organs are graded porous structures. Changes in pore characteristics (porosity, specific surface area) will cause changes in permeability, fluid shear force, cushioning energy absorption, and other properties, thus affecting cell adhesion, migration, and tissue growth.[23] In addition, pore characteristics also affect the transport of nutrients, the exchange of oxygen, and the removal of metabolites within the cell tissue.[24] Therefore, the bionic porous design of porous titanium alloys is also one of the requirements.

In addition to the internal structure, surface morphology and roughness have a significant effect on cell adhesion and bone mineralization. Studies have shown that the roughness range of 1 – 10 μm can promote the mineralization reaction and mineralization of bone tissue in the implant[25] and improve protein adsorption, osteoblast adhesion, and the healing rate of the peripheral area outside the implant. Therefore, it is important to explore the suitable surface morphology to enhance the bonding of the implant with the tissue to improve the biocompatibility of porous implants.

2.3. Factors affecting the properties of porous titanium alloys

The composition and type of titanium alloy are the primary factors affecting its performance. Pure titanium is the earliest form of material used in making titanium alloy, but its modulus can reach as high as 110 GPa; TC4 is the second most widely used material after pure titanium due to its low cost, but it can precipitate Al/V elements in the human body for a long time, jeopardizing the human nervous system.[26] Therefore, β titanium alloys with lower modulus and less toxicity are gradually emerging, and β phases with lower modulus are formed inside titanium alloys by adding biological elements such as Nb, Ta, and Zr.[27] At present, the modulus of TiNbTaZr, TiNbZr, and other materials has been reduced to 50 GPa, with high strength and, low mode characteristics and good biocompatibility.[28] Developing new materials can improve the performance of implants from the source. Still, the development and application of new materials are restricted by their high development cost, long cycle, and minor performance adjustment range.

Compared with the research and development of new materials, optimizing the preparation process and structural design of existing materials is a more efficient pathway to material enhancement. Especially when coinciding with the rise of the additive manufacturing process, the mechanical properties of materials can be significantly adjusted to our favor, and an optimized structural design can help realize the precise regulation of porous titanium alloys. These procedures could constitute a systematic structural design method. The strength, modulus, and other properties of porous titanium can be directly adjusted by changing the

design factors of porous implant unit structure, pore size, porosity, and pore distribution.[29]

The material's surface is in direct contact with cells and tissues, and the surface properties are related to the interface bonding between materials and tissues. In addition, surface roughness or morphology and element release directly affect gene expression and protein synthesis inside cells. Therefore, surface properties are important factors affecting the biocompatibility of porous titanium alloys.[30] Figure 2 summarizes the performance requirements of porous titanium alloys and the relationship between them and the influencing factors. It is clear that material development, structural morphology, and surface properties are the three key factors affecting the mechanical and biological properties of porous titanium alloys.

3. Preparation process of porous titanium alloy

According to the analysis in Section 2, the structure is one of the direct factors affecting the properties of porous titanium alloys, and the preparation process is the key to determining the structural properties. Different methods exert different influences on the degree of melting, internal microstructure, pore size, and distribution of titanium alloy powder and thus affect its modulus, strength, and other mechanical properties.[31] In this section, the processing methods of porous titanium are divided into the powder sintering method,[32] fiber fabrication method,[33] and additive manufacturing method,[34] according to the state of raw materials and processing principles, and the advantages and disadvantages of different processes are compared and analyzed.

3.1. Sintering method

3.1.1. Powder sintering method

The powder sintering method uses metal powder as raw material, which is a preparation method to melt and bond the powder surface through compaction, sintering, and other processes to obtain porous metal[35] (Figure 3A). The structure and mechanical properties of porous titanium alloys obtained by this process are affected by sintering temperature, time, pressure, powder composition/particle size, and other factors.[36]

Oh *et al.*[37] studied the effect of powder diameter on porous titanium's morphology and mechanical properties. By controlling the sintering conditions and the particle size of titanium powder (65 μm, 189 μm, and 374 μm), the medical porous titanium alloy with a porosity of 5.0 – 37.1% was prepared (Figure 3B and C). The mechanical test results show that the larger the powder diameter is, the lower the modulus of the porous material is at the sintering temperature of 1173°C and the sintering pressure of 10 MPa. The main reason is that the pores of the large-diameter powder are larger and difficult to close during the sintering process, and thus, the resulting material has a higher porosity. In addition to powder properties, temperature sintering is also an essential factor affecting the mechanical properties of sintered porous titanium. Torres *et al.*[38] sintered titanium powder at 1000°C for 40 min to obtain porous titanium with a porosity of 41.5%, a strength of 480 MPa, and a modulus of about 10 GPa. Later, they increased the sintering temperature to 1100°C and found that the material's porosity decreased to 34.6%, the strength increased to 560 MPa, and the modulus increased to 20 GPa. These parameter changes indicate the conformance to the law of material molding. The increase in sintering temperature promotes the melting of the powder, making the pores of the material isolated, thereby resulting in the reduction of porosity, and the improvement of material density leads to the enhancement of its mechanical properties.

In addition to controlling the traditional melting temperature and powder, the discharge plasma sintering

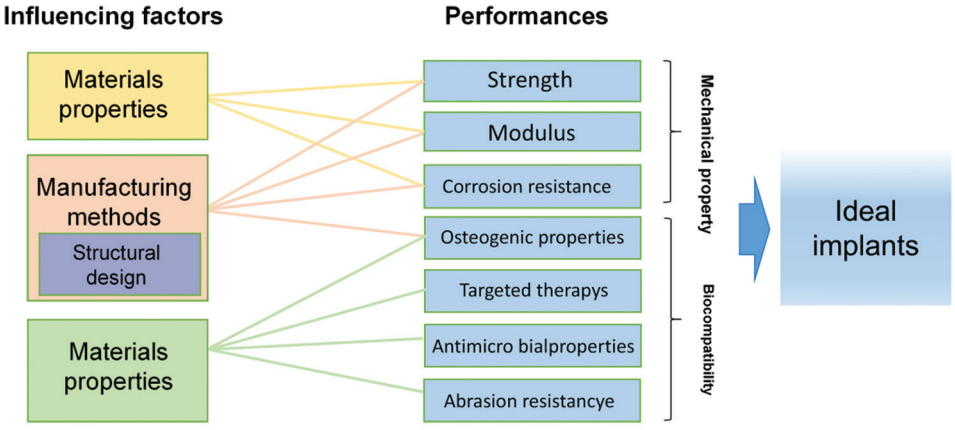

Figure 2. Relationship between properties of medical porous materials and influencing factors.

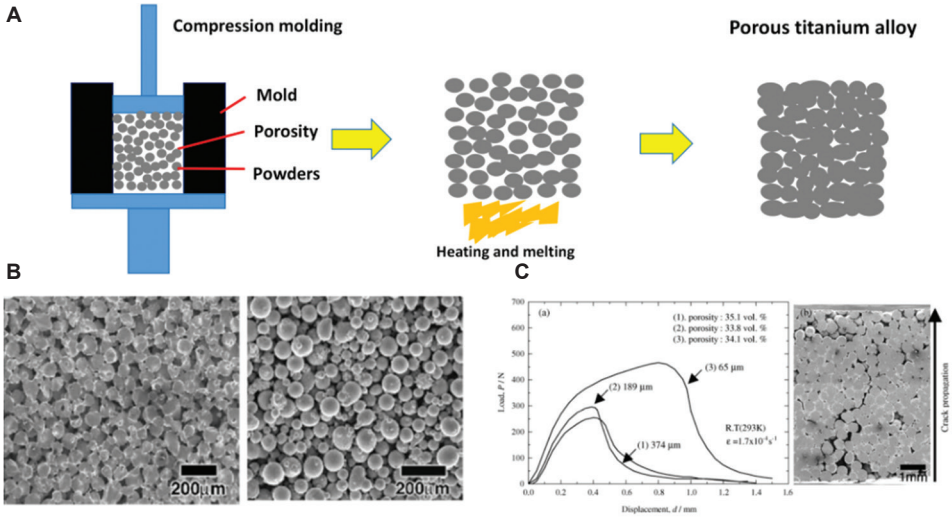

Figure 3. Powder sintering process and sample properties. (A) Schematic diagram of porous scaffold prepared by powder sintering method. (B) Scanning electron microscopy image of titanium alloy powder before and after sintering. (C) Sample compression properties after sintering.[37] Copyright © 2003 Elsevier. Reprinted with permission from Elsevier.

method has become an important preparation process for porous titanium alloys due to its advantages of low sintering temperature, sintering time, and high processing efficiency. Annur *et al.*[39] used spark plasma sintering (SPS) processing to sinter porous titanium with porosities ranging from 4.2% to 27.5% at 600 – 800°C. The porous titanium was obtained by using the SPS process. The modulus of elasticity of the obtained porous titanium was 13.6 – 24.4 GPa, which is close to that of human bone (0.3 – 30 GPa). The self-propagating high-temperature synthesis method is a kind of powder sintering method. In this method, the heat released by the chemical reaction of the powder itself spontaneously and continuously spread through all the reactants in the form of a combustion wave,[40] resulting in a high reaction rate and high-temperature gradient, and the crystal lattice of the prepared material produces high-density defects to form a porous structure. This method is suitable for the preparation of NiTi porous titanium.

The powder sintering method is the main method for preparing porous metal implants in the early stage because of its low cost, simple operation, and the low requirement on powder parameters such as powder sphericity and particle size.[41] However, the porosity and pore size of the porous titanium alloy obtained by this method are mainly affected by the properties of the powder (melting point, particle size, *etc.*). The porosity of the sintered scaffold is up to 50%, and the shape of the pores is small and irregular. In addition, porous titanium sintered by powder has poor toughness and is prone to crack propagation under low-stress conditions.[42]

3.1.2. Foaming method

The process of preparing porous titanium alloy using the foaming method involves adding a blowing agent to the metal powder and ensuring thorough mixing. On heating, a chemical reaction or a sudden change in pressure triggers the blowing agent to release gas, causing expansion and overflow during the metal melting process, thus creating a porous structure. Foaming agents are mainly divided into solid foaming, slurry foaming, and vacuum foaming (Figure 4A and B). Its properties are affected by factors such as the type of foaming agent, temperature, and time.[43]

Chen *et al.*[44] used pure titanium with an average particle size of 38 μm as raw material, mixed sodium carboxymethyl cellulose (CMC), sodium hexametaphosphate (SHMP), and hydrogen peroxide solution as a binder, dispersant, and blowing agent; the sample was stirred and dried at room temperature and heated in a vacuum atmosphere to 1300°C for 3 h. By adjusting the hydrogen peroxide content, the porous titanium with porosity of 48%, 64%, and 76% (Figure 4C) was obtained, its strength was between 78 and 235 MPa, and the corresponding modulus was 1.3 – 4.2 GPa. Rao *et al.*[45] prepared porous Ti-Nb-Zr alloys with porosity ranging from 6.06% to 62.8% by mixing TiH_2, Nb, and Zr powders with 0 – 50% NH_4HCO_3 and controlling the content of Nb and Zr and the sintering temperature. The hardness of porous titanium alloys is between 290 and 63 HV, the compressive strength is between 1530.5 and 73.4 MPa, and the elastic modulus is between 10.8 and 1.2 GPa. During the foaming process, vibration or stirring can improve the uniformity of foaming. Ahn *et al.*[46] mixed titanium hydride powder with nonionic

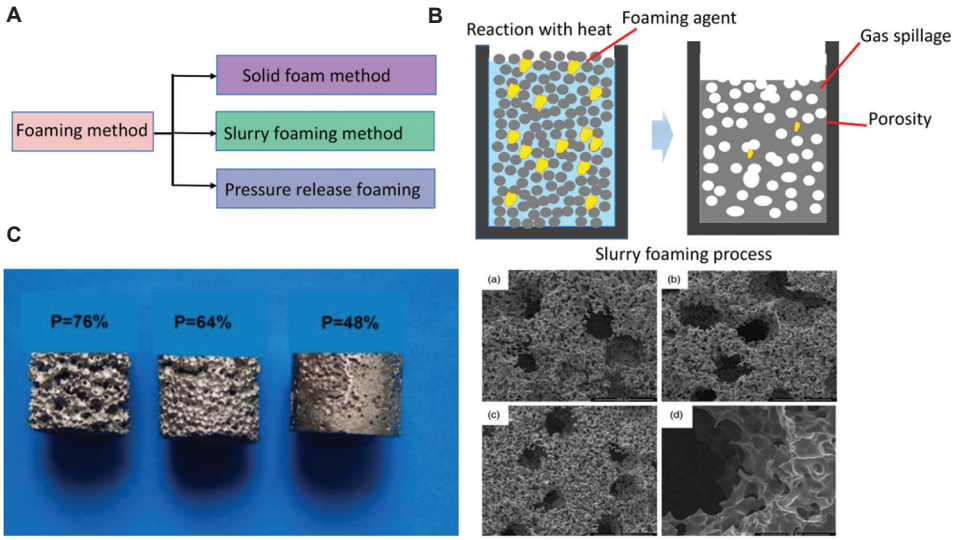

Figure 4. Classification of the foaming method and the morphology of the prepared samples. (A) Classification of slurry foaming method. (B) Principle of preparation of porous titanium alloy by foaming method. (C) Porous titanium with different porosity obtained by the slurry foaming method and its microstructure.[44] Copyright © 2009 Elsevier. Reprinted with permission from Elsevier.

surfactant (Hypermer KD-6) and poly(vinyl alcohol) (PVA) to form TiH2 suspension, which was poured into a mold after creating a large number of bubbles inside the suspension by mechanical stirring, and sintered at 1400°C for 2 h to obtain porous scaffolds with 83% porosity, with a strength of 8.9 ± 1.6 MPa.

The foaming process is simple, rapid, and low-cost. However, it is challenging to ensure a pore uniformity in the porous material prepared by this process, and the material is also prone to crack and fatigue damage. In addition, if the material is used as a medical porous implant, the residual blowing agent may enter and harm the human body. Therefore, this method is predominantly used for the preparation of porous structures of low-density materials such as polymer compounds.[47]

3.1.3. Space holder technique

The space holder method mixes the metal powder and pore-forming agent in proportion, prepares the precursor under certain conditions for sintering, and removes the pore-forming agent in the sintering process to obtain porous metal materials. Commonly used pore-forming agents include hydride, carbide, magnesium, and sodium chloride.[31]

Pore-forming agents' shape, content, and distribution are the main factors affecting the pore characteristics. As shown in Figure 5A, Haghjoo *et al.*[48] used urea and cubic sodium chloride (SC) of two different forms (NU and SU) as pore-making agents, which were mixed with TiH_2 and compacted under a load of 120 MPa. After the urea was removed at 200°C, the porous titanium scaffold was prepared at 1000°C. After sintering, NaCl was removed by soaking the scaffold in warm water for 24 h, and the porosity of the prepared scaffold was about 64%. Mechanical tests showed that the strength of porous titanium with different pore shapes varied between 230 and 340 MPa, and the modulus was between 3.78 and 6.32 GPa. The results of cell proliferation experiments *in vitro* showed that the roughness and high surface area provided by acute angle in Ti/NU and Ti/SC samples significantly improved the cell viability of the samples. Compared with titanium alloy, magnesium metal is degradable in the human body, has better biocompatibility, and has a significant difference in physical properties from titanium metal, so it is also used as one of the pore-making materials. Luo *et al.*[49] used magnesium powder, magnesium particles, and titanium powder as pore-making agents (Figure 5B), mixed titanium powder with magnesium powder/particles and ethanol adhesive, pressurized the sample to form at 400 MPa, heated the sample at 60°C to remove ethanol, and finally heated the sample slowly to 1150°C for 4 h to remove magnesium powder and complete sintering. Porous titanium with a 35 – 65% porosity was obtained, as shown in Figure 5C. Mechanical experiments showed that its strength and Young's modulus were 22 – 126 MPa and 0.063 – 1.18 GPa, respectively. In addition to organic substances and metals, $CaCl_2$ in inorganic substances is also one of the pore-making agents. Yang *et al.*[50] mixed Ti_2O_3 and calcium chloride powder with different contents into cylindrical preforms. It was then transferred into the crucible, and the bottom was placed with metallic

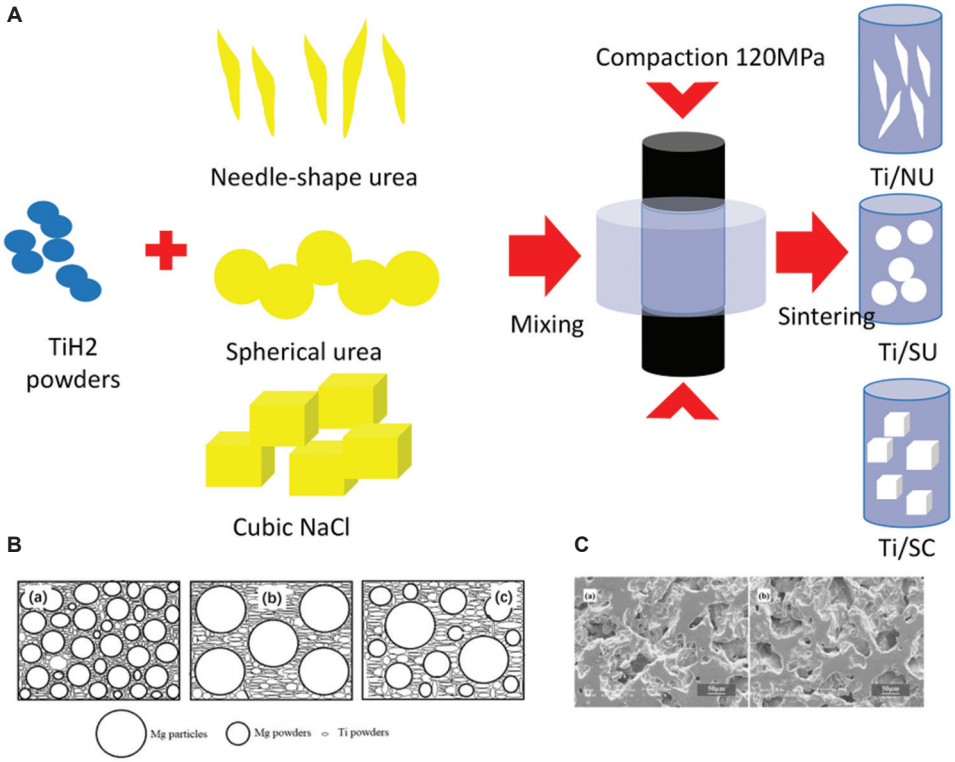

Figure 5. Principle and shape of space holder method. (A) Scanning electron microscopy images of two different shapes of urea NaCl and schematic diagram of porous titanium preparation. (B) Schematic diagram of preparing porous titanium alloy using magnesium particles and magnesium powder as pore-forming agents. (C) Preparation of porous titanium alloy using magnesium particles and magnesium powder as pore-forming agents.[49]

calcium, which acts as a reducing agent. Porous titanium was prepared from calcium chloride volatilization by continuous heating at 1273 K under 0.1 Pa. Then, porous titanium with a porosity of 62 – 82% was prepared by leaching the reduction products with dilute hydrochloric acid, and more than 90% of the pores were open. The porosity gradually increased with calcium chloride content in the raw material.

Space scaffold technology can achieve a wide range of pore size adjustments and high porosity by controlling the mixing ratio and is one of the most commonly used methods for preparing porous materials.[51] However, the uniformity of the mixture is not easy to control, and the pore-forming agent needs to be removed by heating evaporation or soaking, which makes it easy to produce residual pore-forming agents and engender other problems affecting the material's biocompatibility.

3.1.4. Gel injection molding

The gel injection molding method involves mixing powder and adhesive, followed by injection molding and curing to obtain a uniform blank. After drying, dust removal, and sintering, the billets are prepared into nearly net porous titanium alloys with complex shapes.[52]

The advantage of the gel casting method is that it can design the overall appearance of porous materials according to the needs of the damaged parts. Yang *et al.*[53] used acrylamide, N-methylene diacrylamide, n-tetramethylenediamine (TEMED) as catalyst, ammonium persulfate hydrogel system, and titanium powder to prepare a premixed solution. The slurry was poured into a non-porous mold (Figure 6), kept at 60°C for 2 h to cure into the required shape, and dried in vacuum at room temperature after demolding. By changing the volume of the polymer network between the powder particles, 39 – 50% porous Ti-Mo and Ti-Nb alloy porous implants were prepared after sintering at 900 – 1050°C for 2 h, with Young's modulus ranging from 5 to 18 GPa.

Biasetto *et al.*[54] used gel casting to prepare porous Ti6Al4V metal by mixing titanium alloy powder with a surfactant to prepare suspension Doran molds for mechanical stirring to study the effect of stirring speed (700 rpm and 1500 rpm) on the evolution of porous titanium porosity morphology. At 700 r/min, the porous titanium porosity decreased from 91.3% to 81.3% at 700 r/min, and the porosity decreased from 88.3% to 70.7% at 1500 r/min. From the results, it clear that the increase in rotational speed decreases the bubble content

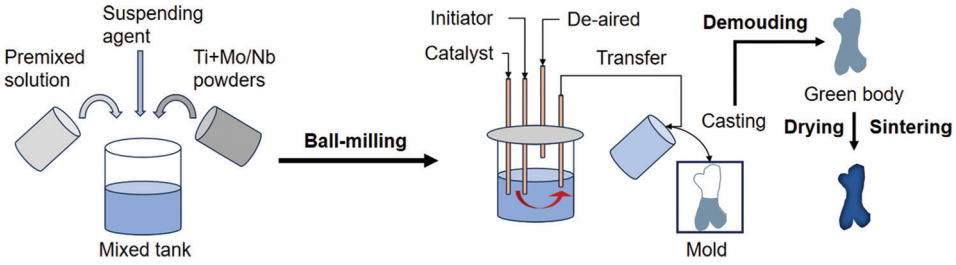

Figure 6. Schematic diagram of gel injection molding.

in the mixture, resulting in a reduction in porosity, with the compressive strength of the sintered samples ranging from 24.4±6.8 to 79.1±6.5 MPa.

Parts with high quality, complex shape, and uniform aperture distribution can be prepared by gel injection molding. The mold required by this process is inexpensive and is suitable for preparing large-size and high-precision porous medical implant materials.

3.2. Fiber braiding method

Fiber sintering refers to the technique of winding or arranging metal fibers into the desired structure and then placing them in a reducing atmosphere so that the contact points between the fibers are thoroughly combined and sintered to obtain porous titanium alloys. This method has been widely used in preparing cardiovascular scaffolds and titanium mesh.

The pore characteristics of metal fibers can be adjusted by changing the winding mode, length, diameter, and length-diameter ratio. Liu *et al.*[55] utilized a commercial pure titanium wire with a diameter of 0.27 mm as raw material, wound it along a rod with a diameter of 1.5 mm, and uniformly stretched the helical spring section prepared to maintain a particular pitch. The stretched coil spring wire was then wound together to form a pre-compacted sample, as shown in Figure 7A. Using bisphenol A glycyl methacrylate (BisGMA) as a binder, the free cross-wire nodes in wound porous titanium were fixed to enhance its strength, and the BisGMA-reinforced porous titanium material with a porosity of 40 – 55% was prepared. Its elastic modulus and yield strength were 0.4 – 1.4 GPa and 12.9 – 52.5 MPa, respectively. Wang *et al.*[56] took NiTi wire as raw material, used a mold to arrange NiTi regularly, and added Nb powder at the connection points of each cross line for sintering, forming a NiTi porous scaffold (Figure 7B). The strain of the elastic test scaffold reached 27%, and the remaining strain remained close to zero after unloading, showing good superelasticity. Li *et al.*[57] superimposed titanium mesh with different apertures (300 μm, 551 μm, 697 μm) layer by layer (Figure 7C) to produce porous titanium with an anisotropic structure. The Young's modulus and yield stress of porous titanium were 1 – 7.5 GPa and 10 – 110 MPa, respectively. The length-diameter ratio of titanium mesh affects the compression properties of porous titanium. A higher length-diameter ratio of the pore increases the Young's modulus and yield stress of titanium mesh.

Compared with the powder sintering method to prepare porous titanium, the product prepared by the fiber sintering method has better plasticity and impact resistance, and the porosity can reach more than 90%. The products prepared by this method have been widely used in cardiovascular and cerebrovascular scaffolds and other fields, but the prominent drawbacks lie in their shape limitations and the low bonding strength at the titanium wire connection in the complex service environment of the human body.

3.3. Additive manufacturing method

Additive manufacturing, also known as 3D printing, has the advantage of manufacturing medical implants quickly and accurately.[58] The products of which can not only achieve specific mechanical properties but also shape compatibility, which was otherwise not possible between traditional universal internal implants and the human body.[59] At present, the common methods for 3D-printing medical titanium alloys are selective laser sintering (SLS),[60] electron beam melting technology (EBM), selective laser melting technology (SLM), and direct ink writing (DIW) technology.[61]

3.3.1. SLS/EBM/SLM

As shown in Figure 8A and B, the principle of electron beam melting molding technology and selective laser sintering/melting technology is preparing a construct using melted metal powder in a layer-by-layer fashion using electron beam or laser as heat source in vacuum or inert gas environment.[62] The specific working process is as follows: pre-laying powder, high-energy electron beam/laser deflection after focusing on producing high energy, scanning the powder layer in a local small area to produce high temperature and even melting,[63] continuous scanning

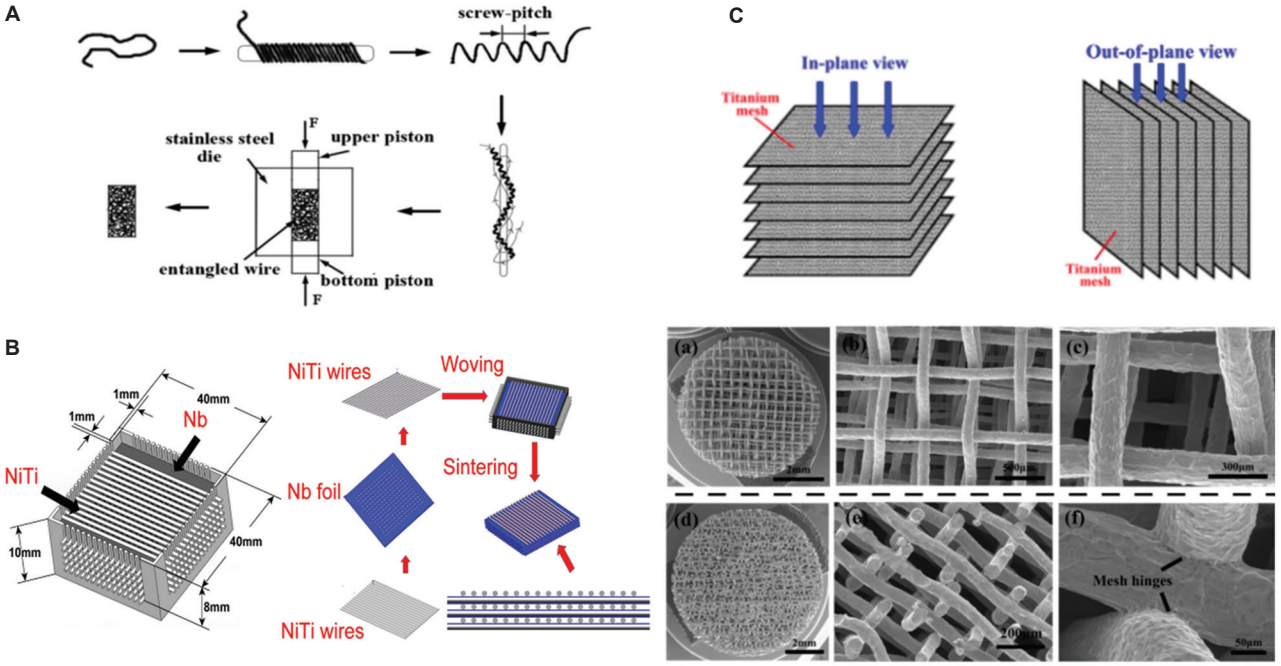

Figure 7. Preparation of porous titanium alloys using different fibre preparation methods. (A) Preparation of porous titanium by fiber winding method of titanium alloy.[55] Copyright © 2010 Elsevier. Reprinted with permission from Elsevier. (B) Schematic diagram depicting NiT titanium alloy wire eutectic reaction sintering of porous titanium. (C) Schematic diagram depicting titanium mesh superposition of porous titanium.[57] Copyright © 2015 Elsevier. Reprinted with permission from Elsevier.

by the heat source to produce energy to make the melt pool fuse and solidify, and connecting into linear and planar metal layers.[64] After finishing the layer, the powder-laying process is repeated until forming is completed.[65]

The process is mainly affected by laser power, spot diameter, hatch spacing, scanning speed, powder thickness, preheating temperature, and other parameters,[68] and the materials obtained by different processes exhibit different properties.[69] The processing principle of SLS is close to that of the powder sintering method, which mainly makes the powder surface melt and bond. However, compared with the traditional powder sintering method, SLS technology has more advantages in the preparation of macroscopic pores, and the porosity, pore size, and other structural parameters can be controlled better and faster. However, a notable disadvantage of this method is that the obtained material is of low strength.

EBM technology uses an electron beam as a heat source,[70] which has advantages in refractory metal additive manufacturing. In contrast, SLM has higher accuracy, which is suitable for preparing high-precision components.[71] Ataee *et al.*[72] studied *in vitro* biocompatibility of CP-Ti manufactured by SLM and Ti64 scaffolds fabricated by EBM and compared them with cast CP-Ti. The *in vitro* cell experiment results showed that the CP-Ti scaffold made by SLM had higher cell viability and cell adhesion density than the TC4 scaffold made by EBM. Then, the mechanical properties of CP-TI prepared by SLM and cast CP-Ti were tested, and the modulus of the porous scaffold prepared by SLM was lower. Due to the advantages of additive manufacturing technology in the preparation of complex porous structures, design methods involving the adjustment of parameters such as porosity, aperture, cell type, and structure size have gradually attracted the attention of researchers,[73] and porous structure design methods such as CAD structure,[74] medical imaging,[75] topology optimization,[76] and minimal surface[77] have been established.

The additive manufacturing method has significant advantages in the preparation of bionic porous implants. Lv *et al.*[78] prepared porous scaffolds with porosity varying along a radial gradient using SLM technique. The mechanical properties showed that the decrease in peripheral porosity could increase the moment of inertia of the porous implant and improve the bending and compression resistance of the material. In addition, the effect of porous unit variation on the mechanical properties has also been investigated.[79] The mechanical and permeability properties of the scaffolds are compromised when different units are combined. Overall, the additive manufacturing method is able to achieve precise control of the strength, modulus, and biological properties of the present porous implants with reduced material usage.[80]

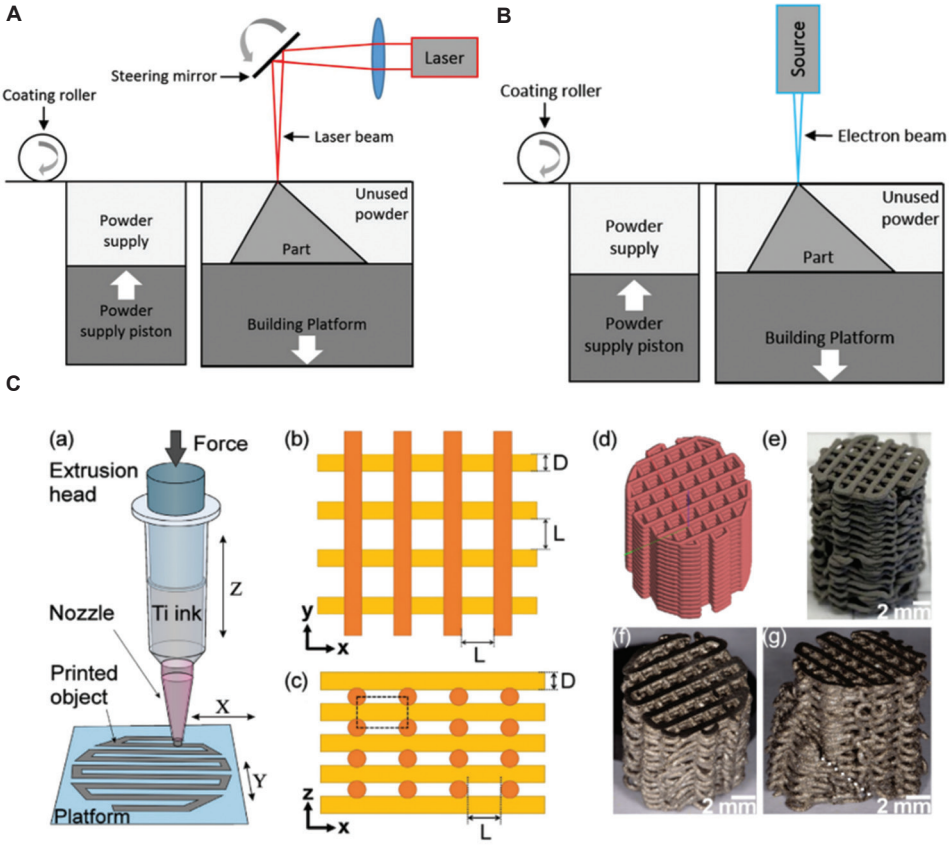

Figure 8. Different metal additive manufacturing processes. (A) Schematic diagram depicting the principle of preparation by laser selective melting. (B) Schematic diagram depicting the of processing principle of electron beam melting.[66] (C) Schematic diagram of direct writing ink technology.[67]

3.3.2. Direct ink writing technology

Direct ink writing technology is a new additive manufacturing molding process in which a suspension is prepared by mixing a metal powder material with a viscous fluid before printing. The suspension is then loaded into a printer and extruded through a nozzle for molding, and the extruded material is dried and sintered to form a 3D porous structure,[81] as shown in Figure 8C.

Zhao *et al.*[82] prepared porous Ta-Ti-Nb-Zr high-entropy alloy using DIW technology. By adjusting Zr content, porous titanium alloys with different properties were obtained, whose compressive strength increased from 70.08 to 149.95 MPa, and elastic modulus increased from 0.18 GPa to 0.64 GPa. To improve the molding accuracy of extruded materials, Li *et al.*[83] designed a photocurable-assisted technology to print porous Ti6Al4V alloys by DIW. Titanium alloy suspension with a powder content of 45% was prepared based on 1,6-hexanediol diacrylate monomer and trimethylolpropane triacrylate monomer (HDDA-TMPTA) photosensitive system. The extruded suspension was cured by ultraviolet irradiation, and the TC4 porous scaffold with 50% porosity was obtained after sintering, and its maximum compressive and buckling strengths were 60.47 and 106.8 MPa, respectively.

Compared with SLM and other technologies, DIW technology avoids the temperature gradient caused by laser and other heat sources and effectively reduces internal stress concentration, cracks, and other defects.[84] It can carry bio-friendly elements or drugs and has excellent potential in targeted therapy and osteogenic induction. However, this method is still fraught with problems of a single structure and low strength.[85]

Table 1 summarizes the advantages and disadvantages of different preparation processes for medical porous titanium scaffolds. The structural parameters and performance of porous titanium scaffolds prepared by different processes are summarized in Table 2.

4. Surface modification method of porous titanium alloy

The advances attained in porous titanium alloy, which has significantly reduced elastic modulus and improved

Table 1. Advantages and disadvantages of different preparation processes for medical porous titanium scaffolds

Technology	Principle	Advantages	Disadvantages	References
Sintering process				
Powder sintering method	Porous materials are obtained through compaction, bonding, and sintering processes using metal powders as raw materials	Easy to operate, low cost	The prepared porous titanium alloy has a rough interior, irregular pores and small pore size	38
Foaming	Gas or solid particles are heated, subjected to sudden changes in pressure, or undergo chemical reactions to produce gas, which expands and overflows during the metal melting process to prepare porous structures	Rapid preparation and large aperture	It is often used to prepare polymer porous materials, and it is difficult to prepare porous metal materials	46
Space holder method	The metal powder is mixed with the pore-making agent in proportion, and the precursor is made into a precursor for sintering under certain conditions, and the porous metal material is obtained by removing the pore-making agent during the process of sintering	Controllable porosity, pore shape and distribution	There are partially closed holes; the pore-making agent may easily remain in the material	86
Gel injection molding	The porous structure is obtained by preparing gel metal mixed slurry with low viscosity and high solid volume fraction and putting it into the mold, drying, and sintering the slurry	Fulfilling the implant's appearance requirement, and low cost in mold-making	Poor toughness, low strength	54
Fiber weaving method	Metal fibers are wound or arranged into the desired structure, and then placed in a reducing atmosphere for sintering to fully bond the contact points between the fibers, resulting in porous titanium alloy	Scaffolds or mesh implants with large porosity can be prepared	It is easy to break at the intersection of wires	87
Additive manufacturing				
SLS/EBM/SLM	Laser or electron beam is used as a heat source to selectively irradiate pre-laid powder materials, achieving rapid material melting and forming	The complex porous metal can be prepared with high precision and controllable performance	High cost, slow speed, and not suitable for mass production	88
DIW	Metal powder materials are mixed with viscous fluids to form a precursor, using a nozzle with a certain diameter for extrusion molding, followed by drying/photocuring shaping, and finally, sintering into a porous structure	The internal stress is small, and functional components can be added	Single structure and low strength	83

Abbreviations: DIW: Direct ink writing; SLS: Selective laser sintering; EBM: Electron beam melting; SLM: Selective laser melting.

Table 2. Porosity and mechanical properties of porous titanium prepared by different processes

Processing technology	Materials	Porosity (%)	Ultimate strength (MPa)	Elastic modulus (GPa)	References
Sintering method					
Powder sintering method	Ti	34.6	560	20	38
Foaming method	Ti-Nb-Zr	6.06 – 62.8	73.4 – 1530.5	1.2 – 10.8	45
Space holder technique	Ti	35 – 65	22 – 126	0.063 – 1.18	49
Gel injection molding	Ti-Mo, Ti-Nb	39 – 50	-	5 – 18	53
Fiber braiding method	Ti	40 – 55	12.9 – 52.5	0.4 – 1.4	55
Additive manufacturing					
SLS	Ti-6Mo	24 – 58	31.4 – 152.8	2.07 – 41.9	60
EBM	TC4	70	-	1.4	70
SLM	NiTiNb	60	82 – 321	1.51 – 3.32	78
DIW	Ta-Ti-Nb-Zr	-	70.08 – 149.95	0.18 – 0.64	82

Abbreviations: DIW: Direct ink writing; EBM: Electron beam melting; SLM: Selective laser melting; SLS: Selective laser sintering.

matching degree of its mechanical properties with human tissues,[8] cannot change the fact that titanium alloy is a bioinert metal. Several problems such as inflammation and bone resorption in the human body still persist with using this kind of alloy. In addition, porous implants also face problems such as antimicrobial/inducible/osteogenic/wear/corrosion resistance.[89] Therefore, in addition improving mechanical properties (strength and modulus) through material development and structural design, augmenting the performance of porous implants through surface modification has become the focus of researchers.[90]

Porous implants have a complex internal structure, and it is difficult to penetrate the interior of the implants by means of the strong plastic surface processing techniques, such as friction stir,[91] shot peening[92], and femtosecond laser.[93] Therefore, the modification of porous implants mostly takes fluid (gas and liquid) as the medium, by modifying the surface morphology of porous titanium or adding components, as shown in Figure 9. In this section, based on the working principle of surface modification, the medical porous titanium alloy is divided into four categories: physical modification, chemical modification, biological modification, and composite modification (or compound method), and the advantages and disadvantages of different methods and influencing factors are summarized.

4.1. Physical modification

The physical method mainly refers to the modification of the surface structure and roughness of porous titanium. The surface roughness and surface free energy of materials are the necessary conditions that affect cellular processes such as protein adsorption, cell adhesion, migration, and differentiation. The use of chemical reagents and strong acids to etch titanium alloys is a common method to change the surface structure of materials.[94]

Reagent type, concentration, and etching time affect the material's surface properties. In addition, the composition and structure of porous titanium alloys also affect the material's surface roughness and mechanical properties. Civantos *et al.*[95] chemically etched porous titanium scaffolds for manufacturing additives by hydrofluoric acid impregnation and studied the effect of etching time (125 s, 625 s) on the biological properties. The results showed that 125 s of porous titanium etching time was more conducive to cell adhesion, while 625 s of etching promoted cell osteoblastic differentiation. However, etching will also hurt the mechanical properties of porous titanium. Wang *et al.*[96] investigated the effect of etching time on the mechanical properties of porous titanium in a hydrochloric acid solution containing 20% (mass fraction). Pitting and grain boundary corrosion occurred in a hydrochloric acid solution on porous titanium's inner and outer surfaces. With time, the number and size (diameter and depth) of etching pits increased significantly, and the material strength decreased from 152 MPa to 106 MPa after 150 min.

Etching plays an important role in the early surface modification of porous implants due to its simplicity and low cost of operation. However, it is difficult to control the surface morphology of the material, and the corrosion process can cause cracks or stress concentration, which affects the fatigue performance of the scaffold.

4.2. Chemical modification

The chemical method is used to introduce inorganic materials or organic components onto the surface of porous scaffold, contact them with cells/tissues, or release functional components, and then affect cell behavior to achieve bone formation or an antibacterial effect. According to the processing methods, it is mainly divided into chemical molecular dipping, vapor deposition, and electrochemical methods.

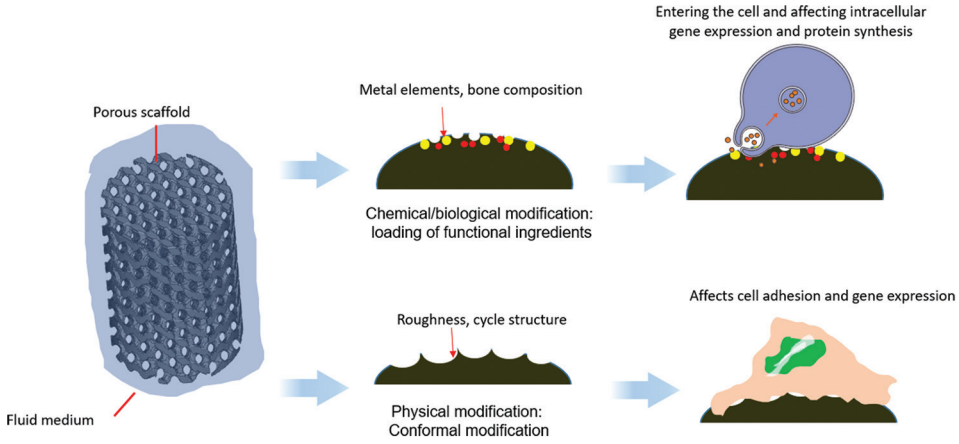

Figure 9. Schematic diagram of morphologic modification of porous implants or surface modification by adding components in a liquid environment.

4.2.1. Chemical molecular dipping

In the chemical molecular dipping method, the scaffold is immersed in a solution containing active ingredients, and the solution adheres to the surface of the material through chemical reaction or drying to form a coating so as to improve the material performance of porous implants whose performance is mainly affected by the chemical composition.[97] At present, components that are added to its surface are primarily Ca/P inorganic salt materials such as hydroxyapatite and organic materials.

Calcium phosphate and hydroxyapatite are the main inorganic components of human bone and the most common additive components, which can participate in metabolism, stimulate or induce regeneration of bone tissue, and accelerate the repair of damaged parts. Because of its brittleness, hydroxyapatite is generally coated by thermal spraying, laser cladding, and hydrothermal treatment. In addition, to promote the deposition of inorganic materials, its adsorption can also be promoted by alkali heat treatment in advance. Wang *et al.*[98] immersed TiNbZr alloy in sodium hydroxide solution and heated it at 60°C in an autoclave for 24 h. The treated scaffold was immersed in simulated body fluid (SBF) for a week so that Ca/P elements were uniformly deposited on the material's surface. Cell experiments showed that synthetic calcium and phosphorus materials significantly enhanced cell fixation and osseointegration, and enhanced phenotypic osteogenic lineages (osteopontin and osteonectin) and osteoblast synthesis activities of human bone marrow-derived mesenchymal cells.

The organic polymer coating is conducted mainly by preparing a solution containing the expected load components, and soaking the modified porous titanium alloy in the solution, a step through which the substrate binds to the surface through electrostatic adsorption or chemical reaction with the functional group of active molecules, to achieve a firm bond between the substrate and the load material. Chudinova *et al.*[99] coated chitosan/hydroxyapatite composite (CS/HA) on a porous titanium surface to prepare biomaterials with good bone integration ability. It was shown that CS/HA composites are novel materials for treating bone defects in diabetic patients by reactivating the Wnt/b-catenin pathway.

Chemical conjugation between the substrate surface and grafted molecules is vital to stable covalent modification. Compared with electrostatic interaction, chemical grafting with polydopamine (PDA) as a binder can achieve more multi-functional component loading.[100] Jiao *et al.*[101] utilized PDA combined with Ag particles to modify the porous titanium surface. PDA achieved tunability of silver adsorption and release, and the modified surface had better antimicrobial properties than the pristine surface, as shown in Figure 10.

Chemical molecular dipping has played an important role in the field of surface modification of early medical materials; its preparation conditions are simple, and the cost involved is low. However, given an array of pitfalls, such as the weak binding force between the prepared coating and the substrate, the poor surface wear resistance of the scaffold, and the susceptibility to fatigue fracture, it proves to be difficult to use in a complex stress environment.

4.2.2. Vapor deposition

The vapor deposition method refers to vaporizing the component to be added, contacting porous titanium, and forming a film on the surface, as shown in Figure 11A. According to the principle of gasification and reaction, it can be divided into physical vapor deposition (PVD) and chemical vapor deposition (CVD).

PVD is a method in which the target material is transferred by evaporation or sputtering in atomic, molecular, or ion states and aggregated on the surface of the substrate to form a film in a vacuum environment.[102] This method primarily encompasses vacuum evaporation, sputtering coating, and ion coating. Escudero *et al.*[103] used PVD to deposit silver coating with a thickness of 4.5 ± 1.5 μm on the surface of porous Ti6Al4V alloy. Compared with the blank group, the silver-coated scaffold reduced the adhesion of *Staphylococcus aureus* on the porous sample and inhibited the formation of *Staphylococcus* biofilm on the material's surface within 72 h. In addition, the maximum cumulative silver release measured within 28 days was $<3.5 \times 10^{-6}$ ppm, which did not cause significant damage to osteoblasts' adhesion, proliferation, and differentiation, highlighting good compatibility and antibacterial effects.

CVD refers to depositing a metal inorganic coating or solid film on the substrate by chemical reaction with one or several compounds containing film elements after gasification. Wang *et al.* used the CVD method to prepare tantalum coating on the surface of a porous TC4 scaffold, as shown in Figure 11B. The healing and fusion effect of the scaffold in rabbits with lumbar vertebrae resection was evaluated. The results showed that bone marrow-derived mesenchymal stem cells (BMSCs) increased on the surface of Ta-coated scaffolds by a larger margin than those in the blank group (Figure 11C).

Due to the rapid gas diffusion, the gas deposition method can be used to modify the surface of complex porous structures, producing a deposited coating with high purity. However, the problem with this process is that the thickness of the deposited coating is small. Compared with

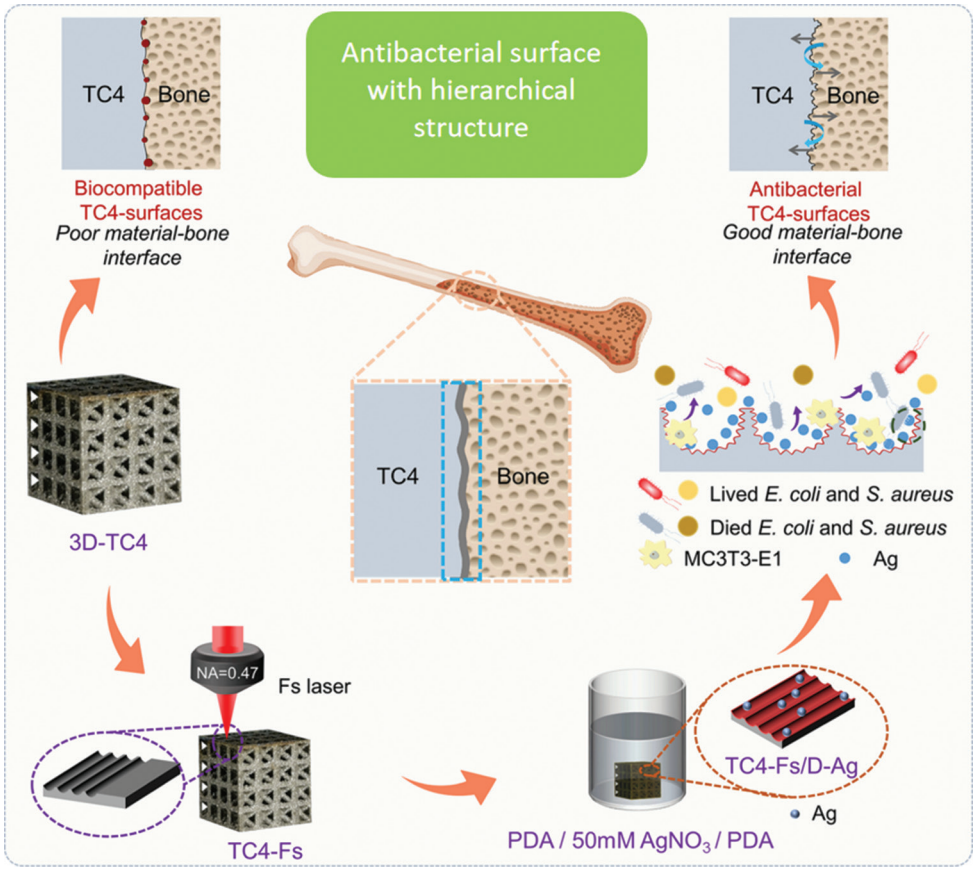

Figure 10. Construction of antibacterial coating by combining polydopamine (PDA) with Ag particles.[101]

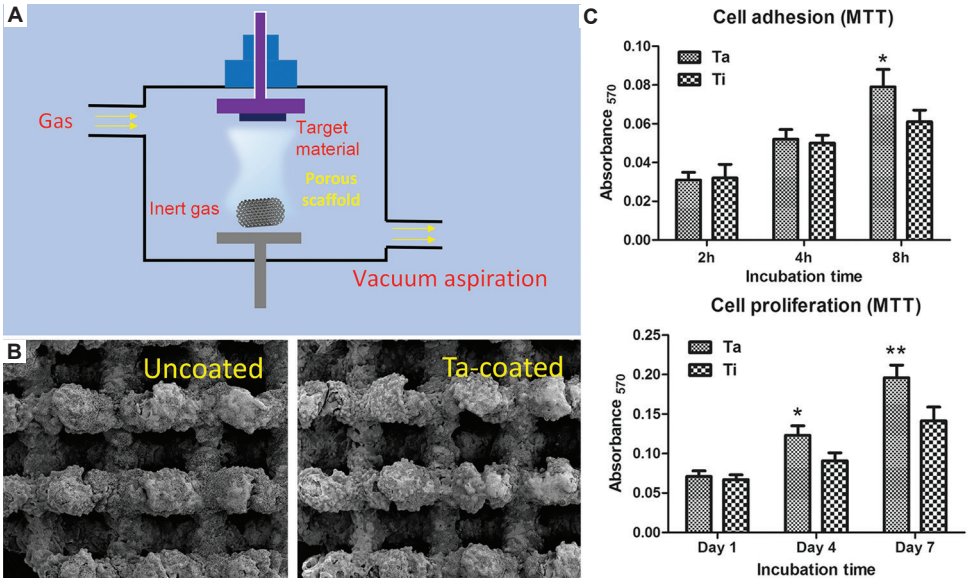

Figure 11. Principle of vapor phase deposition and coating morphology. (A) Schematic diagram of the principle of vapor deposition. (B) Physical vapor deposition on the surface of porous titanium before and after Ta coating. (C) Cell adhesion and proliferation on different scaffold surfaces.[104] Copyright © 2018 Springer. Reprinted with permission from Springer.

the PVD method, the films prepared by the CVD method have better matrix coverage and progressivity.

4.2.3. Electrochemical modification

Electrochemical modification is one of the most widely used methods for material surface modification. The underlying principle involves preparing a metal salt solution with pre-added substances, using the material to be plated as the electrode, and leveraging an electrochemical reaction to precipitate ions in the solution and fix them on the material's surface to generate a coating.[105] According to the reaction principle, it is mainly divided into electrochemical deposition, micro-arc oxidation, anodic oxidation, and other processes.

Electrochemical deposition, also known as electrodeposition, electrophoretic deposition, or electroplating, is a method of depositing materials (metals, polymers, ceramics, glass, and their composites) onto a base material through redox reactions using an electric current. Vidal *et al.*[106] performed pulse electrodeposition on porous titanium scaffolders to achieve uniform coverage of Ca-P coating. The results of antibacterial tests showed that the scaffolds possess antibacterial activity against Gram-positive and Gram-negative bacterial strains and effectively reduced the infection around the implant. In addition, researchers also electroplated Cu, Zn, Ag, and other metals onto the material's surface to improve biocompatibility. Guo *et al.*[107] prepared titanium copper/titanium copper nitride coating by electroplating on the surface of the titanium scaffold. Biological experiments showed that the proliferation and adhesion of human bone mesenchymal stem cells on coated scaffolds were higher than those on blank scaffolds. The coating plays a significant role in adsorbing hBMSCs, upregulating *SDF-1a/CXCR4* gene expression, and stimulating extracellular signal-related kinase (Erk) and Akt signaling pathways. Compared with conventional chemical deposition, the coating materials prepared by electrochemical deposition have better uniformity, wider thickness range, and higher bonding strength.

The anodizing method can form a uniform porous structure on the surface of materials, which is a convenient and fast method for preparing highly ordered nanotube structures,[108] as shown in Figure 12A. The geometric characteristics of nanotube arrays (morphology, length, pore size, and wall thickness) are influenced by various factors such as anodizing time, voltage, electrolyte composition, viscosity coefficient of electrolyte, and substrate composition.[109] Its electrolytes are mainly composed of nitric acid, hydrofluoric acid, and organic compounds such as fluoride salts and ethylene glycol.[110]

Liang *et al.*[111] utilized titanium alloy porous screws as anodes, using an electrolyte solution containing ethylene glycol (EG), water and ammonium fluoride, and conducted anodic oxidation reactions using a direct current voltage source. The voltages were set to 10, 15, 20, and 25 V and continuously energized for 40 min. Observation of the surface of porous screws reveals that the morphology of the anodized surface is influenced by the location of the screw and the magnitude of the voltage. Shokuhfar *et al.*[109] used HH_4F and ethylene glycol as electrolytes, 60 V constant voltage, and direct current to conduct anodic oxidation experiments on CP-Ti surface and TC4 surface, respectively, to obtain periodic nanotube structures. The total cell density was higher on the cp-Ti surface than on the TC4 alloy surface because the precipitation of Al and V elements in the TC4 alloy affected cell proliferation.

During micro-arc oxidation, the material is used as the anode in the electrolyte, and a strong voltage is employed to generate micro-arc discharge and local high temperature so that the electrolyte ions vaporize at high temperature to form plasma and oxidize with the porous implant, thus generating a metal oxide coating with TiO_2 as the main component,[112] as shown in Figure 12B. The coating prepared by this process is mainly affected by factors such as pulse frequency, duty cycle, duration, and electrolyte composition.[113]

Carbonate, sulfate, and silicate solutions containing Ca/P/Si elements are the most commonly used electrolytes.[114] Yan *et al.*[115] formed a bioactive coating enriched with micropores on the pore wall of porous titanium by micro-arc oxidation. The composition analysis of the coating shows that the porous titanium coating is mainly composed of anatase and rutile TiO_2 and other complex Ca-P-Sr phases. *In vitro*, osteogenic induction experiments showed that the porous titanium treated with MAO displayed good apatite induction ability. In addition to the traditional electrolyte, some new materials, such as graphene, are also added to the solution. Sun *et al.*[116] coated graphene on a porous titanium alloy using a micro-arc oxidation process. Biological experiments showed that graphene coating significantly improved the surface roughness of the material, and promoted the adhesion, growth, and proliferation of human adipose-derived stem cells. In addition, graphene-coated scaffolds also successfully repaired rabbit mandibular defects, providing a new idea for the clinical application of tissue engineering in the field of oral and maxillofacial bone defect repair. The coating prepared by micro-arc oxidation has the advantages of good wear resistance, strong corrosion resistance, and small thermal conductivity. Applying different electrolyte components can ensure the other functions achievable by micro-arc oxidation coating, a property that can be leveraged to add relevant substances to the electrolyte to make the coating more biocompatible.

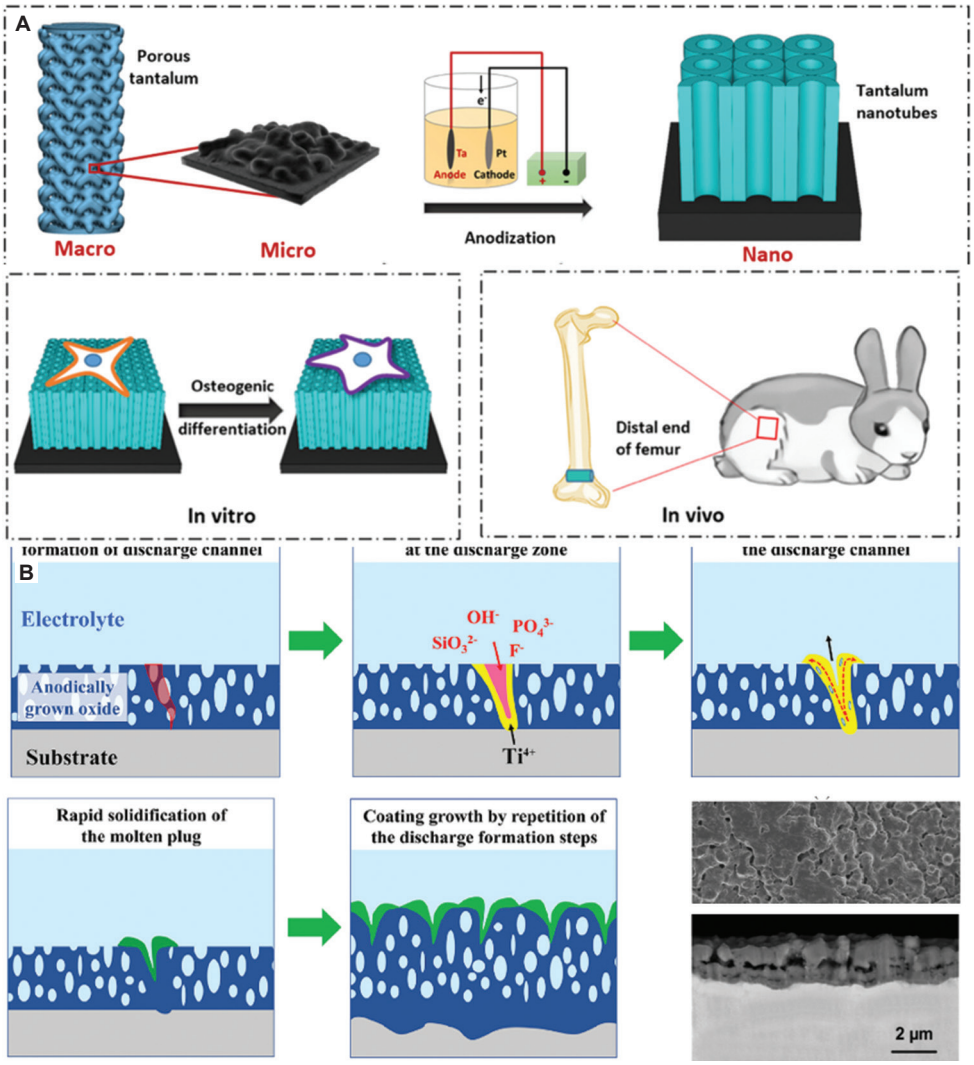

Figure 12. Coatings prepared using different electrochemical methods. (A) Schematic diagram of anodizing processing and its working principle.[108] Copyright © 2021 Elsevier. Reprinted with permission from Elsevier. (B) Micro-arc oxidation surface preparation principle and surface image.[112] Copyright © 2023 Elsevier. Reprinted with permission from Elsevier.

4.3. Loaded drug or active substance

The antibacterial and osteogenic effects of porous implants can be achieved by modifying the materials' surface morphology and chemical composition. However, it is often difficult to control the release time and content from the porous implants generated by methods such as metal element coating, a predicament that would cause certain damage to the human body. Thus, loading drugs, stem cells, or exoactive substances on the surface of porous scaffolds can greatly improve its safety.

Due to the strict storage conditions required for drugs and bioactive substances, a much stringent set of requirements should be applied in the design of carriers. Hydrogels emerge as the ideal carriers of drugs and bioactive substances due to their high hydrophilicity, unique three-dimensional network, good biocompatibility, and cell adhesion.[117,118] Bai *et al.*[119] constructed a porous titanium/Poloxam 407 hydrogel system loaded with zoledronate (ZOL) to promote bone integration in rabbit osteoporosis models to inhibit local excessive bone absorption and promote bone integration. The composite scaffold (ZOL/gTi) showed good biocompatibility and continued to release ZOL as the hydrogel degraded (Figure 13A).

Cell tissue modification refers to the culture of stem cells or their secretions *in vitro* and subsequently the modification of the surface of materials by gel loading or by culture with materials. Yu *et al.*[120] encapsulated bone BMSCs into a matrix gel, as shown in Figure 13B. Subsequently, the BMSC-containing matrix was infiltrated into the porous Ti6Al4V scaffold surface to improve the extracellular

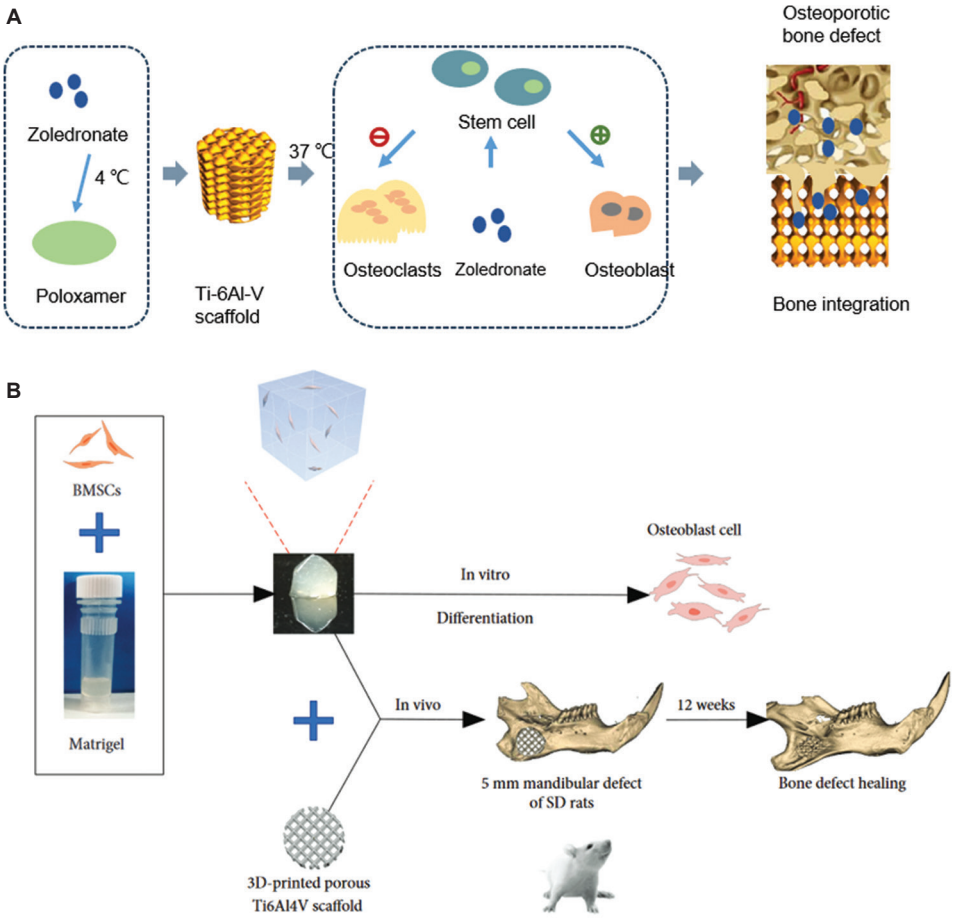

Figure 13. Porous titanium alloy bioactive coating for medical applications. (A) Preparation and effect of a gel-supported drug promoting bone formation. (B) Hydrogel-supported BMSCs promoting bone repair coating[120] Copyright © 2019 Hindawi. Reprinted with permission from Hindawi.

environment of porous titanium alloys. Compared with the local injection of BMSCs, the modified Ti6Al4V scaffold promoted the formation of new bone at the mandibular defect site in rats. Qiao *et al.*[121] constructed pure titanium scaffolds coated with platelet-rich plasma (PRP) by freeze-drying. *In vitro* biological experiments showed that PRP-coated porous titanium scaffolds significantly promoted the attachment, proliferation, migration, and osteogenic differentiation of bone marrow mesenchymal stem cells (BMSCs). *In vivo* studies of implant coatings using an osteoporosis model have shown that the bioactive interface of PRP coatings enhanced bone vitality.

Compared with changing the surface morphology of materials and adding metal elements, loaded drugs or active substances have no side effects on damaged tissues, and their effectiveness and safety are significantly improved.[122] However, this modification method necessitates excellent extraction and storage of surface materials. Hence, developing low-cost modification methods for active substances is one of the critical problems to be solved.

4.4. Compound method

Oftentimes, approaches such as surface modification of porous implants, chemical composition adjustment, and active material loading would only produce implants with limited conducive functions or properties. In the context of addressing the urgent needs to promote osteogenic and antibacterial effects, especially during the early stages of implantation, there is increasing interest in unifying morphology modification and composition loading approaches to create multifunctional implants. Therefore, combining morphology modification and composition loading to obtain multiple effects has become one of the hot research topics.

Ag particles have antibacterial effects. Depending on this property, Croes *et al.*[123] added different concentrations of Ag nanoparticles to the chitosan-based (Ch) coating. The Ch+Ag particle composite coating is endowed with enhanced antibacterial properties than simple chitosan coating. Wei *et al.*[124] prepared carbon nanotubes by electrophoretic deposition on the surface of porous titanium

and then added mesoporous silica nanoparticles (MSNs) and mechanical growth factor (MGF) into the carbon nanotubes, as shown in Figure 14. The results of biological experiments show that the porous titanium coating has a nanostructured topological structure and can improve myoblasts' adhesion, proliferation, and myogenic differentiation on the material's surface through covalent bond prolongation.

The dynamic changes in the fluid environment and tissues present hurdles for the continual usage of implants. For example, the surface morphology of porous titanium cannot adapt with time to the continuous changes, posing difficulty to the chemical composition released in response to a change in tissue growth and the human environment. Using ultrasonic, electromagnetic, photothermal, and other external stimulation combined with special coatings, the function of the modified layer can be stimulated to achieve dynamic regulation and satisfy the conditions required for human tissue recovery.[125] As shown in Figure 15, Wu

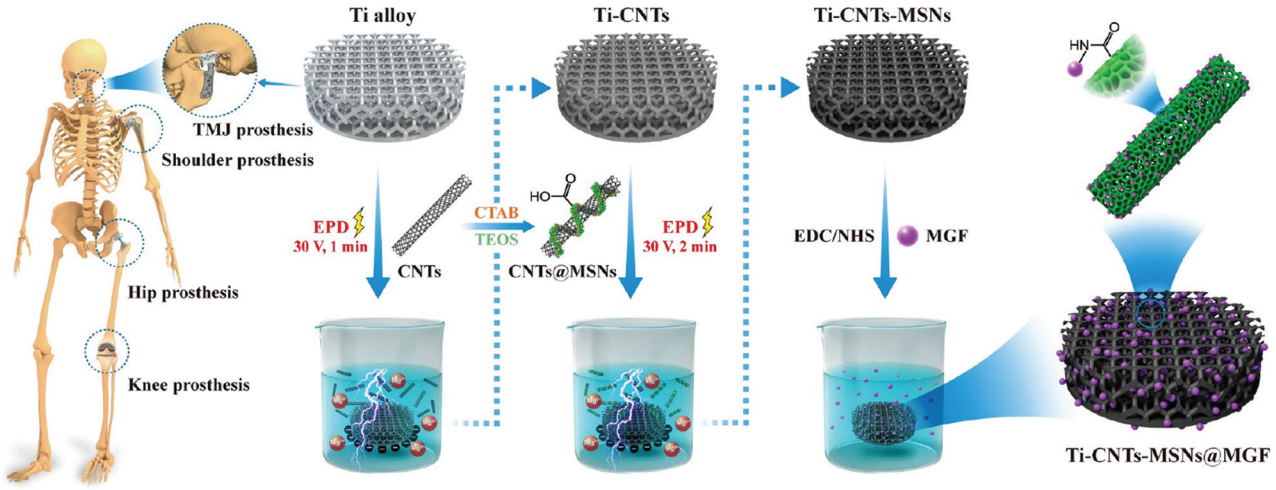

Figure 14. Multi-method composite construction coating. The porous prosthesis was coated with CNT and deposited to Ti-CNTS-MSNS@MGF.[124] Copyright © 2022 ACS. Reprinted with permission from ACS.
Abbreviations: CNTs: Carbon nanotubes; CTAB: Cetyltrimethylammonium bromide; EDC/NHS: N-hydroxysuccinimide and 1-ethyl-3-(3-dimethylaminopropyl) carbodiimide hydrochloride; EPD: Electrophoretic deposition; MGF: Mechanical growth factor; MSNs: Mesoporous silica nanoparticles; TEOS: Tetraethoxysilane; TMJ: Tendon muscle junction.

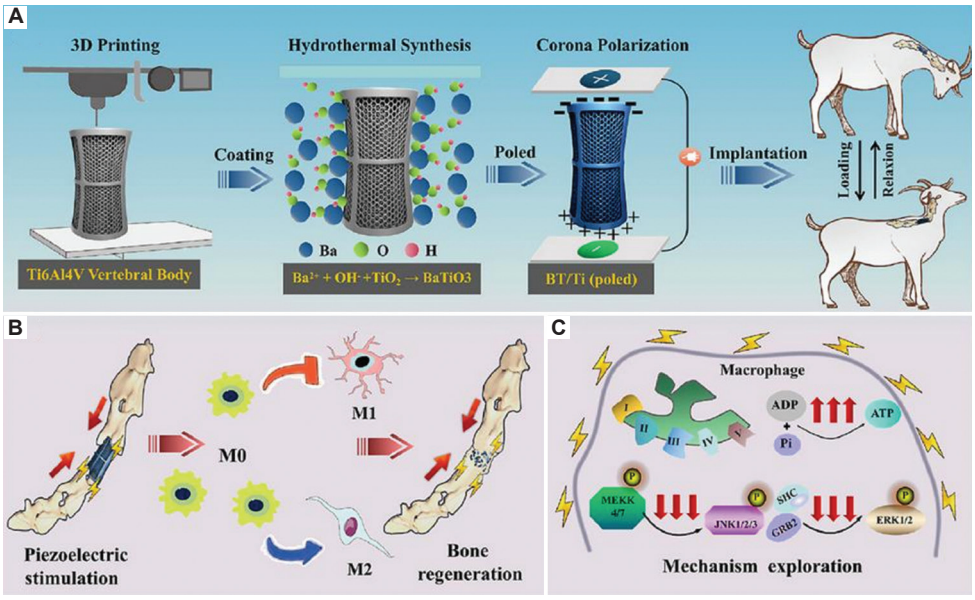

Figure 15. Porous Ti6Al4V scaffold coated with barium piezoelectric titanate and implantation scaffold and mechanism of bone formation.[126] Copyright © 2023 Elsevier. Reprinted with permission from Elsevier.

et al.[126] used a hydrothermal synthesis method to form $BaTiO_3$ coating uniformly on the surface of a 3D-printed porous Ti6Al4V scaffold. The ultrasonic excitation of coating vibration to generate electrical stimulation promoted the pro-regenerative M2 polarization, inhibited the M1 polarization of macrophages, and promoted the bone regeneration process of the sheep cervical vertebra resection model.

The principles, advantages, and disadvantages of different surface modification methods are summarized in Table 3.

5. Summary and outlook

Medical porous titanium alloy has broad development prospects in biological tissue engineering. Through the review and summary of its performance requirements, processing methods, modification methods, and effects, the following conclusions are drawn:

(i) Medical porous titanium alloy in the human body mainly plays a fixed, supporting, loading, and other roles. Good mechanical properties (strength, modulus, corrosion/wear resistance) guarantee biocompatibility and ensure the primary conditions for their functioning, while the above properties can be influenced by the material composition, structural design, and surface properties.

(ii) The porous structure can reduce elastic modulus and improve compatibility, in terms of mechanical properties, with the human body. The properties of porous titanium are affected by the preparation process and structure. According to the sintering principle, the preparation process of porous titanium mainly includes the sintering method, fiber preparation, additive manufacturing, and so on. With the development of additive manufacturing, the machining accuracy and structural complexity of porous titanium will be continuously improved, alongside the steady develop of a design scheme based on design elements such as aperture, porosity, and structural units. In the future, additive manufacturing of porous titanium alloys will take into consideration the development of new materials and the structural topology optimization for realizing the processing of structure-function integrated devices, with the aim of enhancing their performance in mimicking human tissue.

Table 3. Comparison of different surface modification processes for porous titanium alloys

Modified technology	Preparation principle	Working principle	Advantages	Disadvantages	References
Physical modification	Alteration of the surface structure and roughness of the material by means of etching, *etc*.	Forms a certain rough structure on the surface of the material to promote cell growth	Low cost and easy to operate	Poorly effective	95
Chemical modification					
Chemical molecular dipping	The coating is directly formed by a chemical reaction between the modified solution and the surface of the material	Influence cellular behavior by attaching chemicals to surfaces	Low cost and effective	Low bonding strength to the material surface, prone to debris and inflammation	101
Vapor deposition	Attachment of the metal to the surface of the material by vaporization of the evaporated metal to produce a modified film by reaction	Acts on cells/bacteria via metallic components such as Ag/Cu/Zn in the film	Good coating bonding properties, suitable for metal element modification	Limited metal loading and thin modification layer	127
Electrochemical modification	Electrochemical reaction causes the analytes in the electrolyte to adhere to the surface of the material to form a coating	The electrolyte component and porous structure of the coating also promote cell growth	Strong binding and good effect	High cost and complex preparation process	109 107 115
Loaded drug or active substance	Bioactive substances such as drugs and cellular platelets are loaded onto the surface of the material using a carrier such as a gel	Promote tissue recovery by releasing drugs and building a bioactive environment	High safety and quick recovery	High requirements for surface coating preparation	117 119
Compound method	Combining morphological modification with compositional effects, or building coatings from combinations of different components	The synergistic action of different components, or the joint action of surface morphology and components	Better results with simultaneous antimicrobial and osteogenic effects	High preparation requirements and complex processes	126

(iii) The surface modification process is a crucial step for endowing the material with functional properties. Given the complex internal structure of porous titanium alloy, penetrating the inside of the structure using the traditional modification method is challenging; therefore, surface modification of porous titanium is mostly conducted in a fluid medium. According to the principle of action, the modification strategies of porous titanium alloy can be divided into physical modification, chemical composition loading, biological activity introduction, *etc.* Composite modification combines the above methods to achieve multiple functions simultaneously. In addition, the spatiotemporal modulation of coating properties through external aids, such as sound, light, electricity, heat, and magnetism, can help with further adapting to the growth of human tissues and environmental changes and allow for matching with human properties, paving the way to become the new generation of modification methods.

Acknowledgments

This project acknowledges the support of Guangxi Key Laboratory for Preclinical and Translational Research on Bone and Joint Degenerative Diseases (21-220-06).

Funding

None.

Conflict of interest

The authors declare that they have no competing interests.

Author contributions

Conceptualization: Liqiang Wang
Data curation: Miao Luo and Yuting Lv
Supervision: Chengliang Yang
Writing – original draft: Binghao Wang and Zheng Shi
Writing – review and editing: Binghao Wang and Yuwen Cui

Ethics approval and consent to participate

Not applicable.

Consent for publication

Not applicable.

Availability of data

Not applicable.

References

1. Evans JT, Evans JP, Walker RW, Blom AW, Whitehouse MR, Sayers A. How long does a hip replacement last? A systematic review and meta-analysis of case series and national registry reports with more than 15 years of follow-up. *Lancet*. 2019;393:647-654.

   doi: 10.1016/S0140-6736(18)31665-9.

2. Gupta K, Meena K. Artificial bone scaffolds and bone joints by additive manufacturing: A review. *Bioprinting*. 2023;31:e00268.

   doi: 10.1016/j.bprint.2023.e00268

3. Denry I, Kelly JR. Emerging ceramic-based materials for dentistry. *J Dent Res*. 2014;93:1235-1242.

   doi: 10.1177/0022034514553627.

4. Dong T, Duan C, Wang S, *et al*. Multifunctional surface with enhanced angiogenesis for improving long-term osteogenic fixation of poly(ether ether ketone) implants. *ACS Appl Mater Interfaces*. 2020;12:14971-14982.

   doi: 10.1021/acsami.0c02304

5. Wang N, Ma Y, Shi H, Song Y, Guo S, Yang S. Mg-, Zn-, and Fe-based alloys with antibacterial properties as orthopedic implant materials. *Front Bioeng Biotechnol*. 2022;10:888084.

   doi: 10.3389/fbioe.2022.888084

6. Liang W, Zhou C, Zhang H, *et al*. Recent advances in 3D printing of biodegradable metals for orthopaedic applications. *J Biol Eng*. 2023;17:56.

   doi: 10.1186/s13036-023-00371-7

7. Song C, Liu L, Deng Z, *et al*. Research progress on the design and performance of porous titanium alloy bone implants. *J Mater Res Technol*. 2023;23:2626-2641.

   doi: 10.1016/j.jmrt.2023.01.155

8. Guo AXY, Cheng L, Zhan S, *et al*. Biomedical applications of the powder-based 3D printed titanium alloys: A review. *J Mater Sci Technol*. 2022;125:252-264.

   doi: 10.1016/j.jmst.2021.11.084

9. Gao C, Li C, Wang C, *et al*. Advances in the induction of osteogenesis by zinc surface modification based on titanium alloy substrates for medical implants. *J Alloy Compd*. 2017;726:1072-1084.

   doi: 10.1016/j.jallcom.2017.08.078

10. Sun Y, Hu W, Wu C, *et al*. Research progress on mechanical properties of 3D printed biomedical titanium alloys. *J Mater Eng Perform*. 2023;32:9489-9503.

    doi: 10.1007/s11665-023-08248-y

11. Liu R, Su Y, Yang W, *et al*. Novel design and optimization of porous titanium structure for mandibular reconstruction. *Appl Bionics Biomech*. 2022;2022:8686670.

    doi: 10.1155/2022/8686670

12. Long S, Zhu J, Jing Y, He S, Cheng L, Shi Z. A comprehensive review of surface modification techniques for enhancing the biocompatibility of 3D-printed titanium implants. *Coatings*.

2023;13:1917.

doi: 10.3390/coatings13111917

13. Asri RIM, Harun WSM, Samykano M, *et al*. Corrosion and surface modification on biocompatible metals: A review. *Mater Sci Eng C Mater Biol Appl*. 2017;77:1261-1274.

doi: 10.1016/j.msec.2017.04.102

14. Ottria L, Lauritano D, Bassi MA, *et al*. Mechanical, chemical and biological aspects of titanium and titanium alloys in implant dentistry. *J Biol Regul Homeost Agents*. 2018;32:81-90.

15. Sheng X, Wang A, Wang Z, Liu H, Wang J, Li C. Advanced surface modification for 3D-printed titanium alloy implant interface functionalization. *Front Bioeng Biotechnol*. 2022;10:850110.

doi: 10.3389/fbioe.2022.850110

16. Raman RKS, Wen C, Loeffler JF. Human Body-fluid-assisted fracture of zinc alloys as biodegradable temporary implants: Challenges, research needs and way forward. *Materials*. 2023;16:4984.

doi: 10.3390/ma16144984

17. Dziaduszewska M, Zieliński A. Structural and material determinants influencing the behavior of porous Ti and its alloys made by additive manufacturing techniques for biomedical applications. *Materials*. 2021;14:712.

doi: 10.3390/ma14040712

18. Khodaei M, Fathi M, Meratian M, Savabi O. The effect of porosity on the mechanical properties of porous titanium scaffolds: Comparative study on experimental and analytical values. *Mater Res Express*. 2018;5:055401.

doi: 10.1088/2053-1591/aabfa2

19. Xiong YZ, Gao RN, Zhang H, Dong LL, Li JT, Li X. Rationally designed functionally graded porous Ti6Al4V scaffolds with high strength and toughness built via selective laser melting for load-bearing orthopedic applications. *J Mech Behav Biomed Mater*. 2020;104:103673.

doi: 10.1016/j.jmbbm.2020.103673

20. Lv Y, Wang B, Liu G, *et al*. Metal material, properties and design methods of porous biomedical scaffolds for additive manufacturing: A review. *Front Bioeng Biotechnol*. 2021;9:641130.

doi: 10.3389/fbioe.2021.641130

21. Wei G, Tan M, Attarilar S, *et al*. An overview of surface modification, a way toward fabrication of nascent biomedical Ti–6Al–4V alloys. *J Mater Res Technol*. 2023;24:5896-5921.

doi: 10.1016/j.jmrt.2023.04.046

22. Oesterle W, Klaffke D, Griepentrog M, Gross U, Kranz I, Knabe C. Potential of wear resistant coatings on Ti-6Al-4V for artificial hip joint bearing surfaces. *Wear*. 2008;264:505-517.

doi: 10.1016/j.wear.2007.04.001

23. Bobbert FSL, Lietaert K, Eftekhari AA, *et al*. Additively manufactured metallic porous biomaterials based on minimal surfaces: A unique combination of topological, mechanical, and mass transport properties. *Acta Biomater*. 2017;53:572-584.

doi: 10.1016/j.actbio.2017.02.024

24. Lv Y, Liu G, Wang B, *et al*. Pore strategy design of a novel NiTi-Nb biomedical porous scaffold based on a triply periodic minimal surface. *Front Bioeng Biotechnol*. 2022;10:910475.

doi: 10.3389/fbioe.2022.910475

25. Zhang T, Wang W, Liu J, Wang L, Tang Y, Wang K. A review on magnesium alloys for biomedical applications. *Front Bioeng Biotechnol*. 2022;10:953344.

doi: 10.3389/fbioe.2022.953344

26. Sidhu SS, Singh H, Gepreel MAH. A review on alloy design, biological response, and strengthening of β-titanium alloys as biomaterials. *Mater Sci Eng C Mater Biol Appl*. 2021;121:111661.

doi: 10.1016/j.msec.2020.111661

27. Zhang T, Fan Q, Ma X, *et al*. Effect of laser remelting on microstructural evolution and mechanical properties of Ti-35Nb-2Ta-3Zr alloy. *Mater Lett*. 2019;253:310-313.

doi: 10.1016/j.matlet.2019.06.105

28. Wang L, Lin Z, Wang X, *et al*. Effect of aging treatment on microstructure and mechanical properties of Ti27Nb2Ta3Zr β titanium alloy for implant applications. *Mater Trans*. 2014;55:141-146.

doi: 10.2320/matertrans.M2013187

29. Yuan L, Ding S, Wen C. Additive manufacturing technology for porous metal implant applications and triple minimal surface structures: A review. *Bioactive Mater*. 2019;4:56-70.

doi: 10.1016/j.bioactmat.2018.12.003

30. Zhao F, Wang J, Guo H, Liu S, He W. The effects of surface properties of nanostructured bone repair materials on their performances. *J Nanomater*. 2015;2015:893545.

doi: 10.1155/2015/893545

31. Cao S, Ma N, Zhang Y, Bo R, Lu Y. Fabrication, mechanical properties, and multifunctionalities of particle reinforced foams: A review. *Thin Walled Struct*. 2023;186:110678.

doi: 10.1016/j.tws.2023.110678

32. Rodriguez-Contreras A, Punset M, Calero JA, Javier Gil F, Ruperez E, Maria Manero J. Powder metallurgy with space holder for porous titanium implants: A review. *J Mater Sci Technol*. 2021;76:129-149.

doi: 10.1016/j.jmst.2020.11.005

33. Ryan G, Pandit A, Apatsidis DP. Fabrication methods of porous metals for use in orthopaedic applications. *Biomaterials*. 2006;27:2651-2670.

doi: 10.1016/j.biomaterials.2005.12.002

34. Majumdar T, Eisenstein N, Frith JE, Cox SC, Birbilis N. Additive manufacturing of titanium alloys for orthopedic applications: A materials science viewpoint. *Adv Eng Mater*. 2018;20:1800172.

doi: 10.1002/adem.201800172

35. Babaie E, Bhaduri SB. Fabrication aspects of porous biomaterials in orthopedic applications: A review. *ACS Biomater Sci Eng*. 2018;4:1-39.

doi: 10.1021/acsbiomaterials.7b00615

36. Luo SD, Qian M. Microwave processing of titanium and titanium alloys for structural, biomedical and shape memory applications: Current status and challenges. *Mater Manuf Process*. 2018;33:35-49.

doi: 10.1080/10426914.2016.1257800

37. Oh IH, Nomura N, Masahashi N, Hanada S. Mechanical properties of porous titanium compacts prepared by powder sintering. *Scripta Mater*. 2003;49:1197-1202.

doi: 10.1016/j.scriptamat.2003.08.018

38. Torres Y, Lascano S, Bris J, Pavón J, Rodriguez JA. Development of porous titanium for biomedical applications: A comparison between loose sintering and space-holder techniques. *Mater Sci Eng C Mater Biol Appl*. 2014;37:148-155.

doi: 10.1016/j.msec.2013.11.036

39. Annur D, Kartika I, Sudiro T, Supriadi S, Suharno B. Microstructure, mechanical properties, and *in vitro* studies of porous titanium obtained by spark plasma sintering. *Trans Indian Inst Metals*. 2022;75:3067-3076.

doi: 10.1007/s12666-022-02680-9

40. Saadati A, Aghajani H. Fabrication of porous NiTi biomedical alloy by SHS method. *J Mater Sci Mater Med*. 2019;30:92.

doi: 10.1007/s10856-019-6296-9

41. Han Q, Wang C, Chen H, Zhao X, Wang J. Porous tantalum and titanium in orthopedics: A review. *ACS Biomater Sci Eng*. 2019;5:5798-5824.

doi: 10.1021/acsbiomaterials.9b00493

42. Lascano S, Arevalo C, Montealegre-Melendez I, *et al*. Porous titanium for biomedical applications: Evaluation of the conventional powder metallurgy frontier and space-holder technique. *Appl Sci*. 2019;9:982.

doi: 10.3390/app9050982

43. Nugroho AW, Leadbeater G, Davies IJ. Fabrication and characterization of the porous titanium alloy by argon filled pore expansion technique. *IOP Conf Ser Mater Sci Eng*. 2018;403:012096.

doi: 10.1088/1757-899X/403/1/012096

44. Chen YJ, Feng B, Zhu YP, Weng J, Wang JX, Lu X. Fabrication of porous titanium implants with biomechanical compatibility. *Mater Lett*. 2009;63:2659-2661.

doi: 10.1016/j.matlet.2009.09.029

45. Rao X, Chu CL, Zheng YY. Phase composition, microstructure, and mechanical properties of porous Ti–Nb–Zr alloys prepared by a two-step foaming powder metallurgy method. *J Mech Behav Biomed Mater*. 2014;34:27-36.

doi: 10.1016/j.jmbbm.2014.02.001

46. Ahn MK, Jo IH, Koh YH, Kim HE. Production of highly porous titanium (Ti) scaffolds by vacuum-assisted foaming of titanium hydride (TiH2) suspension. Mater Lett. 2014;120:228-31.

doi: 10.1016/j.matlet.2014.01.065

47. Gonzalez, Z, Molero, E, Sanchez, J, Ferrari, B. Processing of titanium porous bodies by foaming of gelled aqueous suspensions of powders. *Preprints* 2021, 2021020099.

doi: 10.20944/preprints202102.0099.v1

48. Haghjoo R, Sadrnezhaad SK, Hassanzadeh-Nemati N. Synthesis, characterization, and biological studies of sintered porous titanium with three different pore morphologies. *Int J Mater Res*. 2023;114:43-53.

doi: 10.1515/ijmr-2022-0053

49. Luo H, Zhao J, Du H, Yin W, Qu Y. Effect of Mg powder's particle size on structure and mechanical properties of Ti foam synthesized by space holder technique. *Materials*. 2022;15:8863.

doi: 10.3390/ma15248863

50. Yang G, Xu B, Lei X, *et al*. Preparation of porous titanium by direct in-situ reduction of titanium sesquioxide. *Vacuum*. 2018;157:453-457.

doi: 10.1016/j.vacuum.2018.09.021

51. Chen Z, Wu C, Liu X, Shen T, Zhang L. Fabricating honeycomb titanium by freeze casting and anodizing for biomedical applications. *Adv Eng Mater*. 2022;24:2101088.

doi: 10.1002/adem.202101088

52. Li J, Li Z, Wang Q, *et al*. Sintered porous Ti6Al4V scaffolds incorporated with recombinant human bone morphogenetic protein-2 microspheres and thermosensitive hydrogels can enhance bone regeneration. *RSC Adv*. 2019;9:1541-1550.

doi: 10.1039/C8RA10200G

53. Yang D, Guo Z, Shao H, Liu X, Ji Y. Mechanical properties of porous Ti-Mo and Ti-Nb alloys for biomedical application by gelcasting. *Procedia Eng*.2012;36:160-167.

doi: 10.1016/j.proeng.2012.03.025

54. Biasetto L, De Moraes EG, Colombo P, Bonollo F. Ovalbumin as foaming agent for Ti6Al4V foams produced by gelcasting. *J Alloys Compd*. 2016;687:839-844.

doi: 10.1016/j.jallcom.2016.06.218

55. Liu P, Tan Q, Wu L, He G. Compressive and pseudo-elastic hysteresis behavior of entangled titanium wire materials. *Mater Sci Eng A*. 2010;527:3301-3309.

doi: 10.1016/j.msea.2010.02.071

56. Wang L, Xie L, Zhang LC, *et al*. Microstructure evolution and superelasticity of layer-like NiTiNb porous metal prepared by eutectic reaction. *Acta Mater.* 2018;143:214-226.

doi: 10.1016/j.actamat.2017.10.021

57. Li F, Li J, Xu G, Liu G, Kou H, Zhou L. Fabrication, pore structure and compressive behavior of anisotropic porous titanium for human trabecular bone implant applications. *J Mech Behav Biomed Mater*. 2015;46:104-114.

doi: 10.1016/j.jmbbm.2015.02.023

58. Ngo TD, Kashani A, Imbalzano G, Nguyen KTQ, Hui D. Additive manufacturing (3D printing): A review of materials, methods, applications and challenges. *Compos B Eng*. 2018;143:172-196.

doi: 10.1016/j.compositesb.2018.02.012

59. Agarwal R, García AJ. Biomaterial strategies for engineering implants for enhanced osseointegration and bone repair. *Adv Drug Deliv Rev*. 2015;94:53-62.

doi: 10.1016/j.addr.2015.03.013

60. *Structural Characteristics and Mechanical Behavior of Selective Laser Sintered Porous Ti-6Mo Alloy for Biomedical Applications-All Databases*, (n.d.). Available from: http://webvpn.swu.tsgvip.top/https/5377757368696765686l6f78756565212abc50b4738e8888c9482a5750aefc5fc6e25954c38c5bb888/wos/alldb/full-record/WOS:000379195400020 [Last accessed on 2024 Mar 03].

61. Davoodi E, Montazerian H, Mirhakimi AS, *et al*. Additively manufactured metallic biomaterials. *Bioactive Mater*. 2022;15:214-249.

doi: 10.1016/j.bioactmat.2021.12.027

62. Wang C, Huang W, Zhou Y, *et al.* 3D printing of bone tissue engineering scaffolds. *Bioactive Mater*. 2020;5:82-91.

doi: 10.1016/j.bioactmat.2020.01.004

63. Huang S, Kumar P, Yeong WY, Narayan RL, Ramamurty U. Fracture behavior of laser powder bed fusion fabricated Ti41Nb via in-situ alloying. *Acta Mater*. 2022;225:117593.

doi: 10.1016/j.actamat.2021.117593

64. Huang S, Narayan RL, Tan JHK, Sing SL, Yeong WL. Resolving the porosity-unmelted inclusion dilemma during in-situ alloying of Ti34Nb via laser powder bed fusion. *Acta Mater*. 2021;204:116522.

doi: 10.1016/j.actamat.2020.116522

65. Zadpoor AA. Additively manufactured porous metallic biomaterials. *J Mater Chem B*. 2019;7:4088-4117.

doi: 10.1039/C9TB00420C

66. Bikas H, Stavropoulos P, Chryssolouris G. Additive manufacturing methods and modelling approaches: A critical review. *Int J Adv Manuf Technol*. 2016;83:389-405.

doi: 10.1007/s00170-015-7576-2

67. Slámečka K, Kashimbetova A, Pokluda J, *et al*. Fatigue behaviour of titanium scaffolds with hierarchical porosity produced by material extrusion additive manufacturing. *Mater Des*. 2023;225:111453.

68. Sing SL, An J, Yeong WY, Wiria FE. Laser and electron-beam powder-bed additive manufacturing of metallic implants: A review on processes, materials and designs. *J Orthop Res*. 2016;34:369-385.

doi: 10.1002/jor.23075

69. Qu H. Additive manufacturing for bone tissue engineering scaffolds. *Mater Today Commun*. 2020;24:101024.

doi: 10.1016/j.mtcomm.2020.101024

70. Hara D, Nakashima Y, Sato T, *et al*. Bone bonding strength of diamond-structured porous titanium-alloy implants manufactured using the electron beam-melting technique. *Mater Sci Eng C Mater Biol Appl*. 2016;59:1047-1052.

doi: 10.1016/j.msec.2015.11.025

71. Sing SL, Yeong WY, Wiria FE. Selective laser melting of titanium alloy with 50 wt% tantalum: Microstructure and mechanical properties. *J Alloys Compd*. 2016;660:461-470.

doi: 10.1016/j.jallcom.2015.11.141

72. Ataee A, Li Y, Wen C. A comparative study on the nanoindentation behavior, wear resistance and *in vitro* biocompatibility of SLM manufactured CP–Ti and EBM manufactured Ti64 gyroid scaffolds. *Acta Biomater*. 2019;97:587-596.

doi: 10.1016/j.actbio.2019.08.008

73. Gómez S, Vlad MD, López J, Fernández E. Design and properties of 3D scaffolds for bone tissue engineering. *Acta Biomater*. 2016;42:341-350.

doi: 10.1016/j.actbio.2016.06.032

74. Zieliński TG, Opiela KC, Pawłowski P, *et al.* Reproducibility of sound-absorbing periodic porous materials using additive manufacturing technologies: Round robin study. *Addit Manufact*. 2020;36:101564.

doi: 10.1016/j.addma.2020.101564

75. Kou XY, Tan ST. A simple and effective geometric representation for irregular porous structure modeling. *Comput Aided Des*. 2010;42:930-941.

doi: 10.1016/j.cad.2010.06.006

76. Zhao J, Zhang M, Zhu Y, Li X, Wang L, Hu C. Concurrent optimization of additive manufacturing fabricated lattice structures for natural frequencies. *Int J Mech Sci*. 2019;163:105153.

doi: 10.1016/j.ijmecsci.2019.105153

77. Ma S, Song K, Lan J, Ma L. Biological and mechanical property analysis for designed heterogeneous porous scaffolds based on the refined TPMS. *J Mech Behav Biomed Mater*. 2020;107:103727.

doi: 10.1016/j.jmbbm.2020.103727

78. Lv Y, Wang B, Liu G, *et al.* Design of bone-like continuous gradient porous scaffold based on triply periodic minimal surfaces. *J Mater Res Technol*. 2022;21:3650-3665.

doi: 10.1016/j.jmrt.2022.10.160

79. Lv Y, Guo J, Zhang Q, Wei G, Yu H. Design of low elastic modulus and high strength TC4 porous scaffolds via new variable gradient strategies. *Mater Lett*. 2022;325:132616.

doi: 10.1016/j.matlet.2022.132616

80. Zhao D, Huang Y, Ao Y, *et al*. Effect of pore geometry on the fatigue properties and cell affinity of porous titanium scaffolds fabricated by selective laser melting. *J Mech Behav Biomed Mater*. 2018;88:478-487.

doi: 10.1016/j.jmbbm.2018.08.048

81. *Novel-Ink-Based Direct Ink Writing of Ti6al4v Scaffolds with Sub-300 μm Structural Pores for Superior Cell Proliferation And Differentiation - Xu - Advanced Healthcare Materials*. Wiley Online Library, (n.d.). Available from: https://onlinelibrary.wiley.com/doi/abs/10.1002/adhm.202302396 [Last accessed on 2024 Jan [13].

82. Zhao G, Shao X, Zhang Q, *et al*. Porous bio-high entropy alloy scaffolds fabricated by direct ink writing. *J Mater Sci Technol*. 2023;157:21-29.

doi: 10.1016/j.jmst.2023.02.015

83. Li Z, Yang F, Wang H, Li Y, Chen C, Guo Z. Direct ink writing of porous Ti6Al4V alloys via UV light curing. *Adv Eng Mater*. 2022;24:2200176.

doi: 10.1002/adem.202200176

84. Coffigniez M, Gremillard L, Balvay S, Lachambre J, Adrien J, Boulnat X. Direct-ink writing of strong and biocompatible titanium scaffolds with bimodal interconnected porosity. *Addit Manuf*. 2021;39:101859.

doi: 10.1016/j.addma.2021.101859

85. *Direct ink Writing to Fabricate Porous Acetabular Cups from Titanium Alloy. Bio-Design and Manufacturing*, (n.d.). Available from: https://link.springer.com/article/10.1007/s42242-022-00222-2 [Last accessed on 2024 Jan [13].

86. Xu Q, Gabbitas B, Matthews S, Zhang D. The development of porous titanium products using slip casting. *J Mater Process Technol*. 2013;213:1440-1446.

doi: 10.1016/j.jmatprotec.2013.03.011

87. Liu Y, Jiang G, He G. Enhancement of entangled porous titanium by BisGMA for load-bearing biomedical applications. *Mater Sci Eng C Mater Biol Appl*. 2016;61:37-41.

doi: 10.1016/j.msec.2015.12.018

88. Fiocchi J, Tuissi A, Biffi CA. Heat treatment of aluminium alloys produced by laser powder bed fusion: A review. *Mater Des*. 2021;204:109651.

doi: 10.1016/j.matdes.2021.109651

89. Chen LY, Liang SX, Liu Y, Zhang LC. Additive manufacturing of metallic lattice structures: Unconstrained design, accurate fabrication, fascinated performances, and challenges. *Mater Sci Eng R Rep.* 2021;146:100648.

doi: 10.1016/j.mser.2021.100648

90. Zhang LC, Chen LY, Wang L. Surface modification of titanium and titanium alloys: Technologies, developments, and future interests. *Adv Eng Mater*. 2020;22:1901258.

doi: 10.1002/adem.201901258

91. Fang Y, Wang Q, Yang Z, *et al*. An efficient approach to endow TiNbTaZr implant with osteogenic differentiation and antibacterial activity *in vitro*. *Mater Des*. 2022;221:110987.

doi: 10.1016/j.matdes.2022.110987

92. Guo Y, Hu B, Tang C, *et al*. Increased osteoblast function *in vitro* and *in vivo* through surface nanostructuring by ultrasonic shot peening. *Int J Nanomed*. 2015;10:4593-4603.

doi: 10.2147/IJN.S83788

93. Sypniewska J, Szkodo M. Influence of laser modification on the surface character of biomaterials: Titanium and its alloys-a review. *Coatings*. 2022;12:1371.

doi: 10.3390/coatings12101371

94. Surmeneva MA, Khrapov D, Prosolov K, *et al.* The influence of chemical etching on porous structure and mechanical properties of the Ti6AL4V Functionally Graded Porous Scaffolds fabricated by EBM. *Mater Chem Phys*. 2022;275:125217.

doi: 10.1016/j.matchemphys.2021.125217

95. Civantos A, Domínguez C, Pino RJ, *et al*. Designing bioactive porous titanium interfaces to balance mechanical properties and *in vitro* cells behavior towards increased osseointegration. *Surf Coat Technol*. 2019;368:162-174.

doi: 10.1016/j.surfcoat.2019.03.001

96. Wang D, He G, Tian Y, Ren N, Liu W, Zhang X. Dual effects of acid etching on cell responses and mechanical properties of porous titanium with controllable open-porous structure. *J Biomed Mater Res*. 2020;108:2386-2395.

doi: 10.1002/jbm.b.34571

97. Montazerian M, Hosseinzadeh F, Migneco C, Fook MVL, Baino F. Bioceramic coatings on metallic implants: An overview. *Ceram Int*. 2022;48:8987-9005.

doi: 10.1016/j.ceramint.2022.02.055

98. Wang X, Li Y, Hodgson PD, Wen C. Biomimetic modification of porous TiNbZr alloy scaffold for bone tissue engineering. *Tissue Eng A*. 2010;16:309-316.

doi: 10.1089/ten.tea.2009.0074

99. Chudinova E, Koptyug A, Mukhortova Y, *et al*. Functionalization of additive-manufactured Ti6Al4V scaffolds with poly(allylamine hydrochloride)/poly(styrene sulfonate) bilayer microcapsule system containing dexamethasone. *Mater Chem Phys*. 2021;273:125099.

doi: 10.1016/j.matchemphys.2021.125099

100. Li L, Li Y, Yang L, *et al*. Polydopamine coating promotes early osteogenesis in 3D printing porous Ti6Al4V scaffolds. *Ann Transl Med*. 2019;7:240.

doi: 10.21037/atm.2019.04.79

101. Jiao Y, Li X, Zhang X, *et al*. Silver antibacterial surface adjusted by hierarchical structure on 3D printed porous titanium alloy. *Appl Surf Sci*. 2023;610:155519.

doi: 10.1016/j.apsusc.2022.155519

102. Vignesh R, Sakthinathan G, Velusamy R, Ramakrishna S. An *in-vitro* evaluation study on the effects of surface modification via physical vapor deposition on the degradation rates of magnesium-based biomaterials. *Surf Coat Technol*. 2021;411:126972.

doi: 10.1016/j.surfcoat.2021.126972

103. Diez-Escudero A, Andersson B, Carlsson E, *et al*. 3D-printed porous Ti6Al4V alloys with silver coating combine osteocompatibility and antimicrobial properties. *Biomater Adv*. 2022;133:112629.

doi: 10.1016/j.msec.2021.112629

104. Wang F, Wang L, Feng Y, *et al*. Evaluation of an artificial vertebral body fabricated by a tantalum-coated porous titanium scaffold for lumbar vertebral defect repair in rabbits. *Sci Rep*. 2018;8:8927.

doi: 10.1038/s41598-018-27182-x

105. *MetalsFree Full-Text Electrochemical Surface Treatment of a β-titanium Alloy to Realize an Antibacterial Property and Bioactivity,* (n.d.). Available from: https://www.mdpi.com/2075-4701/6/4/76 [Last accessed on 2024 Jan [13].

106. Vidal E, Guillem-Marti J, Ginebra MP, Combes C, Ruperez E, Rodriguez D. Multifunctional homogeneous calcium phosphate coatings: Toward antibacterial and cell adhesive titanium scaffolds. *Surf Coat Technol*. 2021;405:126557.

doi: 10.1016/j.surfcoat.2020.126557

107. Guo Y, Ren L, Xie K, *et al*. Functionalized TiCu/Ti-Cu-N-coated 3D-printed porous Ti6Al4V scaffold promotes bone regeneration through BMSC recruitment. *Adv Mater Interf*. 2020;7:1901632.

doi: 10.1002/admi.201901632

108. Zhang Z, Li Y, He P, *et al*. Nanotube-decorated hierarchical tantalum scaffold promoted early osseointegration. *Nanomedicine*. 2021;35:102390.

doi: 10.1016/j.nano.2021.102390

109. Shokuhfar T, Hamlekhan A, Chang JY, Choi CK, Sukotjo C, Friedrich C. Biophysical evaluation of cells on nanotubular surfaces: The effects of atomic ordering and chemistry. *Int J Nanomedicine*. 2014;9:3737-3748.

doi: 10.2147/IJN.S67344

110. Makurat-Kasprolewicz B, Ossowska A. Recent advances in electrochemically surface treated titanium and its alloys for biomedical applications: A review of anodic and plasma electrolytic oxidation methods. *Mater Today Commun*. 2023;34:105425.

doi: 10.1016/j.mtcomm.2023.105425

111. Liang CY, Jiang XJ, Ji RL, *et al*. Preparation and surface modification of 3D printed Ti–6Al–4V porous implant. *Rare Met*. 2021;40:1164-1172.

doi: 10.1007/s12598-020-01413-5

112. Li G, Ma F, Liu P, *et al*. Review of micro-arc oxidation of titanium alloys: Mechanism, properties and applications. *J Alloys Compd*. 2023;948:169773.

doi: 10.1016/j.jallcom.2023.169773

113. Ming X, Wu Y, Zhang Z, Li Y. Micro-arc oxidation in titanium and its alloys: Development and potential of implants. *Coatings*. 2023;13:2064.

doi: 10.3390/coatings13122064

114. Wen X, Liu Y, Xi F, Zhang X, Kang Y. Micro-arc oxidation (MAO) and its potential for improving the performance of titanium implants in biomedical applications. *Front Bioeng Biotechnol*. 2023;11:1282590.

doi: 10.3389/fbioe.2023.1282590

115. Yan Y, Sun J, Han H, Li D, Cui K. Microstructure and bioactivity of Ca, P and Sr doped TiO2 coating formed on porous titanium by micro-arc oxidation. *Surf Coat Technol*. 2010;205:1702-1713.

doi: 10.1016/j.surfcoat.2010.09.040

116. Sun X, Tong S, Yang S, Guo S. The effects of graphene on the biocompatibility of a 3D-printed porous titanium alloy. *Coatings*. 2021;11:1509.

doi: 10.3390/coatings11121509

117. Huang H, Wu Z, Yang Z, *et al*. *In vitro* application of drug-loaded hydrogel combined with 3D-printed porous

scaffolds. *Biomed Mater*. 2022;17:065019.

doi: 10.1088/1748-605X/ac9943

118. Chen H, Feng R, Xia T, *et al*. Progress in surface modification of titanium implants by hydrogel coatings. *Gels*. 2023;9:423.

doi: 10.3390/gels9050423

119. Bai H, Cui Y, Wang C, *et al*. 3D printed porous biomimetic composition sustained release zoledronate to promote osteointegration of osteoporotic defects. *Mater Des*. 2020;189:108513.

doi: 10.1016/j.matdes.2020.108513

120. Yu L, Wu Y, Liu J, *et al.* 3D Culture of bone marrow-derived mesenchymal stem cells (BMSCs) could improve bone regeneration in 3D-printed porous Ti6Al4V scaffolds. *Stem Cells Int*. 2018;2018:2074021.

doi: 10.1155/2018/2074021

121. Qiao S, Sheng Q, Li Z, *et al*. 3D-printed Ti6Al4V scaffolds coated with freeze-dried platelet-rich plasma as bioactive interface for enhancing osseointegration in osteoporosis. *Mater Des*. 2020;194:108825.

doi: 10.1016/j.matdes.2020.108825

122. Kumar A, Nune KC, Misra RDK. Biological functionality and mechanistic contribution of extracellular matrix-ornamented three dimensional Ti-6Al-4V mesh scaffolds. *J Biomed Mater Res*. 2016;104:2751-2763.

doi: 10.1002/jbm.a.35809

123. Croes M, Bakhshandeh S, Van Hengel IAJ, *et al*. Antibacterial and immunogenic behavior of silver coatings on additively manufactured porous titanium. *Acta Biomater*. 2018;81:315-327.

doi: 10.1016/j.actbio.2018.09.051

124. Wei X, Chen Q, Bu L, *et al*. Improved muscle regeneration into a joint prosthesis with mechano-growth factor loaded within mesoporous silica combined with carbon nanotubes on a porous titanium alloy. *ACS Nano.* 2022;16:14344-14361.

doi: 10.1021/acsnano.2c04591

125. Jiang P, Zhang Y, Shi B, *et al*. Advanced surface engineering of titanium materials for biomedical applications: From static modification to dynamic responsive regulation. *Bioact Mater*. 2023;27:15-57.

doi: 10.1016/j.bioactmat.2023.03.006

126. Wu H, Dong H, Tang Z, *et al*. Electrical stimulation of piezoelectric BaTiO3 coated Ti6Al4V scaffolds promotes anti-inflammatory polarization of macrophages and bone repair via MAPK/JNK inhibition and OXPHOS activation. *Biomaterials*. 2023;293:121990.

doi: 10.1016/j.biomaterials.2022.121990

127. Lascano S, Chávez-Vásconez R, Muñoz-Rojas D, *et al*. Graphene-coated Ti-Nb-Ta-Mn foams: A promising approach towards a suitable biomaterial for bone replacement. *Surf Coat Technol*. 2020;401:126250.

doi: 10.1016/j.surfcoat.2020.126250

ACCSCIENCE PUBLISHING

Materials Science in Additive Manufacturing

ORIGINAL RESEARCH ARTICLE

Effects of carbon content on precipitate evolution and crack susceptibility in additively manufactured IN738LC

Zhongji Sun[1]*, Verner Soh[1], Coryl Lee[1], Delvin Wuu[1], Desmond Lau[1], Siyuan Wei[1], Chee Koon Ng[1], Swee Leong Sing[2], Dennis Tan[1], and Pei Wang[1,3]*

[1]Institute of Materials Research and Engineering (IMRE), Agency for Science, Technology and Research (A*STAR), Singapore, Republic of Singapore

[2]Department of Mechanical Engineering, National University of Singapore, Singapore, Republic of Singapore

[3]Engineering Cluster, Singapore Institute of Technology, Singapore, Republic of Singapore

Abstract

Hot cracking is a major bottleneck preventing the additive manufacturing community from adopting precipitation-strengthened nickel-base superalloys, such as the IN738LC. Prior literature demonstrates the beneficial outcome of increasing the carbon content within IN738LC to alleviate its hot cracking problem. However, the effect of carbon content on the gamma prime precipitation and grain recrystallization was not fully addressed. Here, we fabricated five sample sets of IN738LC with different carbon contents and subjected these samples to two separate heat treatment processes. The precipitate and grain evolution were monitored under the backscattered electron imaging and electron backscattered diffraction studies. While the carbon addition could assist in addressing the hot cracking problem, horizontal delamination cracks were detected during the fabrication of large samples when the overall carbon content was above 0.4 wt.%, highlighting the need for care when introducing carbon for the purpose of resolving hot cracking.

Keywords: Additive manufacturing; Cracking; Nickel-base superalloy; Carbon

***Corresponding authors:** Zhongji Sun (sun_zhongji@imre.a-star.edu.sg) Pei Wang (wangp@imre.a-star.edu.sg)

Citation: Sun Z, Soh V, Lee C, *et al*. Effects of carbon content on precipitate evolution and crack susceptibility in additively manufactured IN738LC. *Mater Sci Add Manuf*. 2024;3(1):2264. doi: 10.36922/msam.2264

Received: November 16, 2023

Accepted: January 8, 2024

Published Online: February 19, 2024

1. Introduction

Precipitation-strengthened nickel-base superalloy IN738LC was originally designed as an investment casting alloy[1]. It contains a high-volume fraction (about 45 %) of the coherent $L1_2$ Ni_3(Al, Ti) gamma prime (γ') precipitates,[2] which provides the material with excellent high-temperature (up to 980°C) resistance to hot corrosion and desired mechanical properties,[3,4] enabling the alloy to serve as critical components within the hot sections of land-based and aero gas turbines.[5,6] The envisioned benefits of one-step near-net-shape production of this material through additive manufacturing (AM) have driven many research efforts for the past half-decade.[7-9] If successful, the AM approach could save on raw material feedstock and eliminate the need for post-machining, which is a considerable cost for such an expensive and difficult-to-machine hard alloy.[10] However, under AM's rapid solidification conditions, for example, laser powder bed fusion (LPBF), IN738LC is prone to hot cracking.[11,12]

Prior studies illustrate that one potential method to eliminate the problem of hot cracks in this alloy is through the addition of carbon, as the formation of carbides serves as trapping sites for the hot-crack-promoting element, that is, boron.[13] The role of carbon has long been a debatable topic within the nickel-base superalloy community. First, carbon segregation along grain boundaries was reported to improve the grain boundary strength.[14] As a result, the concurrent improvement in the material's room temperature and high-temperature tensile strength (5 – 6%) and elongation (30 – 50%) was observed on several occasions.[15,16] However, low-temperature and high-stress creep tests show that the increase in carbon content has a detrimental effect. The excessive carbon content leads to enlarged carbides, which facilitate the formation of gas pores and subsequently result in a large primary creep strain and short rupture life.[17] Second, carbon was found to prevent oxide formation during the material's melting stage, improving the overall melt's cleanliness.[18] Yet, during service under a high-temperature environment, the oxidation of carbide itself could introduce plastic deformations and contribute to soft recrystallized regions nearby, serving as crack initiation sites.[19] Finally, metastable carbides at low temperatures are effective trapping sites, either for hydrogen or boron, to prevent hydrogen embrittlement and solidification defects.[20] However, brittle topologically close-packed (TCP) phases tend to form on the carbide decomposition at high temperatures, leading to pre-mature material failure under loading.[21]

Besides the effect of carbon on the performance of nickel-base superalloys, its interaction with γ' precipitation is also another subject worth investigating. The γ' phase within those LPBF-built IN738LC only appears during heat treatment (HT).[6] It is believed that the additional carbon will induce competitive precipitation between the carbide and γ'.[22] Hence, an optimization of the HT process due to the additional carbon addition might be necessary. Conventionally, the as-cast IN738LC goes through a classic two-step HT, with a solutionization HT at 1120°C for 2 h, followed by 24 h aging HT at 845°C.[23] Several studies have reported on the inadequacy of this conventional two-step HT toward recrystallization and suggested that a stress-relief HT at 845°C for 24 h before the two-step HT is required to lower the temperature threshold for recrystallization.[24] Past literature suggests that for IN738LC alloys, a unimodal fine γ' precipitation or a bimodal γ' precipitation with the size of the finer γ' below 100 nm is desirable for both the room-temperature and high-temperature (up to 850°C) tensile properties.[25] To obtain such a fine γ', the aging temperature needs to be at least 1120 °C to trigger the mechanism of "precipitate refinement by solution HT."[26] Hence, there is still plenty of room for improvement to optimize the HT processes for LPBF-built IN738LC alloys.

In this study, we fabricated five sample sets of IN738LC alloys with different carbon contents through the LPBF approach and subjected the as-built samples to different HT cycles. The evolution of the carbide and γ' precipitation was closely monitored after each procedure, including their microhardness and tensile properties. Moreover, the less-reported issues of delamination cracking during the fabrication process are also presented and discussed toward the end.

2. Methods

2.1. Sample fabrication

A Trumpf TruPrint 1000 LPBF machine was employed for fabricating the IN738LC samples in the present study. The equipment has a laser source with a wavelength of 1070 nm and a laser spot size of 30 μm. Five sample sets with different carbon (C) concentrations ranging from 0 to 0.4 wt.% were produced, with a 0.1 wt.% carbon interval between each sample set. The IN738LC powders were obtained from Shanghai Truer Industrial Development Co., Ltd, with a powder size ranging from 15 to 53 μm. Its chemical composition is listed in Table 1. Graphite powders were purchased from Nanografi Nano Technology, having an average powder size of ~1 μm. The powders were mixed in a roller mill (BMU-100-3) for 12 h, with a rotational speed of 180 rpm. Before sample production, the powders were dried in a vacuum at 60°C for 24 h. A chessboard laser scan strategy was adopted for the actual production, with an individual island dimension of 4 × 4 mm^2, a layer thickness of 20 μm, hatch spacing of 90 μm, a laser scanning speed of 1200 mm/s, and a laser power input of 115 W and 130 W, respectively.

Blocks with a size of 10 × 10 × 25 mm^3 were fabricated in a graded structure format from 0 wt.% carbon to 0.4 wt.% carbon, with each composition having a 5 mm height (Figure 1A), under an oxygen concentration of about 100 ppm. The different powder compositions were loaded into the powder storage unit within the LPBF machine sequentially; therefore, the graded structure could be produced in a single production run.

2.2. Material characterization and HT

All as-built specimens were removed from the substrate through electric discharge machining. The specimens were mounted in PolyFast carbon resin and grounded with SiC-paper of grit in the descending order of #220, #500, #1000, #2000, and #4000, respectively. Subsequently, a polishing step with MD-Dac (DiaPro Dac 3 μm suspension) and MD-Nap (DiaPro Nap 1 μm suspension) was carried out,

Table 1. Chemical composition of IN738LC powders

wt.%	Cr	Co	Al	Ti	W	Nb	Ta	Si	Zr	C	B	Ni
IN738LC	16.06	8.61	3.54	3.58	2.65	0.97	1.69	0.032	0.031	0.124	0.0086	Bal

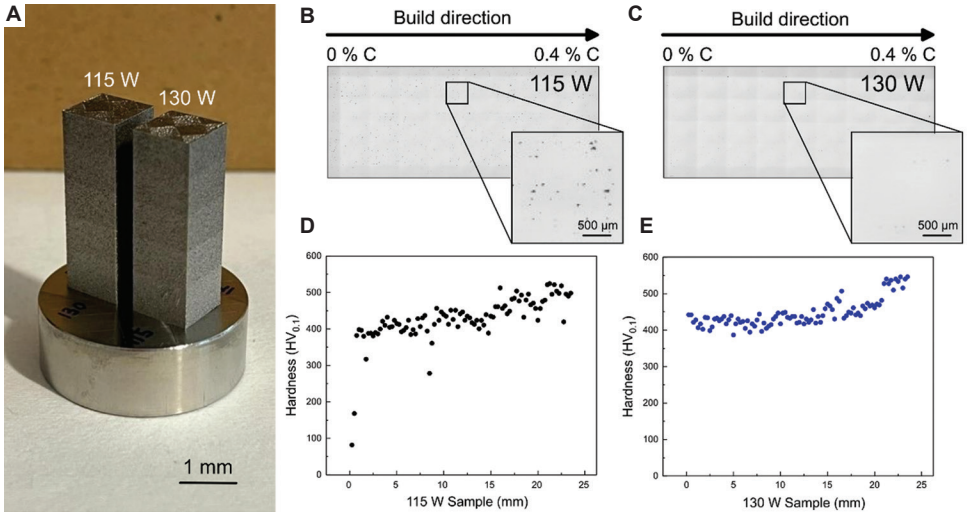

Figure 1. The effect of laser power, 115 W and 130 W, on the density and microhardness of IN738LC samples mixed with different amounts of carbon, from 0 to 0.4 wt.%. (A) The actual as-built samples. (B and C) The optical image and (D and E) microhardness evolution along the build direction of these specimens.

followed by Vibratory polishing (MasterMet colloidal silica suspension).

Optical microscopy (OM) examination was conducted using an Olympus BX53M microscope equipped with Olympus stream motion 2.3.3 software. Scanning electron microscopy and electron backscattered diffraction were performed using a JEOL JSM-IT500HR equipped with an Oxford Symmetry detector, using an accelerating voltage of 20 kV and a step size of 1 µm. Bruker D8 discover diffractometer was employed for the X-ray crystallography (XRD) study, with a Cu Kα radiation and 2D Vantec detector.

Only specimens built with the 130 W laser power input were subjected to subsequent HT in the QSXL-1616 box-type electric furnace due to its higher relative density (to be shown in Section 3.1). For HT studies, specimens with different compositions were machined into smaller blocks of 2.0 × 4.5 × 1.0 mm. In total, two HT procedures were adopted to optimize the grain recrystallization and gamma prime (γ') morphology, namely, the two-step HT and the three-step HT. The two-step HT process mimics the standard industrial practice of post-processing the conventionally made IN738LC. The material first goes through a solution treatment at 1120°C for 2 h, with the intention of dissolving any previously present γ'. Then, an aging process is conducted at 845°C for 24 h to promote γ' precipitations.[27] However, literature results showed that LPBF-built IN738LC does not have any γ' in its as-built state, as they are kinetically suppressed.[28] Thus, the γ' dissolution treatment no longer justifies its presence.

The three-step HT was conceived in this study to promote grain recrystallization and avoid the anisotropic performance of the LPBF-produced samples. The three-step HT began with a stress-relief procedure at 845°C for 24 h, which has shown to be effective in lowering the threshold temperature for recrystallization during HT.[24] Subsequently, the stress-relieved specimens were held at 1200°C for 4 h before being placed at a temperature of 1120°C for 24 h to promote a bimodal γ' distribution, with the fine γ' having a size below 100 nm.[26] All heating processes use a constant heating rate of 10°C/min. Water quenching was adopted after each HT step.

Microhardness tests were carried out on the Innovatest Falcon 5000 machine, using a 0.1 kg and 1.0 kg load, respectively, with a holding time of 15 s. At least, ten indents were placed on each specimen. Tensile specimens have a gauge length of 20 mm, gauge width of 8 mm, and gauge thickness of 1 mm. They are machined from the larger, as-built rectangular blocks. Tensile studies were conducted on an Instron Mechanical Tester 5569 machine, using a nominal strain rate of 0.3 mm/min.

3. Results

3.1. Laser processing parameter optimization

LPBF fabrications using five different combinations of powders were conducted within the same build platform (Figure 1A), with the bottom of the build being pure IN738LC, followed by IN738LC with 0.1 wt.% carbon. The carbon content sequentially increased, and the top-most portion was IN738LC with 0.4 wt.% carbon. The OM images of samples fabricated using two different laser powers are shown in Figure 1B (115 W) and Figure 1C (130 W). The specimen made from 115 W depicts uniformly distributed pores, with a density value of 99.35% measured through OM image analysis. The size of the pores is mostly below 100 μm, as illustrated from the enlarged view in Figure 1B. In comparison, the specimen fabricated with a 130 W laser power input had much fewer and smaller pores, with a density value of 99.95%, obtained from the same analysis approach. The effect of carbon content on microhardness under the two laser power inputs is shown in Figure 1D (115 W) and Figure 1E (130 W), respectively. For both builds, the microhardness value increases concurrently with the carbon content, ranging from ~380 HV to ~530 HV for 115 W and from ~400 HV to ~ 550 HV for 130 W, indicating that the higher power gives the as-built samples a higher microhardness. Due to a larger number of pores within the 115 W build, its microhardness results show a greater degree of scatter (Figure 1D), with the lowest microhardness value recorded being <100 HV, which likely occurred when the microhardness indents fell near those pre-existing pores.

3.2. Evolution of γ' and carbide under different processing and HT conditions

Only specimens fabricated with the 130 W laser power input were subjected to subsequent characterization due to their superior density of 99.95%. The γ' and carbide characteristics of the as-built specimens were examined under the backscattered electron (BSE) imaging condition (Figure 2). Out of the five different compositions, only three alloys were examined in detail, that is, the pure IN738LC, IN738LC with 0.1 wt.% carbon, and IN738LC with 0.3 wt.% carbon. This is because the trend on the effect of carbon addition is consistent among all specimens. In general, the grain boundaries have a zig-zag morphology and are interlocking with one another (Figure $2A_1$–C_1). The grains were not uniform in color due to the intragranular rotations induced by inherent residual stresses incurred during LPBF's cyclic heating.[29] With the increase in carbon content, the number of carbides (bright spherical dots under the BSE imaging) was found to increase monotonously along the cellular boundaries (Figure $2A_2$–C_2). The carbides were previously found to be titanium carbide (TiC), thus appearing bright under the BSE condition.[13] The size of these cellular structures was approximated to be around 500 nm, consistent with the previous reports.[13] For pure IN738LC, the MC carbides were isolated from one another, and the distance between individual carbides was reduced with the increment of carbon content (Figure $2A_3$–C_3). For alloy with 0.3 wt.% carbon, the carbides occupied almost the entire cellular boundaries and formed a carbide ring (Figure $2C_3$).

After the standard two-step HT, more carbides started to precipitate out, mostly along the grain boundaries of these three specimens, again appearing as bright dots (Figure $3A_1$–C_1). The contrast within individual grains became more uniform than their as-built state. The amount of γ' is inversely proportional to the carbon content, with the pure IN738LC and the IN738LC with 0.1 wt.% carbon samples having densely packed γ' (black phases in Figure $3A_2$ and B_2), and the sample with 0.3 wt.% carbon having a much lower quantity of γ' (Figure $3C_2$). The first two samples demonstrate a bimodal γ' distribution, with the bigger γ' having a diameter of about 200 to 400 nm and the smaller γ' having a diameter of around 100 nm (Figure $3A_3$ and B_3). For the IN738LC sample mixed with 0.3 wt.% carbon, the smaller carbides are not clearly visible under the current imaging condition (Figure $3C_3$). It is speculated that the missing γ' could be deprived of their essential solute elements due to the competitive nucleation and growth of MC carbides.

Straight annealing twins were present within the pure IN738LC alloy after the three-step HT process proposed in this paper (Figure $4A_1$). Its grain boundaries were no longer tortuous but mostly smooth. The presence of MC carbides (those white dots) was more apparent than its as-built and two-step HT-processed counterparts. For the IN738LC samples added with 0.1 wt.% and 0.3 wt.% carbon, the accumulation of carbides (bright spots) along their grain boundaries was clearly visible (Figure $4B_1$ and C_1). The higher temperature and longer duration designed in the three-step HT caused the γ' to grow further, reaching a peak diameter of around 600 to 800 nm (Figure $4A_2$). In conjunction, the MC carbide also reached a maximum dimension of around 500 nm. With a higher carbon content, the maximum size of γ' and those intragranular carbides decreased (Figure $4B_2$ and C_2). While the larger γ' in the three-step HT is about twice the size of those in the two-step HT, the smaller γ' in the three-step HT is about half the size of those in the two-step HT, having an average size of ~60 nm for the pure IN738LC (Figure $4A_3$). A similar trend in the refinement of γ' in the three-step HT was also observed for the other two alloys (Figure $4B_3$ and C_3).

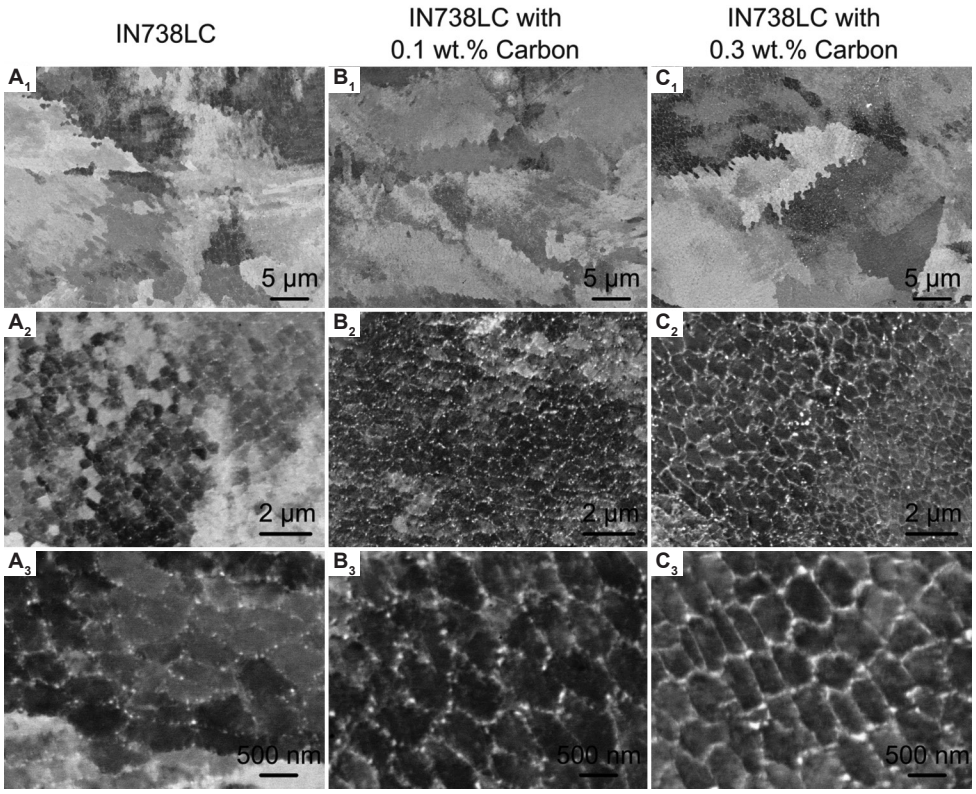

Figure 2. Backscattered electron imaging of the as-built specimens at different magnifications for (A_1–A_3) pure IN738LC, (B_1–B_3) IN738LC with 0.1 wt.% carbon, and (C_1–C_3) IN738LC with 0.3 wt.%. Bright spots are the MC carbides.

3.3. Phase constituents and grain recrystallization during HTs

The XRD results of the samples under the as-built, two-step HT, and three-step HT conditions are shown in Figure 5A–C. Within the XRD graphs, the orange diamond represents the γ/γ' phase, while the blue circle and yellow star are the MC and $M_{23}C_6$ carbides, respectively. Right after the LPBF production, the XRD profile suggests that the pure IN738LC mainly consists of a single γ/γ' phase, which cannot be distinguished based on the XRD technique alone due to their close lattice spacing (Figure 5A). However, based on the previous BSE results, we know that it, in fact, only contains the γ phase, as the γ' is kinetically suppressed during the solidification process. With the addition of increasing carbon, the MC carbide peak became more obvious, consistent with a previous report that after rapid solidification for IN738LC, the precipitated carbon tends to form MC carbides.[13] After the industrial standard two-step HT, we started to observe MC carbides in the pure IN738LC sample. As the carbon content increased, the intensity of the MC carbide peaks became stronger (Figure 5B). When mixing with 0.4 wt.% carbon, an additional $M_{23}C_6$ peak (yellow star)[30] was found for the two-step HT. This was the only $M_{23}C_6$ carbide peak detected within this study, but its intensity was relatively low. As for the three-step HT, due to its higher HT temperature and longer HT duration, there were more MC carbide peaks with higher intensities (Figure 5C). Overall, despite the different HT processes adopted, MC carbide is the dominant precipitate within the LPBF-produced IN738LC.

The inverse pole figure maps of the previously mentioned samples are shown in Figure 6. All maps were computed with a viewing direction along the build direction and a scan area of 500 × 500 μm^2. Under the as-built condition, all specimens demonstrated a classic columnar grain structure, growing parallel to the heat flow direction[31] (Figure 6A_1–C_1). The specimen with the highest carbon content (0.3 wt.%) seems to have more <110>-oriented grains in green (Figure 6C_1). After the standard two-step HT process, no discernible changes were observed for the pure IN738LC and IN738LC mixed with 0.1 wt.% carbon in terms of their grain morphologies or crystallographic textures (Figure 6A_2 and B_2). The intragranular rotations, typical for LPBF-built samples,[32] are still present. However, for the specimen blended with 0.3 wt.% carbon, grain growth was evident, and the <110> grains expanded at the expense of other grains with a different crystallographic orientation (Figure 6C_2).

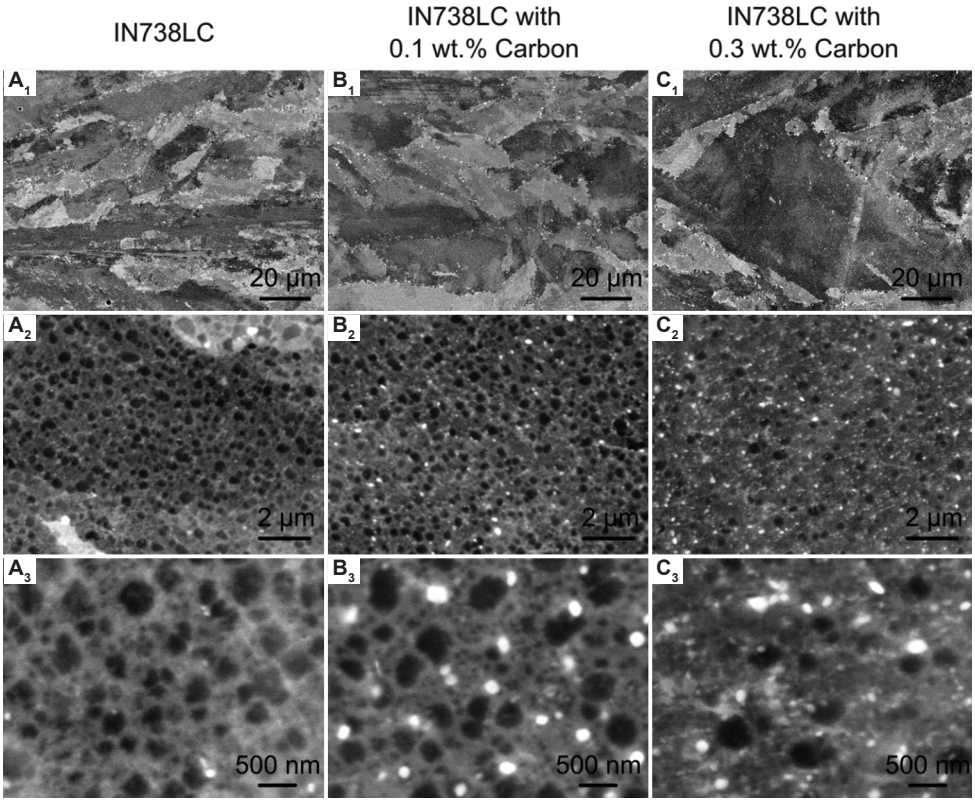

Figure 3. Backscattered electron imaging of specimens after the industrial standard two-step HT at different magnifications for (A_1–A_3) pure IN738LC, (B_1–B_3) IN738LC with 0.1 wt.% carbon, and (C_1–C_3) IN738LC with 0.3 wt.%. Bright spots are MC carbides and dark precipitates are γ'.

For the three-step HT, the pure IN738LC had a vastly different grain morphology. Columnar grains changed into equiaxed grains encompassing straight annealing twins (Figure $6A_3$). Such a microstructure is envisioned to be beneficial for providing an isotropic property when the material is strained under different loading directions. With an increment of 0.1 wt.% of carbon within the base alloy, the material failed to make this columnar-to-equiaxed transition but retained its columnar grain shape, though the grain size enlarged with more <110> crystallographic orientations (Figure $6B_3$). As for the specimen with 0.3 wt.% of carbon, the three-step HT did not yield a huge difference in comparison to the prior two-step HT (Figure $6C_2$ and C_3). The sample was still mostly made of large columnar <110> orientated grains along the build direction.

4. Discussion

The aim of the present work is to explore the feasibility of eliminating the hot cracking problem within LPBF-built precipitation-strengthened IN738LC by increasing its carbon content. This approach is mainly inspired by the previous study,[13] which shows that carbides are effective trapping sites for the hot-crack-promoting element, boron. Despite its promising result on hot crack elimination and ease of application, there are several potential problems associated with this method. First, it is the viability of having sufficient γ' precipitates, as the increased carbon content will yield more carbides, thus competing for those essential γ' forming elements. Second, carbides are also known for their pinning effect in nickel-base superalloys, as they prevent the migration of recrystallization grain boundaries, thus hampering grain recrystallization.[33] Third, while having more carbides should assist in the eradication of hot cracks during solidification,[34,35] when existing in abundance, their brittle nature might cause large delamination cracks under the inherent residual stresses present in the LPBF's cyclic heating cycles.[36] In this study, we addressed each of these potential problems sequentially.

As shown in Figures 2–4, the characteristics of γ' are strongly correlated with the carbon content and the HT procedures. In the as-built state, we did not observe γ' in any of the three samples. All as-built specimens have a cellular microstructure with a cell size of around 500 nm, typical for LPBF-built nickel-base superalloys.[37] Carbides

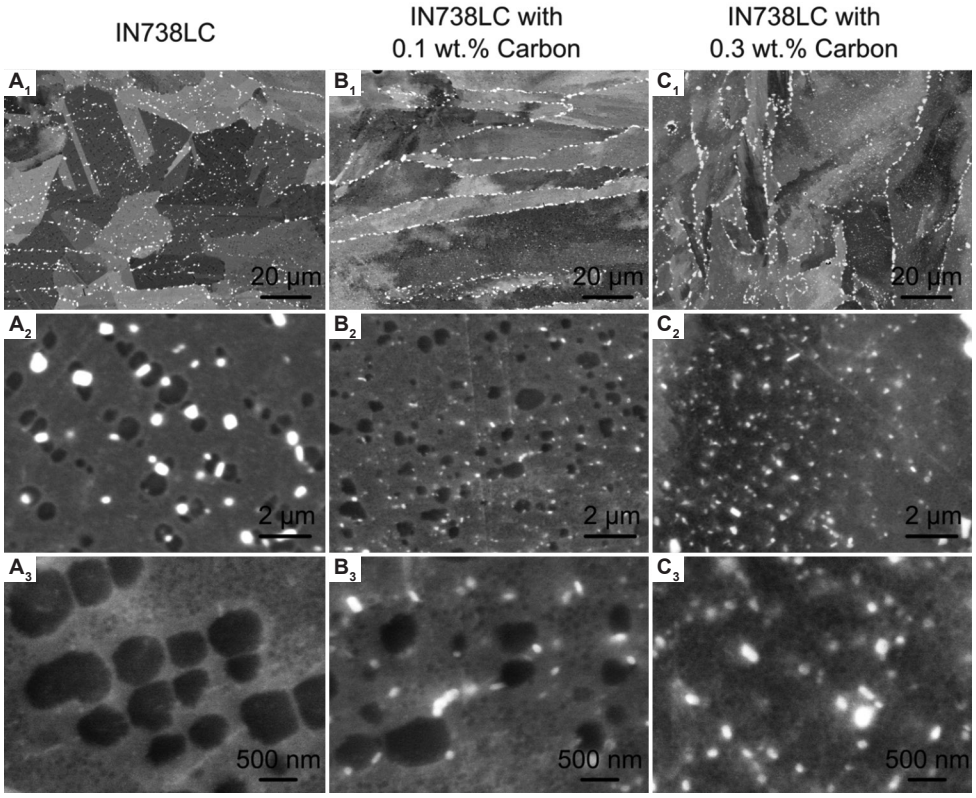

Figure 4. Backscattered electron imaging of specimens after the proposed three-step HT at different magnifications for (A_1–A_3) pure IN738LC, (B_1–B_3) IN738LC with 0.1 wt.% carbon, and (C_1–C_3) IN738LC with 0.3 wt.%.

are mainly observed within the interdendritic/cellular boundaries, which can be ascribed to the high partitioning coefficient of carbon within the matrix gamma phase.[13] With the adoption of a conventional two-step HT, the addition of 0.1 wt.% carbon did not seem to alter the γ' morphologies to a large extent (Figure 3A_3 and B_3). The size and distribution of γ' are rather similar to the pure IN738LC, which underwent the same two-step HT process. The density of MC carbides did increase with the addition of carbon, but γ' was still the dominant precipitate within the sample (Figure 3B_3).

However, the same cannot be said for the alloy with 0.3 wt.% carbon addition. After the standard two-step HT, the number density of the larger γ' was greatly reduced, estimated to be less than 50% of those in the pure IN738LC by visual inspection (Figure 3B_3). Under a higher magnification, those smaller γ' can no longer be detected (Figure 3C_3). Instead, smaller carbides were observed. It is shown that the MC carbide within LPBF-built IN738LC is mainly made of titanium, which has the same atomic concentration as its carbon content.[13,28] Thus, when more carbides are formed through acquiring the titanium solutes within the supersaturated gamma matrix, the availability of titanium for γ' formation is sharply decreased. This lack of sufficient γ' is expected to diminish the high-temperature performance of IN738LC with an additional 0.3 wt.% carbon. Yet, for room-temperature applications, the presence of more carbides contributes to a higher hardness, as shown in Figure 7A. The similar microstructures after the two-step HT in Figure 3A_3 and B_3 yielded similar hardness results around 490 HV. With the increase in carbide density, the hardness property of the IN738LC added with 0.3 wt.% carbon reaches about 520 HV, yielding a 30 HV increment.

The higher solution and aging HT temperatures in the three-step HT process promote the growth of primary γ', but reduce the size of those secondary γ' (Figures 3 and 4). Prior literature suggests that the presence of fine γ' (< 100 µm) is beneficial toward both the room temperature and high-temperature (up to 850°C) strengths of IN738LC,[25] which is also the rationale for the design of the existing three-step HT. Yet, our preliminary hardness results show the opposite trend (Figure 7A). In general, the samples after the three-step HT are about 50 HV to 80 HV, softer than their counterparts experiencing the two-step HT, despite that the three-step HT produced much finer secondary γ' precipitates. There are two potential explanations for the observed phenomenon. First, during the growth of

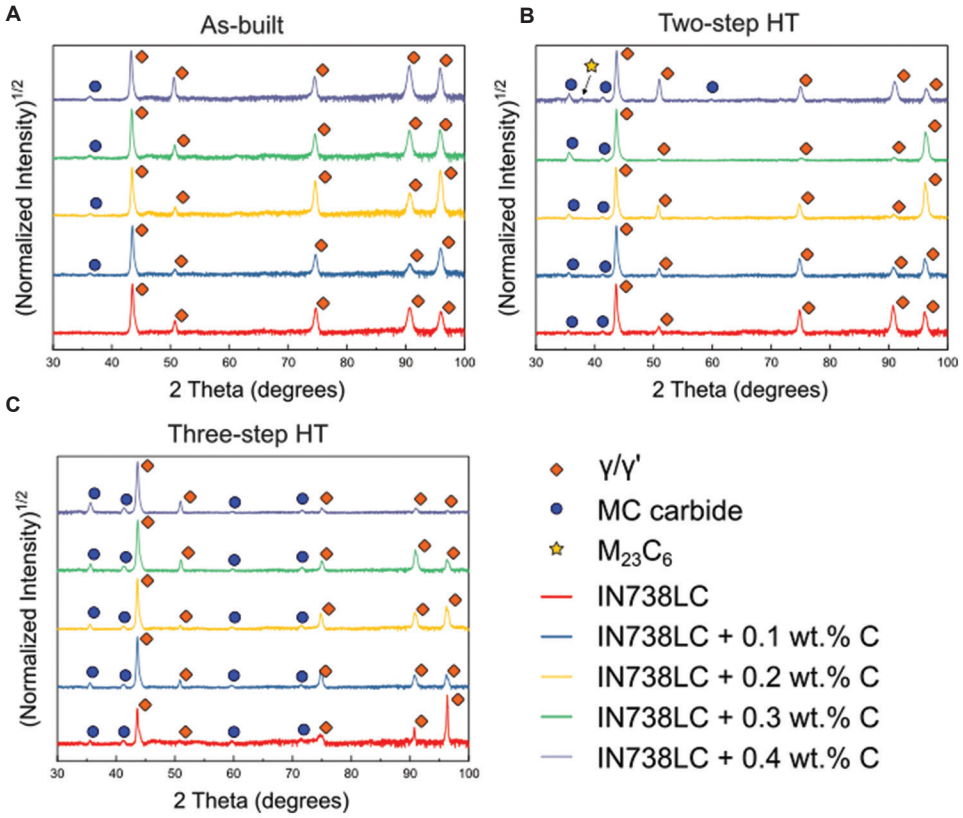

Figure 5. X-ray crystallography results of the IN738LC samples mixed with different amounts of carbon (from 0 to 0.4 wt.%) fabricated with a 130 W laser power input in the (A) as-built, (B) two-step heat treatment (HT), and (C) three-step HT conditions. The orange rectangle indicates the γ/γ' phase, while the blue circle and yellow represent the MC and $M_{23}C_6$ carbides.

those exceptionally large primary γ' under the three-step HT, they absorbed all available adjacent solutes, as shown in the empty white space in Figure $4A_3$. These areas are unable to resist the propagation of slip dislocations during plastic deformation, hence weakening the material.[38] Second, the carbides under the three-step HT have become much larger in size and are primarily confined within the high-angle grain boundaries (Figure $4B_1$ and C_1), possibly due to the lowering of grain boundary energies through solute segregation during HT.[39] The lack of fine intragranular carbides will then reduce the material's hardness. The hardness results from Figure 7A corroborate this hypothesis, as all three samples under the three-step HT have similar hardness results, and the difference in their carbon content (thus carbides) did not make any discernible difference in the hardness property.

While the influence of carbon content on the γ' characteristics might not be too obvious, at least for the 0.1 wt.% sample, its effect on recrystallization was much more pronounced. All as-built specimens have a similar as-built grain morphology comprising columnar grains (Figure 6). The standard two-step HT yielded little change for the pure IN738LC and IN738LC with 0.1 wt.% carbon additions but an obvious grain growth for the 0.3 wt.% carbon-added sample. Prior literature suggests that the carbide within nickel-base superalloys serves dual purposes during recrystallization.[33] On the one hand, carbides act as nucleation sites for recrystallized grains, termed as particle-stimulated nucleation; on the other hand, they inhibit recrystallized grain boundary migration through the Zener pinning effect.[40] It is postulated that when the carbide density increases, the grain nucleation during recrystallization is initially promoted (Figure $6C_1$), but as the carbides along the high-angle grain boundaries reach a critical size (measured to be 1.8 ± 0.6 μm from Figure $4C_1$), the grain can no longer grow further (Figure $6C_3$).

The same phenomenon was also observed for the 0.1 wt.% carbon-added sample under the three-step HT procedure (Figure $6B_3$). The only specimen that can transform from a columnar-shaped grain into an equiaxed grain is the pure IN738LC under the three-step HT (Figure $6A_3$). These results highlight the sensitivity of carbon content within the IN738LC alloy during the recrystallization process. Even with only 0.1 wt.% carbon addition, grain growth is severely limited.

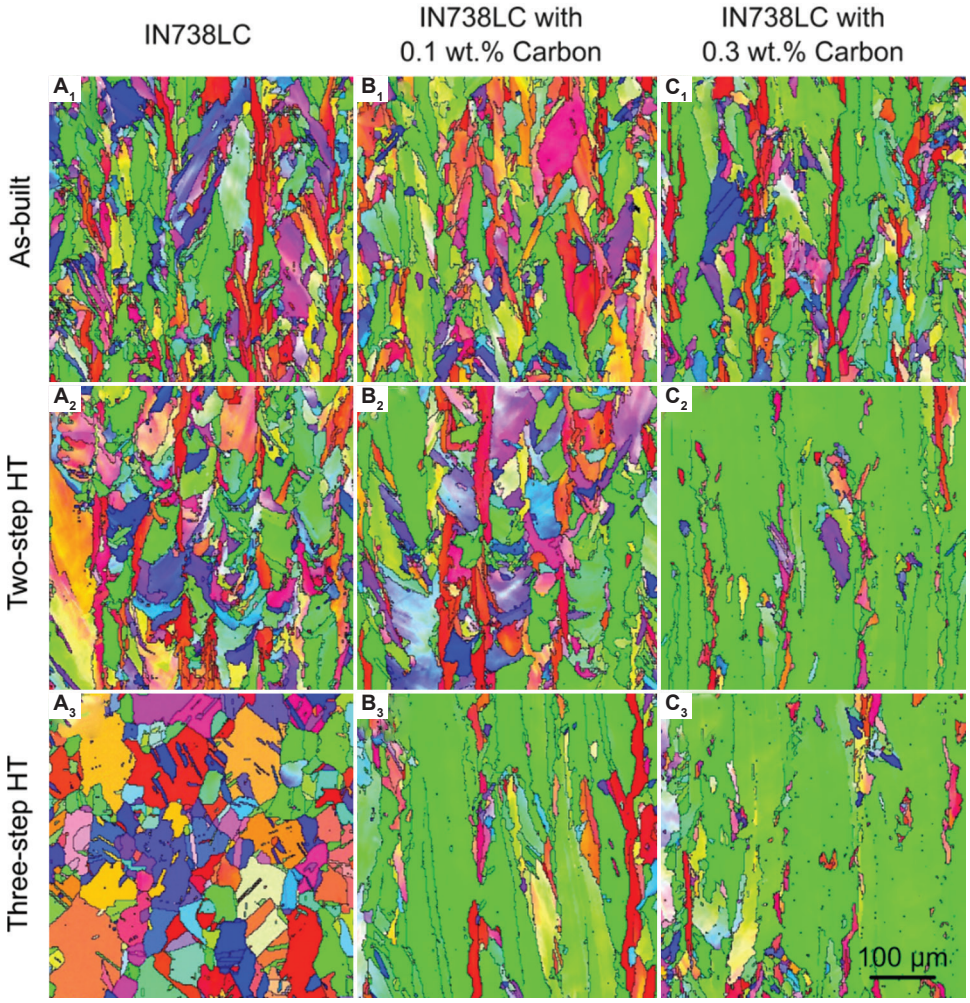

Figure 6. Inverse pole figure (IPF) maps of specimens under the as-built, two-step heat treatment (HT), and three-step HT conditions for (A_1–A_3) pure IN738LC, (B_1–B_3) In738LC mixed with 0.1 wt.% carbon, and (C_1–C_3) IN738LC mixed with 0.3 wt.% of carbon. The IPFs are constructed with a viewing direction parallel to the build direction.

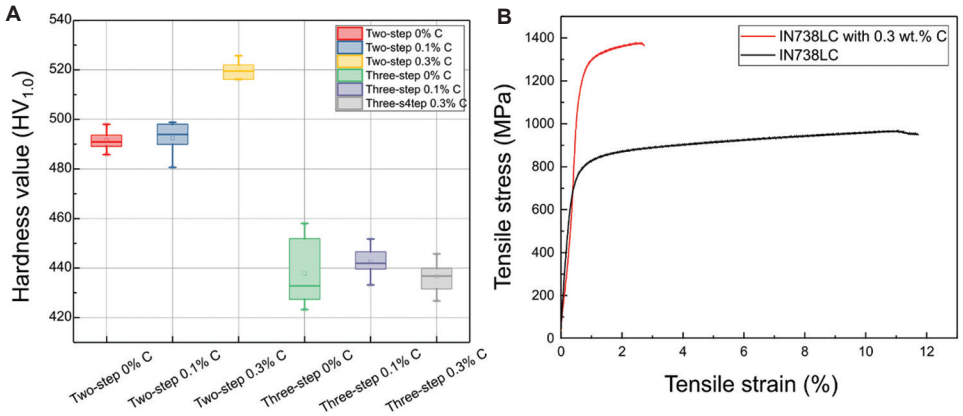

Figure 7. (A) Microhardness results of the three specimens under investigation after the two different heat treatment processes. (B) The room-temperature tensile results of the as-built IN738LC and the as-built IN738LC with 0.3 wt.% carbon addition. It should be noted that the tensile property of the 0.3 wt.% carbon-added sample was retrieved from its non-cracked regions. Care must be taken when interpreting its mechanical performance for the entire built part.

The room temperature tensile results of the as-built pure IN738LC and IN738LC with an addition of 0.3 wt.% are presented in Figure 7B. These results are comparable to those reported in the literature, with and without carbon additions.[3,18] However, one major issue found in the present study, which is not reported in prior works, is the presence of large, horizontal cracks within the as-built IN738LC with an addition of 0.3 wt.% carbon (Figure 8A and B). Its tensile property is only measured in those non-cracked regions. It should be noted, though, that the present work used powder mixtures between the IN738LC and graphite powders instead of pre-alloyed powders. Despite this fact, the presence of large delamination cracks still warrants further investigation.

Most of the delamination cracks in the existing literature are centered on those carbide-containing tool steels, whereas the occurrence of cracking is a measure to relieve the inherent residual stresses accumulated during the LPBF production.[41] We believe that it is a similar mechanism for the crack occurrence in the current material. A small-sized, representative fracture surface of the crack under OM is shown in Figure 8C. Within this specimen, the top portion is the cracked surface, showing a bright contrast. The lower portion is the region, which was originally still intact after production but was broken apart to examine the fracture surface. Laser melt tracks were observed on the cracked surface during LPBF fabrication (Figure 8D). Such a feature indicates that fusion between successive layers did not take place during the production run, likely due to part distortions triggered by the build-up of residual stresses. As for regions that were originally intact after LPBF fabrication, ductile dimples were detected (enlarged view within Figure 8E), suggesting the ductile failure mode during the breaking of parts after the LPBF production.

Despite the few reports on such delamination cracks in the open literature, these cracks pose a significant challenge to the LPBF production of precipitation-containing alloys, which often offer superb strength, wear, and conductivity properties.[42] During the production of samples with small dimensions (with a cross-sectional area of 10 × 10 mm^2, Figure 1), no cracks were observed. The delamination cracks only occurred for large samples, whose residual stress content is believed to be much larger.[43] Hence, the key to fabricating crack-free samples having large precipitation content is to minimize the amount of residual stress that occurs during production. One proven method is to use a heated substrate to reduce the thermal gradient during fabrication and, hence, lower the residual stress content.[44]

5. Conclusion

The present study aims to examine the effect of increasing the carbon content within precipitation-strengthened nickel-base superalloy IN738LC during the LPBF process. Besides its benefit of reducing the material's hot cracking susceptibility, three potential problems associated with

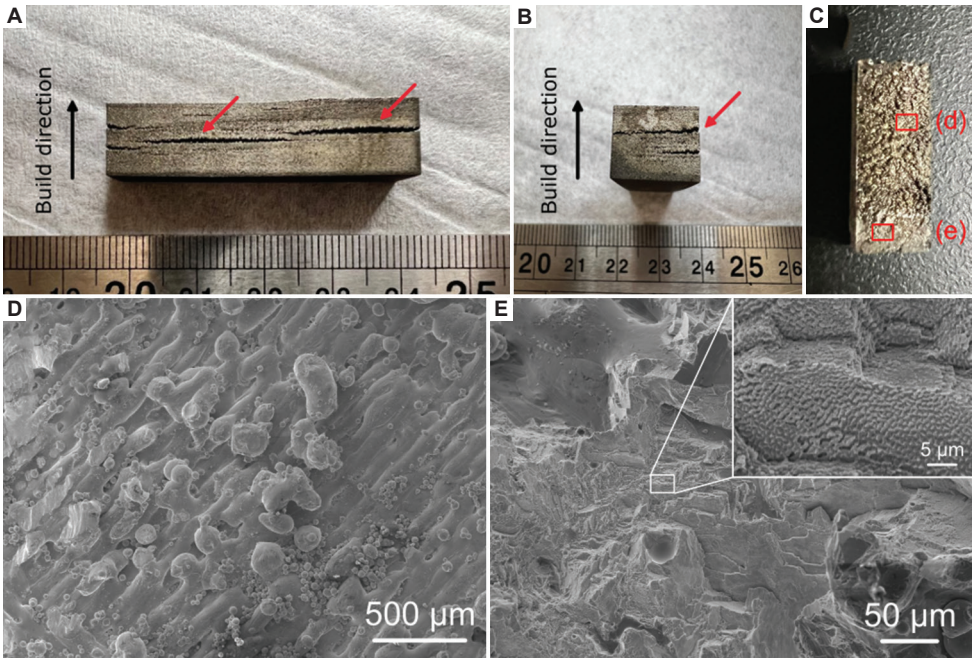

Figure 8. Large, horizontal cracks present in the as-built IN738LC with an addition of 0.3 wt.% carbon from (A) longitudinal and (B) cross-sectional views. (C) The fracture surface of the horizontal crack under optical microscopy. Enlarged scanning electron microscopy images of the crack surface focusing on the (D) delaminated and (E) still intact regions.

this approach are investigated in detail, namely, the size and distribution of γ', the ease of recrystallization, and the presence of large delamination cracks.

(i). The effect of carbon addition on the γ' precipitation is limited when the addition amount is about 0.1 wt.%. Under the conventional two-step HT, the γ' has a typical bimodal distribution, with the primary γ' being around 200 to 400 nm and the secondary γ' about 100 nm. However, with the addition of 0.3 wt.% carbon, the γ' precipitation is severely restricted. Instead, MC carbide becomes the dominant precipitate, which increases the material's room-temperature hardness and strength.

(ii). The carbon content is found to be very sensitive toward grain recrystallization. Even with an addition of 0.1 wt.% carbon, the recrystallization is limited to large columnar grains. Only the original IN738LC composition could be fully recrystallized and form equiaxed grains with annealing twins. With additional carbon, they could facilitate early grain nucleation during recrystallization. However, large carbides with a size of about 1.8 μm will eventually form and pin the high-angle grain boundaries and restrict their migration.

(iii). Horizontal delamination cracks occurred during the production of large specimens with the dimension of 45 × 10 × 10 mm^3. No crack was observed for smaller samples (cross-sectional area of 10 × 10 mm^2) fabricated using the same LPBF production parameters. Such cracks are frequently observed for alloys containing a high density of hard precipitates, and their formation is often attributed to the inherent high residual stresses.

Acknowledgments

None.

Funding

Z. Sun acknowledges financial support from the Career Development Fund (grant reference no.: C222812017), Young Individual Research Grant (Grant reference no.: M22K3c0096); and P. Wang acknowledges the financial support from the Individual Research Grant (grant reference no.: A20E7c0109) from the Agency for Science, Technology and Research of Singapore.

Conflict of interest

No potential competing interests.

Author contributions

Conceptualization: Zhongji Sun

Formal analysis: Verner Soh

Investigation: Coryl Lee

Methodology: Delvin Wuu, Desmond Lau

Visualization: Siyuan Wei, Chee Koon Ng

Writing – original draft: Zhongji Sun

Writing – review & editing: Zhongji Sun, Swee Leong Sing, Dennis Tan, Pei Wang

Ethics approval and consent to participate

Not applicable.

Consent for publication

Not applicable.

Availability of data

Data are available from the corresponding author on reasonable request.

References

1. Guo C, Yu Z, Hu X, *et al*. Y2O3 nanoparticles decorated IN738LC superalloy manufactured by laser powder bed fusion: Cracking inhibition, microstructures and mechanical properties. *Compos Part B Eng*. 2022;230:109555.

   doi: 10.1016/j.compositesb.2021.109555

2. Xu J, Ding Y, Gao Y, *et al*. Improving high-temperature mechanical properties of laser powder bed-fused Inconel 738 alloy by hot isostatic pressing: Tailoring precipitates and healing defects. *Mater Sci Eng A*. 2023;862:144285.

   doi: 10.1016/j.msea.2022.144285

3. Zhang L, Li Y, Zhang Q, Zhang S. Microstructure evolution, phase transformation and mechanical properties of IN738 superalloy fabricated by selective laser melting under different heat treatments. *Mater Sci Eng A*. 2022;844:142947.

   doi: 10.1016/j.msea.2022.142947

4. Sotov AV, Agapovichev AV, Smelov VG, *et al*. Investigation of the IN-738 superalloy microstructure and mechanical properties for the manufacturing of gas turbine engine nozzle guide vane by selective laser melting. *Int J Adv Manuf Technol*. 2020;107(5-6):2525-2535.

   doi: 10.1007/s00170-020-05197-x

5. Rickenbacher L, Etter T, Hövel S, Wegener K. High temperature material properties of IN738LC processed by selective laser melting (SLM) technology. *Rapid Prototyp J*. 2013;19(4):282-290.

   doi: 10.1108/13552541311323281

6. Vilanova M, Garciandia F, Sainz S, Jorge-Badiola D, Guraya T, San Sebastian M. The limit of hot isostatic pressing for healing cracks present in an additively manufactured nickel superalloy. *J Mater Process Technol*. 2022;300:117398.

   doi: 10.1016/j.jmatprotec.2021.117398

7. Mostafaei A, Ghiaasiaan R, Ho IT, *et al*. Additive Manufacturing of Nickel-based superalloys: A state-of-the-art review on process-structure-defect-property relationship. *Prog Mater Sci*. 2023;136:101108.

   doi: 10.1016/j.pmatsci.2023.101108

8. Han C, Fang Q, Shi Y, Tor SB, Chua CK, Zhou K. Recent advances on high-entropy alloys for 3D printing. *Adv Mater*. 2020;32(26):e1903855.

   doi: 10.1002/adma.201903855

9. Zhao D, Liang H, Han C, *et al*. 3D printing of a titanium-tantalum Gyroid scaffold with superb elastic admissible strain, bioactivity and in-situ bone regeneration capability. *Addit Manuf*. 2021;47:102223.

   doi: 10.1016/j.addma.2021.102223

10. DebRoy T, Wei HL, Zuback JS, *et al*. Additive manufacturing of metallic components - process, structure and properties. *Prog Mater Sci*. 2018;92:112-224.

    doi: 10.1016/j.pmatsci.2017.10.001

11. Xu J, Lin X, Guo P, *et al*. The initiation and propagation mechanism of the overlapping zone cracking during laser solid forming of IN-738LC superalloy. *J Alloys Compd*. 2018;749:859-870.

    doi: 10.1016/j.jallcom.2018.03.366

12. Zhang X, Chen H, Xu L, Xu J, Ren X, Chen X. Cracking mechanism and susceptibility of laser melting deposited Inconel 738 superalloy. *Mater Des*. 2019;183:108105.

    doi: 10.1016/j.matdes.2019.108105

13. Sun Z, Ma Y, Ponge D, *et al*. Thermodynamics-guided alloy and process design for additive manufacturing. *Nat Commun*. 2022;13(1):4361.

    doi: 10.1038/s41467-022-31969-y

14. Chen QZ, Jones N, Knowles DM. The microstructures of base/modified RR2072 SX superalloys and their effects on creep properties at elevated temperatures. *Acta Mater*. 2002;50(5):1095-1112.

    doi: 10.1016/S1359-6454(01)00410-4

15. Wei CN, Bor HY, Chang L. The effects of carbon content on the microstructure and elevated temperature tensile strength of a nickel-base superalloy. *Mater Sci Eng A*. 2010;527(16-17):3741-3747.

    doi: 10.1016/j.msea.2010.03.053

16. Wei CN, Bor HY, Chang L. The influence of carbon addition on carbide characteristics and mechanical properties of CM-681LC superalloy using fine-grain process. *J Alloys Compd*. 2011;509(18):5708-5714.

    doi: 10.1016/j.jallcom.2011.02.146

17. Li XW, Liu T, Wang L, Liu XG, Lou LH, Zhang J. Effect of carbon content on the microstructure and creep properties of a 3rd generation single crystal nickel-base superalloy. *Mater Sci Eng A*. 2015;639:732-738.

    doi: 10.1016/j.msea.2015.05.039

18. Zhou W, Tian Y, Tan Q, *et al*. Effect of carbon content on the microstructure, tensile properties and cracking susceptibility of IN738 superalloy processed by laser powder bed fusion. *Addit Manuf*. 2022;58:103016.

    doi: 10.1016/j.addma.2022.103016

19. Kontis P, Collins DM, Wilkinson AJ, Reed RC, Raabe D, Gault B. Microstructural degradation of polycrystalline superalloys from oxidized carbides and implications on crack initiation. *Scr Mater*. 2018;147:59-63.

    doi: 10.1016/j.scriptamat.2017.12.028

20. Yao J, Cahoon JR. Discussion of "hydrogen induced grain boundary fracture in high purity nickel and its alloys-enhanced hydrogen diffusion along grain boundaries. *Scr Metall*. 1988;22(11):1817-1820.

    doi: 10.1016/S0036-9748(88)80291-6

21. Kontis P, Kostka A, Raabe D, Gault B. Influence of composition and precipitation evolution on damage at grain boundaries in a crept polycrystalline Ni-based superalloy. *Acta Mater*. 2019;166:158-167.

    doi: 10.1016/j.actamat.2018.12.039

22. Furrer DU. Application of phase-field modeling to industrial materials and manufacturing processes. *Curr Opin Solid State Mater Sci*. 2011;15(3):134-140.

    doi: 10.1016/j.cossms.2011.03.001

23. Chen J, Xue L. Process-induced microstructural characteristics of laser consolidated IN-738 superalloy. *Mater Sci Eng A*. 2010;527(27-28):7318-7328.

    doi: 10.1016/j.msea.2010.08.003

24. Messé OMDM, Muñoz-Moreno R, Illston T, Baker S, Stone HJ. Metastable carbides and their impact on recrystallisation in IN738LC processed by selective laser melting. *Addit Manuf*. 2018;22:394-404.

    doi: 10.1016/j.addma.2018.05.030

25. Balikci E, Mirshams RA, Raman A. Tensile strengthening in the nickel-base superalloy IN738LC. *J Mater Eng Perform*. 2000;9(3):324-329.

    doi: 10.1361/105994900770345999

26. Balikci E, Raman A, Mirshams RA. Influence of various heat treatments on the microstructure of polycrystalline IN738LC. *Metall Mater Trans A Phys Metall Mater Sci*. 1997;28(10):1993-2003.

    doi: 10.1007/s11661-997-0156-9

27. Bettge D, Oesterle W, Ziebs J. Temperature dependence of yield strength and elongation of the nickel-base superalloy IN 738 LC and the corresponding microstructural evolution.

Zeitschrift fuer Met Res Adv Tech. 1995;86(3):190-197.

doi: 10.1515/ijmr-1995-860309

28. Hariharan A, Lu L, Risse J, *et al*. Misorientation-dependent solute enrichment at interfaces and its contribution to defect formation mechanisms during laser additive manufacturing of superalloys. *Phys Rev Mater*. 2019;3(12):123602.

doi: 10.1103/PhysRevMaterials.3.123602

29. Godec M, Zaefferer S, Podgornik B, Šinko M, Tchernychova E. Quantitative multiscale correlative microstructure analysis of additive manufacturing of stainless steel 316L processed by selective laser melting. *Mater Charact*. 2020;160:110074.

doi: 10.1016/j.matchar.2019.110074

30. Starink MJ, Cama H, Thomson RC. MC carbides in the Hf containing Ni based superalloy MarM002. *Scr Mater*. 1997;38(1):73-80.

doi: 10.1016/S1359-6462(97)00409-0

31. Kang SG, Gainov R, Heußen D, *et al*. Green laser powder bed fusion based fabrication and rate-dependent mechanical properties of copper lattices. *Mater Des*. 2023;231:112023.

doi: 10.1016/j.matdes.2023.112023

32. Sun Z, Tsai SP, Konijnenberg P, Wang JY, Zaefferer S. A large-volume 3D EBSD study on additively manufactured 316L stainless steel. *Scr Mater*. 2024;238:115723.

doi: 10.1016/j.scriptamat.2023.115723

33. Wang L, Xie G, Zhang J, Lou LH. On the role of carbides during the recrystallization of a directionally solidified nickel-base superalloy. *Scr Mater*. 2006;55(5):457-460.

doi: 10.1016/j.scriptamat.2006.05.013

34. Zhou Y, Volek A. Effect of carbon additions on hot tearing of a second generation nickel-base superalloy. *Mater Sci Eng A*. 2008;479(1-2):324-332.

doi: 10.1016/j.msea.2007.06.076

35. Tin S, Pollock TM. Stabilization of thermosolutal convective instabilities in Ni-based single-crystal superalloys: Carbide precipitation and Rayleigh numbers. *Metall Mater Trans A Phys Metall Mater Sci*. 2003;34A(9):1953-1967.

doi: 10.1007/s11661-003-0160-7

36. Sun Z, Tan X, Tor SB. Effects of Chamber Oxygen Concentration on Microstructure and Mechanical Properties of Stainless Steel 316L Parts by Selective Laser Melting. In: Proceedings of the International Conference on Progress in Additive Manufacturing; 2018. p. 470-5.

doi: 10.25341/D4CS38

37. Zhang L, Li Y, Zhang S, Zhang Q. Selective laser melting of IN738 superalloy with a low Mn+Si content: Effect of energy input on characteristics of molten pool, metallurgical defects, microstructures and mechanical properties. *Mater Sci Eng A*. 2021;826:141985.

doi: 10.1016/j.msea.2021.141985

38. Xu J, Gruber H, Boyd R, Jiang S, Peng RL, Moverare JJ. On the strengthening and embrittlement mechanisms of an additively manufactured Nickel-base superalloy. *Materialia*. 2020;10:100657.

doi: 10.1016/j.mtla.2020.100657

39. Liu F, Kirchheim R. Nano-scale grain growth inhibited by reducing grain boundary energy through solute segregation. *J Cryst Growth*. 2004;264(1-3):385-391.

doi: 10.1016/j.jcrysgro.2003.12.021

40. Collins DM, Conduit BD, Stone HJ, Hardy MC, Conduit GJ, Mitchell RJ. Grain growth behaviour during near-γ' solvus thermal exposures in a polycrystalline nickel-base superalloy. *Acta Mater*. 2013;61(9):3378-3391.

doi: 10.1016/j.actamat.2013.02.028

41. Platl J, Bodner S, Hofer C, *et al*. Cracking mechanism in a laser powder bed fused cold-work tool steel: The role of residual stresses, microstructure and local elemental concentrations. *Acta Mater*. 2022;225:117570.

doi: 10.1016/j.actamat.2021.117570

42. Yang K, Wang Y, Guo M, *et al*. Recent development of advanced precipitation-strengthened Cu alloys with high strength and conductivity: A review. *Prog Mater Sci*. 2023;138:101141.

doi: 10.1016/j.pmatsci.2023.101141

43. Xie D, Lv F, Yang Y, *et al*. A Review on distortion and residual stress in additive manufacturing. *Chin J Mech Eng Addit Manuf Front*. 2022;1(3):100039.

doi: 10.1016/j.cjmeam.2022.100039

44. Risse J. Additive Manufacturing of Nickel-Base Superalloy IN738LC by Laser Powder Bed Fusion. Germany: Lehrstuhl für Lasertechnik; 2019.

doi: 10.18154/RWTH-2019-06822

ACCSCIENCE PUBLISHING

Materials Science in Additive Manufacturing

ORIGINAL RESEARCH ARTICLE

Enhancing interlaminar adhesion in multi-material 3D printing: A study of conductive PLA and TPU interfaces through fused filament fabrication

Guo Liang Goh[1,2], Samuel Lee[1], Shi Hui Cheng[1], Daniel Jee Seng Goh[1], Pothunuri Laya[2], Van Pho Nguyen[1,3], Boon Siew Han[3], and Wai Yee Yeong[1,2]*

[1]School of Mechanical and Aerospace Engineering, Nanyang Technological University, Singapore

[2]Singapore Centre for 3D Printing, School of Mechanical and Aerospace Engineering, Nanyang Technological University, Singapore

[3]Schaeffler Hub for Advanced Research, Nanyang Technological University, Singapore

Abstract

In the rapidly expanding field of additive manufacturing, multi-material fused filament fabrication represents a frontier with vast potential for creating composite structures that blend the benefits of different material properties. Interlaminar adhesion between dissimilar materials remains a challenge for the realization of multifunctional structure for practical use. This study investigates the interlaminar adhesion between conductive polylactic acid and thermoplastic polyurethane, materials representative of rigid and flexible characteristics, respectively. We present a comparative analysis of two adhesion enhancement approaches: the incorporation of mechanical interlocking features and the modification of surface roughness at the interface. Through tensile testing, we evaluate the effectiveness of these methods against a benchmark coupon with unmodified interface. Micro-computed tomography analysis, surface morphology analysis, and mechanical performance assessments elucidate the failure modes and provide insights into the interfacial behavior of these interface designs. We found that the interface design with top infill modification showed the highest interlaminar adhesion strength, with an improvement of at least 25% compared to the benchmark coupon. Our findings aim to inform the design and manufacturing practices in multi-material 3D printing and to open new avenues for the development of multifunctional, composite 3D-printed systems.

Keywords: 3D printing; Additive manufacturing; Multi-material; Polymer; Composite material; Adhesion; Interface

***Corresponding author:**
Wai Yee Yeong
(wyyeong@ntu.edu.sg)

Citation: Goh GL, Lee S, Cheng SH, *et al*. Enhancing interlaminar adhesion in multi-material 3D printing: A study of conductive PLA and TPU interfaces through fused filament fabrication. *Mater Sci Add Manuf.* 2024;3(1):2672.
doi: 10.36922/msam.2672

Received: January 8, 2024

Accepted: February 2, 2024

Published Online: February 27, 2024

1. Introduction

The advent of additive manufacturing, also known as 3D printing, has transformed the landscape of material science and engineering, propelling the innovation of new applications across a diverse range of industries such as printed electronics,

tissue engineering, and aerospace and defense.[1-5] Fused filament fabrication (FFF) stands out among the array of multi-material 3D printing technologies (Figure 1A) for its versatility, accessibility, and efficiency in creating complex geometries[6-8] and the availability of a wide range of materials, such as polylactic acid (PLA), thermoplastic polyurethane (TPU), acrylonitrile butadiene styrene (ABS), polyethylene terephthalate glycol, nylon, and polyether ether ketone (PEEK). To date, various material combinations have been attempted, such as PLA/ABS, PLA/TPU, conductive polylactic acid (cPLA)/ABS, PLA/TPU, chlorinated polyethylene (CPE)/TPU, CPE/PLA, PLA/conductive-PLA, ABS/conductive-PLA, and ABS/TPU, just to name a few.[7,9-14] One of the promising areas of interest within multi-material FFF is the printing of soft and rigid materials, which promises to revolutionize the manufacturing of multifunctional applications, from structural electronics to soft robotic devices.[15-18] Among the materials of interest, cPLA and TPU have garnered significant attention due to their unique properties – cPLA for its rigidity and ability to conduct electricity, and TPU for its elasticity and durability.[19]

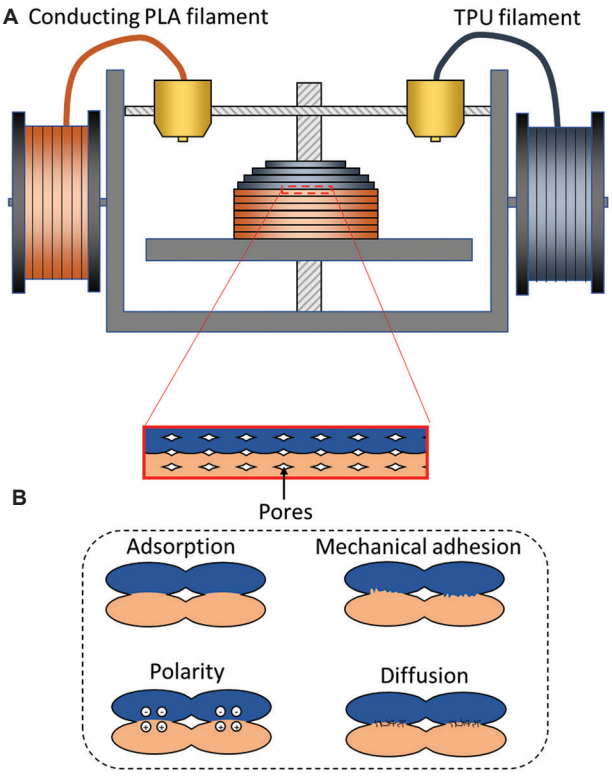

Figure 1. Schematics illustrating (A) the fabrication of a multi-material part through a multi-nozzle fused filament fabrication process and (B) the possible adhesion mechanisms at the interface of a fused filament fabricated multi-material part. Adapted from Watschke *et al.*[36] (licensed under CC BY 4.0). Abbreviations: cPLA: conductive polylactic acid; TPU: Thermoplastic polyurethane.

The fusion of these materials within a single print could lead to the creation of objects with both structural support and flexible characteristics, offering myriad possibilities such as actuators and electronic components integrated into structural frameworks.[20] This capacity for *in situ* fabrication of structures combining multiple material allows for more integrated system with fewer parts and reduces the need for manual assembly. In recent research, Goh *et al.* explored the multifaceted capabilities of multi-material 3D printing by synergizing the distinct properties of cPLA and TPU.[19] Their innovative approach led to the fabrication of a multifunctional robotic gripper, which integrates the rigid features of cPLA as a variable-stiffness backbone, along with the inherent softness of TPU to impart a gentle gripping action. This integration exemplifies the potential of combining soft and rigid materials to create adaptive, responsive structures that leverage the best attributes of each constituent material for advanced robotic applications.[21] However, a critical challenge that impedes the broad implementation of this technology is the issue of interlaminar adhesion between distinct material types. Typically, the adhesion mechanisms between dissimilar polymeric materials are adsorption, mechanical interlocking, polarity, diffusion, *etc.*, as illustrated in Figure 1B.[22] Effective adhesion between cPLA and TPU is pivotal to ensure mechanical integrity and functional performance. Nevertheless, the disparity in the thermal, mechanical, and chemical properties between PLA and TPU creates a complex interface that is prone to delamination and structural weakness under stress.[18] Moreover, the different melting temperatures and rates of thermal contraction during the cooling phase further complicate the bonding process, resulting in a lackluster interfacial adhesion.

Existing approaches to mitigate these adhesion issues are as diverse as the applications they serve. Strategies range from plasma surface treatments to increase the surface energy of the materials, to physical methods such as the inclusion of mechanical interlocks or using a gradient transition between dissimilar materials.[7,10,11,14,23-26] From a mechanical perspective, enhanced adhesion between 3D-printed filaments can be achieved by increasing the contact surface area at the interface. This can be accomplished through the implementation of a skewed toolpath configuration and by elevating the material extrusion rate, both of which serve to augment the interfacial bonding area between the filaments.[27,28] From a materials science perspective, researchers have experimented with the introduction of chemicals or

adhesion promoters that can bond to both PLA and TPU.[29] Process-based modifications, such as optimizing print temperature, speed, and layer height, have also shown potential in improving adhesion.[30,31] Moreover, the integration of nanomaterials and the development of hybrid filaments are emerging as promising frontiers in addressing these adhesion challenges. Each approach carries its own set of advantages and trade-offs, necessitating a comprehensive study to identify the most effective method for a given application. However, these works mainly focused on the interaction between the pure polymeric materials. Nevertheless, the existing literature primarily emphasizes the interplay between unmodified polymeric materials.[32,33] There remains a substantial research gap in understanding the interlaminar properties when one introduces nanocomposites into the mix, particularly between cPLA enhanced with nanoparticles and unaltered TPU. Furthermore, the mechanical interlocks approach often requires a large overlap/transition region to achieve satisfactory interlaminar strength which may not be suitable for some applications. These areas of study are crucial for advancing the application potential of multi-material 3D printing, as it addresses the interface between technologically augmented and standard polymers.

Recognizing the need for enhanced interfacial adhesion, this study delves into two specific enhancement approaches: the engineering of low-profile mechanical interlocking features (<2 mm in thickness) and the tailoring of surface roughness at the interface. These approaches are assessed against a benchmark part with no modifications, providing a comprehensive comparative analysis. By exploring these strategies, this research aims to unravel the complexities of the cPLA-TPU interface and to contribute to the optimization of multi-material FFF processes. The outcomes will provide crucial insights into maximizing the interfacial adhesion, thus enabling the reliable creation of composite materials with integrated soft and rigid characteristics for advanced manufacturing applications.

2. Methods

2.1. Materials

In this study, we utilized cPLA and TPU filaments, with a standard diameter of 1.75 mm, to investigate the adhesion properties relevant for multi-material FFF. The selected cPLA filament, sourced from Protopasta®, is a composite material enhanced with carbon black nanofillers to infuse the PLA with electrical conductivity, while maintaining its inherent rigidity. The soft material chosen is a NinjaFlex TPU filament, acquired from Ninjatek®, notable for its flexibility and a Shore hardness rating of 85A, which falls into the medium-hard category for thermoplastic elastomers. Comprehensive details regarding the specifications, material properties, and manufacturer data for both the cPLA and TPU filaments are systematically cataloged in Table 1. The table provides an overview of key parameters, such as tensile strength, elongation at break, thermal properties, and electrical conductivity, offering a foundation for the ensuing analysis of interlaminar adhesion. This selection of materials facilitates a focused assessment of the interfacial adhesion challenges between a conductive, rigid filament and a non-conductive, flexible counterpart, contributing to the broader understanding of multi-material 3D printing dynamics.

2.2. Design and fabrication of test coupons

The test coupons were designed using a 3D design CAD software, Solidworks® 2022. In this work, a multi-material

Table 1. Summary of materials used in this work for the fabrication of test coupons

Material type	Brand	Model	Property
cPLA	Protopasta®	Electrically conductive composite PLA	• Appearance: black • Additives: carbon black • Volume resistivity of molded resin: 15 Ω-cm • Volume resistivity of 3D-printed parts along layers (x/y): 30 Ω-cm • Volume resistivity of 3D-printed parts against layers (z): 115 Ω-cm • Melt temperature: 155°C • Density: 1.24 g/cm^3 • Tensile modulus: 3.6 MPa • Tensile yield strength: 60 MPa
TPU	Ninjatek®	NinjaFlex	• Appearance: glossy black • Shore hardness: 85A • Maximum elongation: 660% • Melt temperature: 216°C • Density: 1.19 g/cm^3 • Tensile modulus: 12 MPa • Yield strength: 4 MPa

Abbreviations: cPLA: conductive polylactic acid; PLA: Polylactic acid; TPU: Thermoplastic polyurethane.

tensile coupon was designed and used to facilitate the evaluation of interlaminar adhesion property between cPLA and TPU materials. The design of the tensile coupons was adopted from ASTM D638. In this work, we focused on adhesion property between cPLA and TPU materials in the build direction (z-direction). The design and the part orientation used for printing of the tensile coupons are illustrated in Figure 2.

In this study, we conducted a detailed examination of interlaminar adhesion by fabricating and assessing three distinct types of test coupons, differentiated by their interface treatments:

(i) Unmodified interface coupons: These samples were produced without any intentional alterations to the interface. The printing parameters were set to allow for filament deposition with no gaps, ensuring that the layers were laid down in direct contact with one another. This standard configuration serves as the control group, providing a baseline for evaluating the efficacy of interfacial modifications.

(ii) Low-profile mechanical interlocking feature coupons: For these specimens, we introduced a mechanical interlocking design, which features two layers of interlocking geometry that extends 2 mm into the material. The precise pattern of this feature is illustrated in Figure 2C. The intention behind this design is to enhance the mechanical bond between layers through increased physical engagement, akin to the interlocking teeth of a zipper. The design of the interlocking feature was generated using Ultimaker Cura® 5.3.1.

(iii) Top infill modification: The final group of samples includes a modification to the top layer of the bottom part, designed to augment the effective bonding surface area. This was achieved by programming a fine 1 mm gap (or groove) on the top layer of the lower filament segment before depositing the subsequent material. When printing this variant, the printer's nozzle was deliberately positioned closer to the print bed. This adjustment ensures that the extruded filament is compelled into the grooves, forming a mechanical bond on solidification.

This approach to sample design allowed for the comparative analysis of interlaminar adhesion under varying interface conditions. By testing each configuration, we seek to provide insight on the impact of various interface designs and the print order of the materials on the overall bond strength between the rigid cPLA and the flexible TPU layers in multi-material prints.

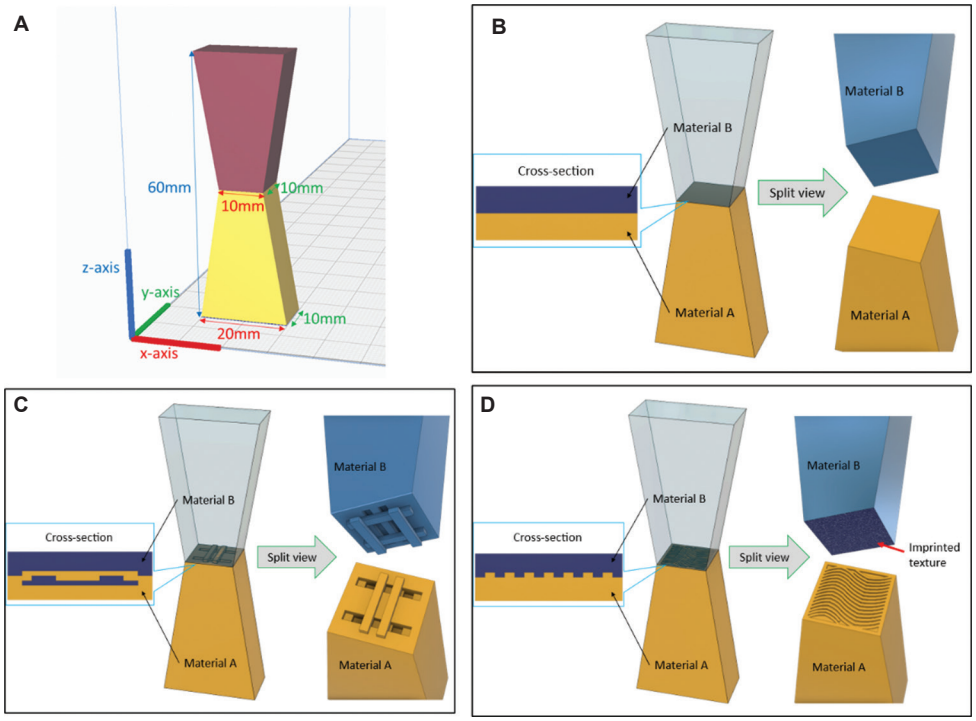

Figure 2. Schematic showing the (A) dimensions and print orientation of the tensile coupon for the investigation of interlaminar adhesion property between cPLA and TPU. (B-D) show the designs of the interfacial feature of multi-material tensile coupon, with (B) showing the normal interface, (C) mechanical interlocking feature, and (D) top infill modification coupons. Abbreviations: cPLA: conductive polylactic acid; TPU: Thermoplastic polyurethane.

Another critical component of the methodology involved the investigation of material deposition order and its effect on interlaminar adhesion properties. We systematically prepared and tested samples using two distinct printing sequences, specifically varying the order in which cPLA and TPU were printed. This variation aimed to ascertain the influence of print order on the bond quality between cPLA and TPU. In Figure 2, "Material A" and "Material B" refer to cPLA and TPU, respectively, whose printing order was alternated as detailed in the subsequent paragraph and summarized in Table 2.

The first set of samples was fabricated by initiating the print with the cPLA, subsequently followed by the deposition of the TPU layer. This sequence prioritizes the placement of the rigid material as the foundational layer. Conversely, the second set of samples reversed this order, starting with TPU as the base, on which cPLA was printed. The test coupons were fabricated through a modified E3D ToolChanger on a standard glass heated bed. A 0.6 mm nozzle was used to print cPLA filaments, whereas a standard 0.4 mm nozzle was used to print the TPU-based filaments. A larger nozzle was used for cPLA filament to ensure good printability as the cPLA filament tends to clog when a smaller nozzle is used. The printing parameters used in this work were adopted from the settings recommended by the respective manufacturers. Table 3 summarizes the print settings that were used to print each material.

Table 2. Material combinations tested in this work

Sample types	Interface design	Material A (printed first)	Material B (printed last)
1	No modification	cPLA	TPU
2		TPU	cPLA
3	Low profile mechanical interlocking	cPLA	TPU
4		TPU	cPLA
5	Top infill modification	cPLA	TPU
6		TPU	cPLA

Abbreviations: cPLA: conductive polylactic acid; TPU: Thermoplastic polyurethane.

Table 3. Print settings for different print filaments

Settings	Materials	
	cPLA	TPU
Nozzle temperature (°C)	200	235
Print speed (mm/s)	70	50
Nozzle size (mm)	0.6	0.4
Part cooling fan	yes	no
Infill percentage	20%	15%
Infill pattern	Grid	Gyroid
Number of perimeter lines	2	2

Abbreviations: cPLA: conductive polylactic acid; TPU: Thermoplastic polyurethane.

2.3. Mechanical tests multi-material test coupons

The tensile test was conducted in accordance with ASTM D638 with some slight modifications using a universal testing machine (AGX plus 10 kN, Shimadzu). For the tensile test, a strain rate of 2 mm/min was used. The force required to pull the sample until it failed was recorded over time. The tensile stress was calculated based on the smallest cross-sectional area of the tensile coupons where the interface between the two materials was situated. Five samples were used for the tensile test to ensure the statistical significance of the results. With three different types of interfaces and two print orders, there were altogether six different coupons that have been tested, and they are summarized in Table 2.

2.4. Characterization of failure mode of the tensile coupons

The characterization of the fracture modes for the tensile coupons was performed using optical microscopy, micro-computed tomography (micro-CT) analysis, and surface roughness characterization to gain both qualitative and quantitative insights into the failure mechanisms:

(i) Optical microscopy: For the initial qualitative analysis, an optical camera was employed to capture high-resolution images of the fracture surfaces post-tensile testing. This visual inspection facilitated a comparative assessment of the macroscopic features across different coupon types, providing immediate visual cues to the nature of the bond failure, such as adhesive or cohesive fracture patterns.

(ii) Micro-CT analysis: We utilized a Bruker SkyScan 1173 micro-CT scanner to probe deeper into the internal structures in three dimensions. This non-destructive technique allowed us to construct detailed 3D representations of the internal coupon structure, including any voids, delamination, or other imperfections that contributed to the failure. The parameters set for the micro-CT scans included a source voltage of 80 kV, source current of 60 µA, image pixel size of 17.47 µm, exposure time of 850 ms, and rotation steps of 1°.

(iii) Surface roughness characterization: A Keyence VX-100 non-contact 3D laser scanning microscope was used to quantitatively measure the surface roughness at the interface. The surface topography data acquired through this method were critical for understanding the role of surface roughness in interlaminar adhesion. Specific parameters measured, including

surface area: area ratio and average roughness (Ra), are indicative of the interface's tactile profile and its potential impact on mechanical interlocking efficacy. Two out of the five coupons are randomly selected for the surface morphology investigation. In the surface morphology analysis, we used a scanned area with a size of approximately half of the cross-section's area to ensure good coverage of the fractured surface. The scan was carried out with a z-resolution of 4 μm.

3. Results and discussions

The interlaminar adhesion strength of the interface is determined by the ultimate tensile strength of the multi-material tensile coupon when the fracture happens at the interface of the coupon. The interlaminar adhesion strength of the interface between cPLA and TPU and the corresponding maximum elongations for the six different sample types are shown in Figure 3A and B, respectively. The results reveal that the interlaminar adhesion strength of coupons with no interface modifications are approximately 0.40 ± 0.03 MPa and 2.60 ± 0.07 MPa for the print order of cPLA → TPU and TPU → cPLA, respectively. For the coupons with mechanical interlocking features, it is found that the interlaminar adhesion strength of the coupons with the print order of cPLA → TPU and TPU → cPLA are 1.87 ± 0.17 MPa and 1.08 ± 0.31 MPa, respectively. For the coupons with top infill modifications, the interlaminar adhesion strength of the coupons with the print order of cPLA → TPU and TPU → cPLA is found to be 2.50 ± 0.09 MPa and 3.25 ± 0.30 MPa, respectively.

The elongation at break of the samples is shown in Figure 3B. The results reveal that the elongation at break of coupons with no interface modifications is approximately 1.30 ± 0.09% and 11.47 ± 1.27% for the print order of cPLA → TPU and TPU → cPLA, respectively. For the coupons with mechanical interlocking features, it is found that the elongation at break of the coupons with the print order of cPLA → TPU and TPU → cPLA is 38.33 ± 6.65% and 6.49 ± 2.31%, respectively. For the coupons with top infill modifications, the elongation at break of the coupons with the print order of cPLA → TPU and TPU → cPLA is found to be 7.17 ± 0.57% and 15.15 ± 2.36%, respectively.

Here, we observed that the coupons with top infill modifications generally provide a higher interlaminar adhesion strength at the interface compared to two other coupon types. Furthermore, for the cases without significant mechanical interlocking features, we observed that the interlaminar adhesion strength for the print order cPLA → TPU is generally higher than the reversed order, TPU → cPLA. Like the results of the interlaminar adhesion strength, similar trends can be observed for maximum elongation. An exception to the trend would be that the maximum elongation of the cPLA-TPU coupons is exceptionally high compared to the rest of the coupon types. One plausible explanation for the observed phenomenon is the thermal degradation of the underlying material resulting from the deposition of a material at a higher temperature. This effect is especially noticeable in the sequence of cPLA followed by TPU, where TPU is deposited at 235°C, a temperature slightly exceeding the maximum recommended temperature of 230°C for cPLA. This higher deposition temperature of TPU may lead to overheating of the underlying cPLA layer, causing thermal degradation that adversely affects the interface's mechanical properties. Conversely, in the reverse printing order of TPU followed by cPLA, the underlying material (TPU) is compatible with the processing temperature of the subsequent material (cPLA), generally resulting in better adhesion strength. This compatibility helps avoid the thermal degradation issues observed in the cPLA →TPU sequence, thus improving the bond quality at the interface. Another possible explanation for the better adhesion of TPU→ cPLA compared to cPLA →TPU is that the former has a smaller temperature difference between the underlying material and the deposited material compared to the latter, resulting in a longer duration above

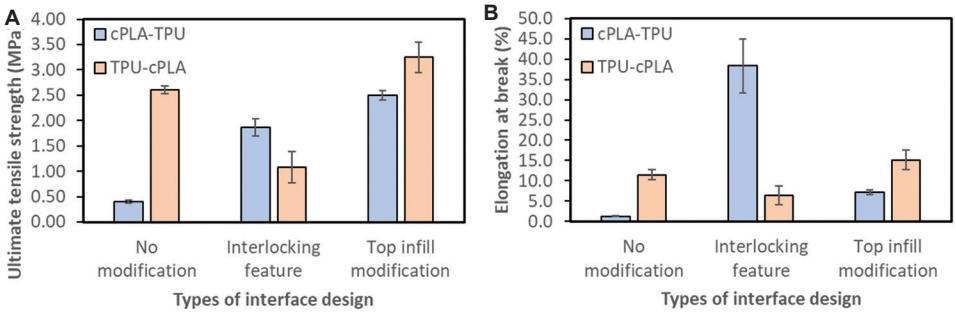

Figure 3. Graphs showing (A) the ultimate tensile strength and (B) the elongation at break of the multi-material tensile coupons in the interfacial adhesion test. The error bars represent the standard error. Abbreviations: cPLA: conductive polylactic acid; TPU: Thermoplastic polyurethane.

the glass transition temperature of materials thus better intermolecule-diffusion between the materials.[30,34]

In our investigation of interlaminar adhesion strength, we ensured that sample failures occurred at the interface between the two materials, specifically where the cross-sectional area of the coupons is the smallest, as delineated in Figure 4. Through this controlled approach, we were able to accurately assess the interface's failure mechanism and to determine the interlaminar adhesion strength for each coupon type.

Our findings revealed that the majority of the samples exhibited a clean break at the interface, with negligible remnants of the opposing material adhering to the fracture surfaces. This phenomenon was predominantly observed in the coupons featuring an unmodified interface and those with modifications to the top surface's infill, as shown in Figure 4A and C. Notably, the samples with these interfaces displayed a consistent pattern of clean separation, indicating a uniform material behavior during failure. A clean break at the interface suggests that the interfacial bond is the weakest link in the coupons since the propagation of a crack will follow the path of least resistance once a crack is initiated under stress. In other words, this suggests that the interlaminar adhesion strength between cPLA and TPU is lower than the tensile strength between these materials. This could be due to the weaker adhesive force compared to the cohesive forces within each material, resulting in a clean break on application of stress.

Conversely, samples designed with mechanical interlocking features presented a more complex failure behavior. Several of these samples did not fracture along the interface plane. Instead, breaks occurred at the smaller features of the interlocking structure, slightly offset from the intended plane, as shown in Figure 4B. This deviation was evident from the corrugated appearance of the fracture surfaces, suggesting that the mechanical interlocks contributed to a redistribution of stress, thereby altering the failure point. Notably, these failure points typically occurred at the smallest features of the interlocking structure, where stress concentration was highest. This phenomenon can be partly attributed to the rapid cooling of these small features, printed before the change in material during the dual extrusion process. The larger temperature difference between the deposition zone and the deposited material at these points likely resulted in weaker bonding.[34] Our findings highlight the significant impact of material change and extruder switching on interfacial adhesion, particularly in the context of dual extruder 3D printing systems where thermal management during printing plays a crucial role in determining bond strength.

These observations provide valuable insights into the relationship between interface design and failure mechanisms in the cPLA-TPU coupons. The distinct

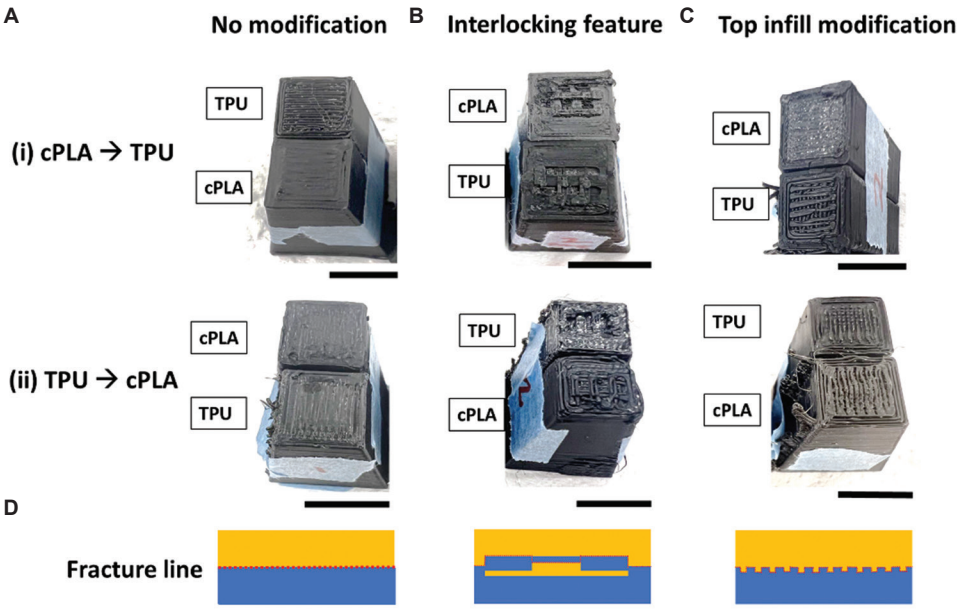

Figure 4. Images showing the typical fracture surfaces on both sides of the tested samples, namely (A) samples with no modification, (B) samples with interlocking feature, and (C) surface area-enhanced samples. The first row shows the samples with (i) the print order of cPLA → TPU, and the second row shows the samples with (ii) the print order of TPU → cPLA. The scale bars at the bottom-right corner of each image represent 1 cm. (D) The red lines in the schematics show the typical fracture lines for each type of interface. Abbreviations: cPLA: conductive polylactic acid; TPU: Thermoplastic polyurethane.

fracture characteristics (Figure 4D) between the cleanly separated samples and those with mechanical interlocks underline the influence of interface modifications on interlaminar adhesion strength and failure behavior.

Fractographic analysis was conducted to understand the failure characteristics of the 3D-printed cPLA/TPU multi-material coupons (Figure 5). All tensile samples failed at the designed interface region where the cross-section of the coupon is the smallest. For the unmodified cPLA → TPU coupons (Figure 5A-i), which exhibited the lowest interlaminar adhesion strength, the interface on the cPLA side was notably smooth and devoid of cracks or surface ruptures. In addition, only minimal marks were observed on the TPU side, indicating a weak adhesive interaction between the materials. Conversely, the TPU → cPLA counterparts displayed cracks and surface ruptures on the fracture surfaces (Figure 5A-ii), suggesting a different failure mechanism. This observation was also consistent for coupons modified with top infill, for both print orientations (Figure 5C-i and C-ii). Despite similar surface characteristics, these modified samples demonstrated significantly higher interlaminar adhesive strength than the unmodified cPLA → TPU coupons. This suggests that the modifications introduce a stronger adhesive force between cPLA and TPU, which is sufficient to initiate cracks and surface rupture upon failure. For coupons featuring interlocking modifications, the fracture surfaces revealed broken interlocking features on both materials (Figure 5B-i and B-ii), indicating that the failure mechanism involved the complete rupture of these fine interlocking elements. This finding shows the effectiveness of the interlocking design in enhancing the mechanical interlocking of the materials, leading to a different failure mode compared to unmodified interfaces.

To further analyze the surface morphology of the fracture surfaces of the coupons, we used confocal microscopy to scan the fractured interfaces (Figure 6). Since both the coupons with unmodified interface and top infill modification showed cleanly separated samples, the confocal microscopy on the fractured surfaces of these samples could shed some light on the how the surface morphology of these samples affects the interlaminar

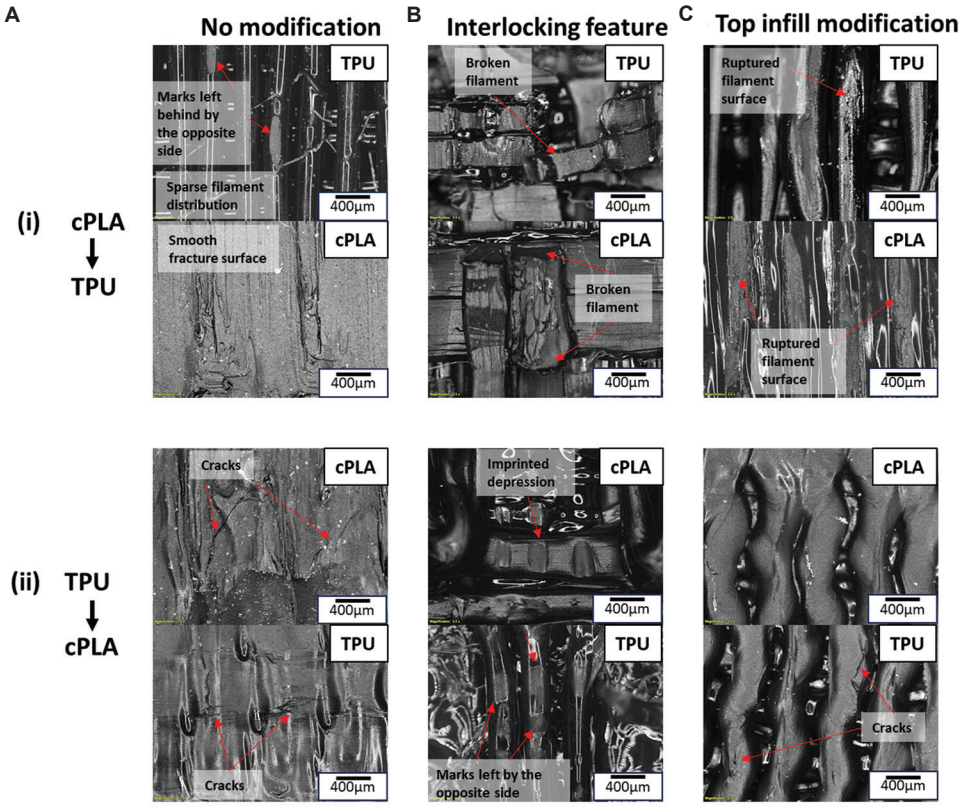

Figure 5. Fracture surfaces of various multi-material coupons with different interface design and print order. Columns (A), (B), and (C) show samples with no modification, interlocking feature, and top infill modification, respectively, and rows (i) and (ii) show samples with print order of cPLA → TPU and TPU → cPLA, respectively. Abbreviations: cPLA: conductive polylactic acid; TPU: Thermoplastic polyurethane.

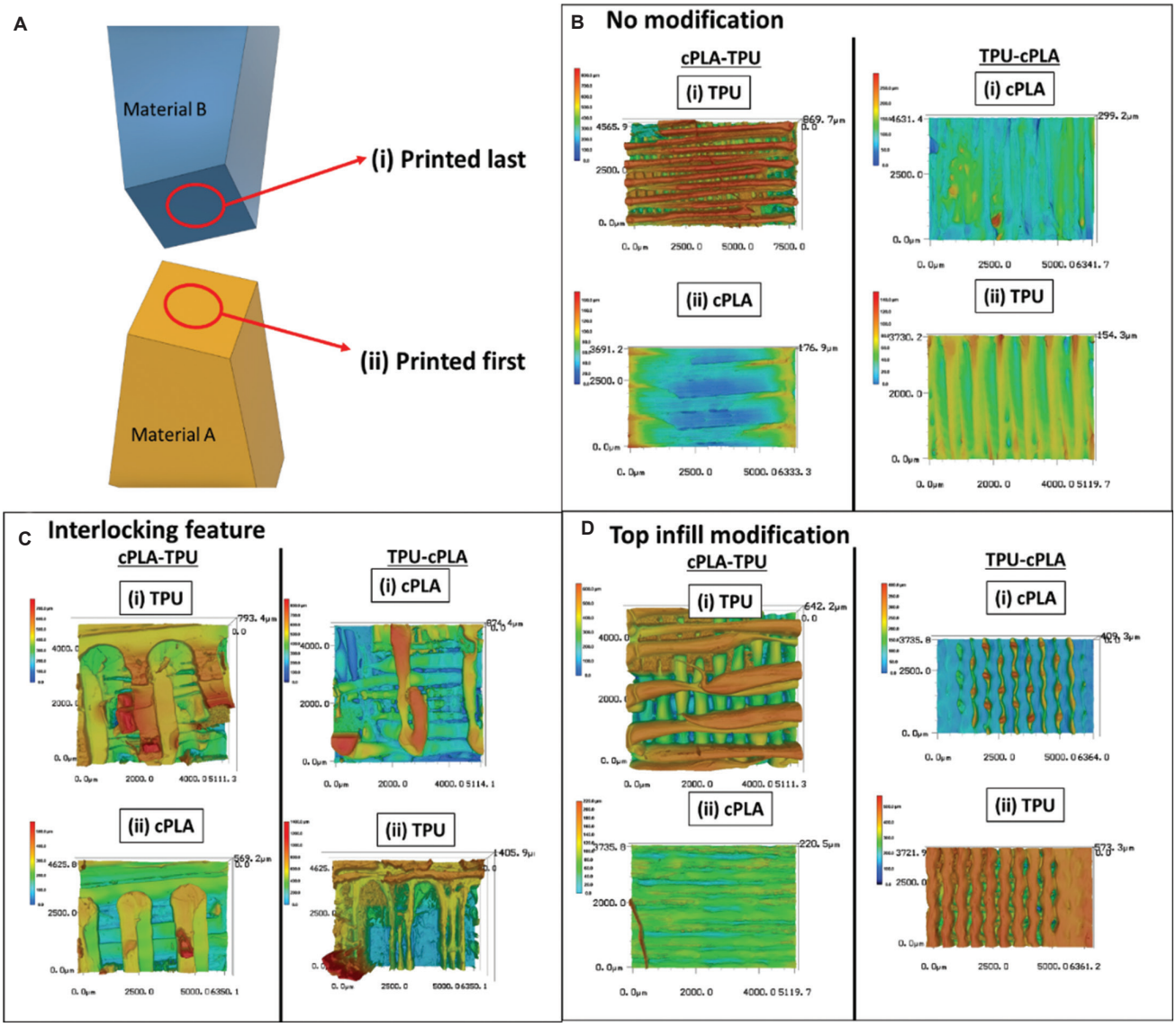

Figure 6. (A) Schematic showing the labels of two scanned fracture surfaces, with (i) representing the fracture surface of the material that is printed last and (ii) representing the fracture surface of the material that is printed first (B–D) 3D reconstructed height map showing the typical surface morphology of the fracture surfaces of the interfaces of coupons for no modification, interlocking feature, and top infill modification, respectively. Abbreviations: cPLA: conductive polylactic acid; TPU: Thermoplastic polyurethane.

adhesion strength and the fracture mode. In particular, we wanted to observe the surface morphology of the material situated below the interface (the material that is printed first). In both cases, we observed that the coupons have a relatively flat surface with some undulations scattered over the region. For the case of coupons with unmodified interface, the surface appears to be relatively flat with very few grooves or valleys, as shown in Figure 6B-ii, regardless of the print order. Similar observations can also be made for the coupons with top infill modifications, but with a much wider grooves scattered over the flat fractured surface. The difference in the surface morphology can be attributed to the design/toolpath that is being used to print the topmost layer of the first material. It is widely known that FFF printing inherently produces parts with grooves form between the filaments, explaining why some small grooves and valleys are observed on the fractured surface of the coupons with unmodified interface. In contrast, for the case of coupons with top infill modification, we intentionally made the gaps between the filament significantly larger, making the filament on the topmost layer sparsely distributed. This explains why the sparsely distributed filaments appear as the peaks in the height map. Figure 6B-i and D-i show the surface morphology of the

fractured surfaces of the opposing side (the material that is printed last) of the coupons with unmodified interface and top infill modifications. More peaks were observed on the fractured surfaces of these coupons, suggesting possible impregnation of material from the top material into the grooves on the top layer of the bottom material. These impregnated material increases the surface area between the materials at the interface, which are responsible for the adhesion through surface adsorption and mechanical interlocking. Figure 6C, on the other hand, shows the surface morphology of the coupon with interlocking features. It is observed that these coupons generally have much rougher surfaces regardless of the print order compared with the other two cases due to uniform fracture lines that form across the interface.

To enhance our quantitative analysis of the fractured surfaces, we employed two specific metrics to evaluate surface roughness: (i) the ratio of surface area to projected area (R_{Sa-A}) and (ii) the average surface roughness (R_a), as shown in Figure 7. The R_{Sa-A} metric serves to quantify the effective surface area available for adsorption phenomena, providing insights into the potential interfacial adhesion capacity. On the other hand, R_a offers a measure of the mean surface texture or topography created during fracture. This parameter is instrumental in assessing the extent to which mechanical interlocking contributes to surface adhesion, as it reflects the microscale irregularities that can enhance mechanical bonding between the interfaces for the case of samples with clean separation. Although the evaluation may not be meaningful for the coupons with interlocking features, the values are also reported here for the sake of comprehensiveness and comparison purposes.

In general, it is observed that both R_{Sa-A} and R_a exhibit almost similar trend for all cases. To ensure conciseness, we combine the discussion of both metrics and use surface roughness indicator (SRI) as the general term to describe both metrics. We evaluated the SRI (R_{Sa-A} and R_a) of the fractured surfaces of the material that is being printed first, as shown in Figure 7A and B. The SRI shows that there is a slight increase in R_{Sa-A} and R_a when comparing the coupons with top infill modifications to the baseline coupons that have unmodified interface. This also helps explain why there is a slight increment in the interlaminar adhesion strength of the coupons with top infill modification. The highly uneven fractured surface of the coupons with interlocking features can also be reflected by the high magnitude of the SRI. Likewise, a comparable trend was observed on the SRI of the corresponding opposite surfaces of the fractures, as these surfaces would essentially constitute the negative imprint of the fracture patterns observed on the initial side, as shown in Figure S1.

In general, the presence of internal voids within the structure can lead to mechanical imperfections, which, in turn, contribute to stress concentration and facilitate crack propagation under tensile load. This phenomenon results in diverse tensile behaviors, as these voids become critical factors in determining the material's mechanical response during testing. A micro-CT analysis was conducted on the three types of coupons to understand how different interface designs affect the formation of pores and defect within the printed structures near the interface (Figure 8A). Here, we observed that coupons with no modifications have a porosity level of approximately 1.47% near the interface region, which is slightly higher compared to that of the 0.64% of the fully printed regions. Similarly, the coupon with interlocking features also has a porosity level of approximately 5.6%. Likewise, the coupons with top infill modifications exhibit a porosity level of approximately 2.1% only (Figure 8B), which is slightly higher than that of the coupons with unmodified interface used in this work. A comparison of the ultimate tensile strength of the samples to the corresponding surface properties and the porosity level at the interface is presented in Table 4. The pronounced influence of porosity on the ultimate

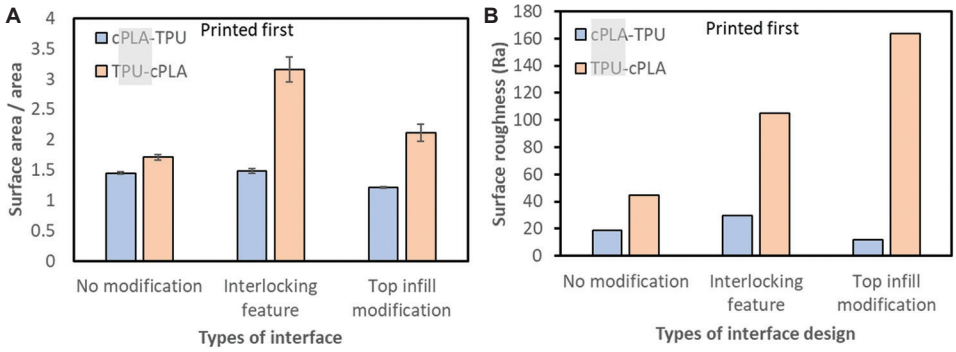

Figure 7. Graphs showing the (A) surface area/area ratio (the error bars represent standard error) and (B) surface roughness (R_a) for the interfaces that are printed first. Abbreviations: cPLA: conductive polylactic acid; TPU: Thermoplastic polyurethane.

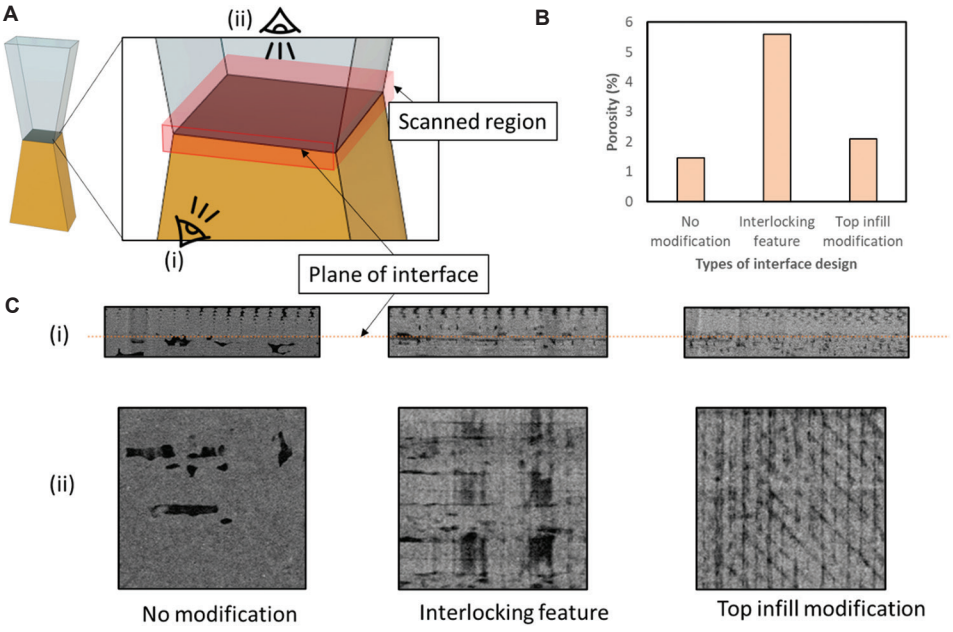

Figure 8. (A) Schematic showing the scanned region at the interface of the multi-material sample. (B) A graph showing the porosity level at the interface of various samples. (C) X-ray images showing the (i) side view at the interface and (ii) the plan view at the interface of various samples.

Table 4. Comparison between the ultimate tensile strength of the interface to their surface properties, and porosity levels at the interface

Interface design	Print order (bottom-top)	Ultimate tensile strength (MPa)	Surface area/ projected area	Surface roughness, R_a (μm)	Porosity level (%)
No modification	cPLA-TPU	0.399±0.029	1.45±0.09	19	1.47
	TPU-cPLA	2.601±0.076	1.71±0.19	45	
Interlocking feature	cPLA-TPU	1.87±0.170	1.49±0.11	30	5.60
	TPU-cPLA	1.08±0.310	3.15±0.63	105	
Top infill modification	cPLA-TPU	2.495±0.093	1.22±0.49	12	2.10
	TPU-cPLA	3.251±0.301	2.11±0.04	164	

Abbreviations: cPLA: conductive polylactic acid; TPU: Thermoplastic polyurethane.

tensile strength (UTS) of the samples is evident when comparing those with interlocking features to those with top infill modification. Despite the assumption that the interlocking feature should offer a larger interfacial area conducive to stronger adhesion, the UTS of these samples is generally lower than that of the samples with top infill modification. This discrepancy can be attributed to the higher levels of porosity present in the samples with interlocking features, which adversely affect their mechanical strength. The higher porosity near the interface region found in these coupons (as depicted in Figure 8C–E) could be attributed to the manufacturing error caused by the misalignment of the nozzles and poor bed leveling, resulting in inaccurate and improper material deposition over the underlying material during the start and end of the material extrusion process.

For the case of coupons with top infill modification, the increased porosity level compared to that of the coupons with unmodified interface can be attributed to the improper impregnation of the top material into the grooves in the underlying material, although the nozzle is marginally brought closer to the substrate to promote stronger flow into the grooves. Nevertheless, the interlaminar adhesion strength is still higher than that of the unmodified interface. This can be attributed to the increased effective surface area between the two materials as discussed earlier resulted by the corrugated interface formed by the toolpath design. This approach ensures that the extruded material is pressed into the grooves of the underlying layer, thereby enhancing the effective surface area at the interface and promoting better interlayer adhesion. This explains why the coupons

with top infill modification have the highest interlaminar adhesion strength.

In addition to increasing the surface area, the various types of interfaces employed in our study also significantly influenced the diffusion of molecular chains at the interface between cPLA and TPU. This diffusion process is critically dependent on the thermal dynamics during printing, where temperature plays a pivotal role.[35] As the printing process involves both cooling of the previously deposited layer and reheating due to subsequent layer deposition, these thermal events occur simultaneously and have a substantial impact on the adhesion mechanism. The reheating of the underlying layer on deposition of a new layer facilitates the diffusion of molecular chains across the interface, potentially leading to stronger bonding. This effect is particularly pronounced in the presence of mechanical interlocks, where the increased surface area and complex geometries create more opportunities for molecular intermingling. The thermal history of each layer, including the peak temperature reached and the cooling rate, thus becomes a critical factor in determining the strength and quality of the interfacial bond. This complex interplay of temperature, cooling, and reheating underscores the importance of optimizing printing parameters to enhance molecular diffusion at the interface, thereby improving the overall structural integrity of the multi-material print.

4. Conclusion

This study provides some insights into the interlaminar adhesion strength of multi-material interfaces, specifically between cPLA and TPU. In this work, we investigated three different types of coupons (unmodified interface, interface with interlocking feature, and interface with top infill modification) with two opposing print orders. Through our experiments, we observed that the failure of samples predominantly occurred at the interface, with most specimens exhibiting a clean break with minimal residual material from the opposing surface. This behavior underscores the importance of interface design in multi-material 3D printing. We quantitatively assessed the surface roughness characteristics of the fractured interfaces, employing metrics such as $R_{Sa\text{-}A}$ and R_a. Our findings revealed that the printing order and interface modifications significantly impact the roughness parameters, which, in turn, affect the mechanical interlocking and adhesion properties. In addition, the decrease in porosity at the interface can be linked to the optimized nozzle positioning during printing, which promotes the extruded material to conform into the grooves of the underlying layer, resulting in an increased effective surface area for adhesion. Our results indicated that the interface incorporating top infill modifications demonstrated superior interlaminar adhesion strength, achieving a minimum enhancement of 25% relative to the standard benchmark coupon.

These results have far-reaching implications for the design and manufacturing of multi-material components, where interlayer adhesion is critical. They pave the way for improved application-specific material selection and the development of advanced printing strategies that can enhance the structural integrity of 3D-printed materials. Future work should focus on the optimization of interface designs to maximize adhesion strength, while also exploring the influence of various printing parameters on the mechanical properties of multi-material prints. Furthermore, the potential for scaling these findings to industrial manufacturing processes presents a promising avenue for the production of complex, high-strength multi-material assemblies.

Acknowledgments

None.

Funding

This research is supported by the Agency for Science, Technology and Research (A*STAR) under its IAF-ICP Program I2001E0067 and the Schaeffler Hub for Advanced Research at NTU and the National Research Foundation, Prime Minister's Office, Singapore under its Medium-Sized Center funding scheme.

Conflict of interest

The authors declare that they have no competing interests.

Author contributions

Conceptualization: Guo Liang Goh
Formal analysis: Guo Liang Goh
Funding acquisition: Wai Yee Yeong, Boon Siew Han
Investigation: Guo Liang Goh, Samuel Lee, Shi Hui Cheng, Pothunuri Laya, Daniel Jee Seng Goh
Methodology: Guo Liang Goh, Samuel Lee
Project administration: Boon Siew Han
Writing – original draft: Guo Liang Goh
Writing – review & editing: Wai Yee Yeong, Van Pho Nguyen

Ethics approval and consent to participate

Not applicable.

Consent for publication

Not applicable.

Availability of data

Data are available from the corresponding author on reasonable request.

References

1. Goh GL, Agarwala S, Goh GD, *et al*. Additively manufactured multi-material free-form structure with printed electronics. *Int J Adv Manuf Technol*. 2018;94(1):1309-1316.

   doi: 10.1007/s00170-017-0972-z

2. Goh GL, Tay MF, Lee JM, *et al*. Potential of printed electrodes for electrochemical impedance spectroscopy (EIS): Toward membrane fouling detection. *Adv Electron Mater*. 2021;7(10):2100043.

   doi: 10.1002/aelm.202100043

3. Goh GL, Zhang H, Chong TH, Yeong WY. 3D printing of multilayered and multimaterial electronics: A review. *Adv Electron Mater*. 2021;7(10):2100445.

   doi: 10.1002/aelm.202100445

4. Goh GD, Agarwala S, Goh GL, Dikshit V, Sing SL, Yeong WY. Additive manufacturing in unmanned aerial vehicles (UAVs): Challenges and potential. *Aerospace Sci Technol*. 2017;63:140-151.

   doi: 10.1016/j.ast.2016.12.019

5. Soetedjo AAP, Lee JM, Lau HH, *et al*. Tissue engineering and 3D printing of bioartificial pancreas for regenerative medicine in diabetes. *Trends Endocrinol Metab*. 2021;32(8):609-622.

   doi: 10.1016/j.tem.2021.05.007

6. Cuan-Urquizo E, Guerra Silva R. Fused filament fabrication of cellular, lattice and porous mechanical metamaterials: A review. *Virtual Phys Prototyp*. 2023;18(1):e2224300.

   doi: 10.1080/17452759.2023.2224300

7. Ribeiro M, Sousa Carneiro O, Ferreira da Silva A. Interface geometries in 3D multi-material prints by fused filament fabrication. *Rapid Prototyp J*. 2019;25(1):38-46.

   doi: 10.1108/RPJ-05-2017-0107

8. Englert L, Heuer A, Engelskirchen MK, *et al*. Hybrid material additive manufacturing: Interlocking interfaces for fused filament fabrication on laser powder bed fusion substrates. *Virtual Phys Prototyp*. 2022;17(3):508-527.

   doi: 10.1080/17452759.2022.2048228

9. Brancewicz-Steinmetz E, Sawicki J, Byczkowska P. The influence of 3D printing parameters on adhesion between polylactic acid (PLA) and thermoplastic polyurethane (TPU). *Materials* (*Basel*). 2021;14(21):6464.

   doi: 10.3390/ma14216464

10. Tamburrino F, Graziosi S, Bordegoni M. The influence of slicing parameters on the multi-material adhesion mechanisms of FDM printed parts: An exploratory study. *Virtual Phys Prototyp*. 2019;14(4):316-332.

    doi: 10.1080/17452759.2019.1607758

11. Freund R, Watschke H, Heubach J, Vietor T. Determination of influencing factors on interface strength of additively manufactured multi-material parts by material extrusion. *Appl Sci*. 2019;9(9):1782.

    doi: 10.3390/app9091782

12. Rodriguez C, Narahara H, Koresawa H, Hisayuki N, Akimitsu S. Enhancement of Electrically Conductive FDM Parts Adhesion Strength to Different Polymers through Atmospheric Pressure Plasma Treatment. In: Proceedings of JSPE Semestrial Meeting 2017 JSPE Spring Conference; 2017. p. 1025-1026.

    doi: 10.11522/pscjspe.2017S.0_1025

13. Penter L, Maier J, Kauschinger B, Lebelt T, Modler N, Ihlenfeldt S. 3D Printing Technology for Low Cost Manufacturing of Hybrid Prototypes from Multi Material Composites. Berlin, Heidelberg: Springer; 2021. p. 396-405.

    doi: 10.1007/978-3-662-62138-7_40

14. Rodriguez C, Narahara H, Koresawa H, Hisayuki N. The Effect of Atmospheric Pressure Plasma on Inter-Laminar Adhesion Strength of FDM Parts Manufactured with Different Functional Polymers. In: Proceedings of JSPE Semestrial Meeting 2019 JSPE Spring Conference; 2019. p. 519-520.

    doi: 10.11522/pscjspe.2019S.0_519

15. Tao R, Shi J, Granier F, Moeini M, Akbarzadeh A, Therriault D. Multi-material fused filament fabrication of flexible 3D piezoelectric nanocomposite lattices for pressure sensing and energy harvesting applications. *Appl Mater Today*. 2022;29:101596.

    doi: 10.1016/j.apmt.2022.101596

16. Roach DJ, Hamel CM, Dunn CK, Johnson MV, Kuang X, Qi HJ. The m4 3D printer: A multi-material multi-method additive manufacturing platform for future 3D printed structures. *Addit Manuf*. 2019;29:100819.

    doi: 10.1016/j.addma.2019.100819

17. Fenollosa F, Gomà JR, Buj-Corral I, *et al*. Foreseeing new multi-material FFF-additive manufacturing concepts meeting mimicking requirements with living tissues. *Procedia Manuf*. 2019;41:1063-1070.

    doi: 10.1016/j.promfg.2019.10.034

18. Stano G, Ovy SAI, Percoco G, Zhang R, Lu H, Tadesse Y. Additive manufacturing for bioinspired structures: Experimental study to improve the multimaterial adhesion between soft and stiff materials. *3D Print Addit Manuf*. 2023;10(5):1080-1089.

    doi: 10.1089/3dp.2022.0186

19. Goh GL, Goh GD, Nguyen VP, *et al*. A 3D printing-enabled artificially innervated smart soft gripper with variable joint stiffness. *Adv Mater Technol*. 2023;8(24):2301426.

doi: 10.1002/admt.202301426

20. Jiao J, Guo Y, Tong Q, *et al*. Stiffness-tunable and shape-locking soft actuators based on 3D-printed hybrid multi-materials. *Soft Sci*. 2022;2(4):20.

doi: 10.20517/ss.2022.19

21. Goh GL, Huang X, Toh W, *et al*. Joint angle prediction for a cable-driven gripper with variable joint stiffness through numerical modeling and machine learning. *Int J AI Mater Des*. 2024;1(1):2328.

doi: 10.36922/ijamd.2328

22. Awaja F, Gilbert M, Kelly G, Fox B, Pigram PJ. Adhesion of polymers. *Prog Polymer Sci*. 2009;34(9):948-968.

doi: 10.1016/j.progpolymsci.2009.04.007

23. Kwon N, Deshpande H, Hasan MK, Darnal A, Kim J. Multi-ttach: Techniques to Enhance Multi-material Attachments in Low-cost FDM 3D Printing. In: Presented at: Proceedings of the 6th Annual ACM Symposium on Computational Fabrication Virtual Event, USA; 2021.

doi: 10.1145/3485114.3485116

24. Kakaraparthi S, Chen N. A multi-material additive manufacturing virtual prototyping method for design to improve part strength. *Int J Adv Manuf Technol*. 2023;127:1-12.

doi: 10.1007/s00170-023-11660-2

25. Hasanov S, Gupta A, Nasirov A, Fidan I. Mechanical characterization of functionally graded materials produced by the fused filament fabrication process. *J Manuf Processes*. 2020;58:923-935.

doi: 10.1016/j.jmapro.2020.09.011

26. Mustafa I, Kwok TH. Interlacing infills for multi-material fused filament fabrication using layered depth material images. *Micromachines*. 2022;13(5):773.

doi: 10.3390/mi13050773

27. Rendas P, Figueiredo L, Geraldo M, Vidal C, Soares BA. Improvement of tensile and flexural properties of 3D printed PEEK through the increase of interfacial adhesion. *J Manuf Processes*. 2023;93:260-274.

doi: 10.1016/j.jmapro.2023.03.024

28. Rodriguez JF, Thomas JP, Renaud JE. Characterization of the mesostructure of fused-deposition acrylonitrile-butadiene-styrene materials. *Rapid Prototyp J*. 2000;6(3):175-186.

doi: 10.1108/13552540010337056

29. Brancewicz-Steinmetz E, Valverde Vergara R, Buzalski V, Sawicki J. Study of the adhesion between TPU and PLA in multi-material 3D printing. *J Achiev Mater Manuf Eng*. 2022;115(2):49-56.

30. Yin J, Lu C, Fu J, Huang Y, Zheng Y. Interfacial bonding during multi-material fused deposition modeling (FDM) process due to inter-molecular diffusion. *Mater Des*. 2018;150:104-112.

doi: 10.1016/j.matdes.2018.04.029

31. Gao X, Qi S, Kuang X, Su Y, Li J, Wang D. Fused filament fabrication of polymer materials: A review of interlayer bond. *Addit Manuf*. 2021;37:101658.

doi: 10.1016/j.addma.2020.101658

32. Cunha P, Teixeira R, Carneiro O, Silva A. Multi-material fused filament fabrication: An expedited methodology to assess the affinity between different materials. *Prog Addit Manuf*. 2023;8(2):195-204.

doi: 10.1007/s40964-022-00322-6

33. Kalia K, Ameli A. Interfacial Bond Strength of Various Rigid/Soft Multi-Materials Printed via Fused Filament Fabrication Process. New York: American Society of Mechanical Engineers; 2020.

doi: 10.1115/SMASIS2020-2298

34. Vanaei HR, Raissi K, Deligant M, *et al*. Toward the understanding of temperature effect on bonding strength, dimensions and geometry of 3D-printed parts. *J Mater Sci*. 2020;55(29):14677-14689.

doi: 10.1007/s10853-020-05057-9

35. Srinivas V, van Hooy-Corstjens CSJ, Rastogi S, Harings JAW. Promotion of molecular diffusion and/or crystallization in fused deposition modeled poly(lactide) welds. *Polymer*. 2020;202:122637.

doi: 10.1016/j.polymer.2020.122637

36. Watschke H, Waalkes L, Schumacher C, Vietor T. Development of novel test specimens for characterization of multi-material parts manufactured by material extrusion. *Appl Sci*. 2018;8(8):1220.

doi: 10.3390/app8081220

ACCSCIENCE PUBLISHING

Materials Science in Additive Manufacturing

ORIGINAL RESEARCH ARTICLE

Role of customized scan strategies and dwell time on microstructure and properties of additively manufactured 316L stainless steel

Puskar Pathak[1,2,3]*, Goran Majkic[1,2,3], and Venkat Selvamanickam[1,2,3]

[1]Advanced Manufacturing Institute, University of Houston, Houston, Texas, United States of America

[2]Department of Mechanical Engineering, University of Houston, Houston, Texas, United States of America

[3]Texas Center for Superconductivity, University of Houston, Houston, Texas, United States of America

Abstract

Direct energy deposition (DED)-based additive manufacturing facilitates fabrication of medium-to-large functional parts. This study assesses the role of varying scan strategies and dwell time between each layer to control the cooling rate of 316L stainless steel produced by the laser-engineered net shaping-DED method. Customized print patterns were designed, keeping other optimized print parameters constant to obtain printed parts with better dimensional tolerance. The parts, which were >99% dense, were fabricated in a controlled argon environment. A heterogeneous microstructure consisting of a cellular columnar and equiaxed substructure was obtained. Two-dimensional X-ray diffraction revealed the presence of a single-phase γ-austenitic FCC phase. A refined microstructure with less elemental segregation was noticed with an increase in dwell time between the print layers. Internal defect analysis using X-ray micro-computed tomography revealed low lack-of-fusion voids along the build direction without any micro-cracks, which is attributed to higher cooling rates between subsequent print layers. As demonstrated in a mechanical performance evaluation of tensile and micro-hardness properties, better performance can be achieved by controlling the cooling rate and customizing deposition patterns.

Keywords: Additive manufacturing; Scan strategy; Dwell time; LENS-DED; 316L stainless steel

***Corresponding author:**
Puskar Pathak
(ppathak3@cougarnet.uh.edu)

Citation: Pathak P, Majkic G, Selvamanickam V. Role of customized scan strategies and dwell time on microstructure and properties of additively manufactured 316L stainless steel. *Mater Sci Add Manuf.* 2024;3(1):2676.
doi: 10.36922/msam.2676

Received: January 8, 2024

Accepted: February 19, 2024

Published Online: March 8, 2024

1. Introduction

Additive manufacturing (AM) has transitioned from its initial use in rapid prototyping to becoming a significant player in high-value manufacturing sectors such as aerospace, automotive, and medical industries. AM enables innovative geometries and delivers advantages such as reduced weight, minimized material wastage, lower part expenses, component consolidation, and improved overall performance.[1-4] Among various AM techniques, the direct energy deposition (DED) technique offering a high deposition rate is the arc wire DED technique.[5,6] Numerous studies have recently been conducted on the applicability of this method to various structural alloys, such as stainless steels[7-12] and Ni-based superalloys.[13-15] However, the surface quality of the products manufactured

by this technique is low. In contrast, the engineered net shaping (LENS) technique also offers flexibility, efficiency, and the ability to produce complex, large-scale parts with a variety of materials in addition to better surface quality, making it valuable in various industries and applications.[2,16-19] Various process parameters including layer thickness, print speed, laser power, printing patterns and orientations, cooling rate, *etc.*, in AM can significantly influence different properties of the produced parts.[1,9,10,13,14] Understanding how these process parameters influence properties is crucial for optimizing the AM process to meet specific design requirements and quality standards for the final printed parts.

The LENS-based DED process has a default deposition pattern, starting with the outer contour deposition and then proceeding to the alternative raster contour to create hatch lines.[9,15,16] Ribeiro *et al.* studied different deposition strategies with the DED process and their influence on mechanical properties.[17] There is a huge interest in exploring alternative (customized) deposition patterns for the LENS-based DED process. In addition, with the LENS-based DED technique, there is an opportunity to explore inter-layer dwell time between each print layer so as to control the laser energy intensity to enable better cooling rate control within the print layers.[18,20] Denlinger *et al.* investigated the influence of inter-layer dwell time on distortion and residual stress in titanium and nickel alloys.[21] While increasing the pause time between print layers unavoidably lengthens the total printing time, it merits consideration due to its potential influence on microstructure and properties.

In this study, an emphasis was placed on investigating the role of customized scan strategies and dwell time in between the print layers of 316L stainless steel (SS) using the DED technique. The current work is an extended research of previous work, a parametric study summarizing the optimization of process parameters to obtain fully dense functional AM parts.[10] The optimized parameters from the previous study were utilized[10] in this study, and two new print parameters – customized scan patterns and dwell time between print layers – were added to get an in-depth understanding of the printing process.

2. Materials and methods

2.1. Materials

The gas-atomized 316L SS from Carpenter Additive (USA) was used to produce the test sample parts. Figure 1A shows the scanning electron microscopy (SEM) images of the spherical gas-atomized 316L SS powder, and Table 1 shows the energy dispersive X-ray spectroscopy (EDS) data of the 316L SS powder. The particle size distribution (PSD) of D50= 58 µm was recorded for the spherical powder based on SEM image (Figure 1B). X-ray micro-computed tomography (micro-CT) was performed, as elaborated in section 2.2, with Skyscan 2214 Bruker micro-CT system (BRUKER, USA) using 0.5 mm Cu filter at 1.75 µm pixel resolution to assess the 316L SS powder quality. The 3D reconstructed image of 316L SS powder is shown in Figure 2A, and the X-Y cross-sectioned image in Figure 2B depicts a minor trace of internal pores.

2.2. Experimental methods

MTS 500 hybrid AM tool built by Optomec was used to deposit 316L SS powder onto 304 SS substrate to fabricate

Table 1. Energy dispersive X-ray spectroscopy data of 316L stainless steel powder

	Elements (wt. %)					
Spot no.	Fe	Cr	Ni	Mo	Si	Mn
1	65.47	18.93	11.89	1.73	0.96	0.56
2	64.52	19.43	12.18	1.95	0.94	0.81
3	64.91	19.44	12.48	1.58	0.53	1.15

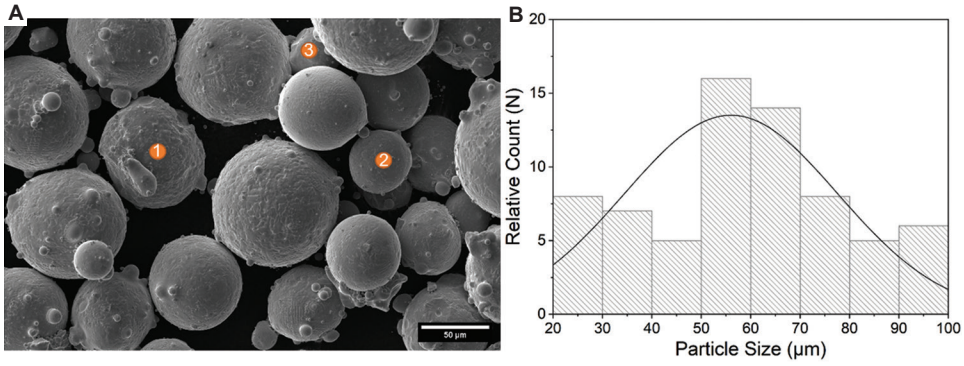

Figure 1. (A) Scanning electron microscopy image with energy dispersive X-ray spectroscopy points, corresponding to energy dispersive spectroscopy data in Table 1; (B) particle size distribution of 316L stainless steel powder.

the sample in 10 × 10 × 10 mm^3 dimensions. The print parameters were laser power of 340 watts, scanning speed of 16 mm/s, powder feed rate of 7.89 g/min, laser spot size of 0.5 mm, layer height of 0.5 mm, and specific energy (E) of 21.25 J/mm^2. These parameters were replicated from the previous parametric optimization study.[10] A Nd: YAG laser with a wavelength of 1068.7 nm was used with a standoff distance of 9.525 mm. As shown in Figure 3, the parts were printed in customized unidirectional and bidirectional scan patterns with 0, 10, and 15 s of dwell time in between the print layers in a controlled argon (Ar) atmosphere. The first three samples (*i.e.*, S1, S2, S3) were printed in a unidirectional scan pattern where the toolpath was consistent, and there were no abrupt changes in deposition direction. The remaining three samples (*i.e.*, S4, S5, S6) were printed in a bidirectional scan pattern where the beam direction is reversed in each pass, and the starting location of the beam is moved diagonally away from the end location of the prior layer.

After the parts were printed, they were cut into sections using an electric hacksaw. These sectioned samples were cleaned in an ultrasonic bath and subsequently embedded in epoxy resin, oriented along the build direction, to prepare them for metallographic analysis. To examine the microstructure, the samples were etched using a solution containing 15 mL HCl, 10 mL HNO_3, and 10 mL acetic acid for 30 s. Further characterizations were carried by means of scanning electron microscopy (SEM) and energy dispersive spectroscopy (EDS) using a Thermo Fisher Axia ChemiSEM (ThermoFisher Scientific, USA), utilizing a spot size of 0.1 µm to elicit quantitative elemental composition and mapping information. The density of the samples was determined using the Ohaus density determination kit (OHAUS, USA), which is based on the Archimedes' principle.[22] In addition, the ZeGage Plus 3D profilometer (Zygo Corporation, USA) was utilized to measure the roughness of the as-printed parts and create 3D roughness maps.

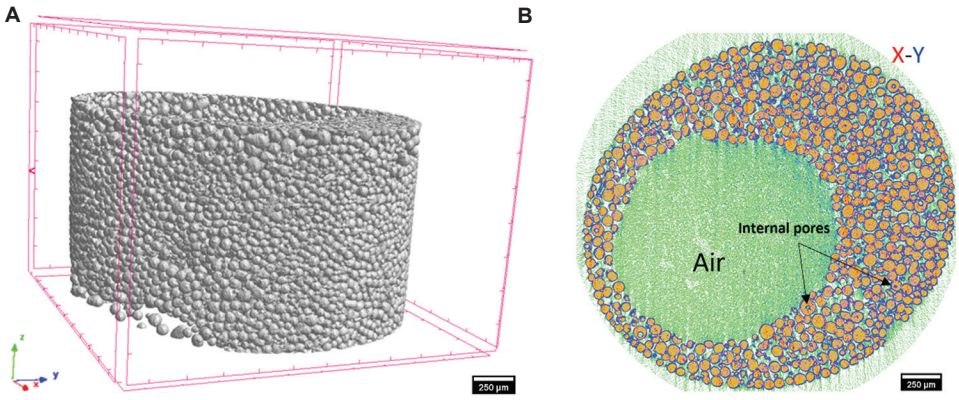

Figure 2. (A) Powder 316L stainless steel micro-computed tomography analysis; (B) X-Y cross section showing the presence of minor internal pores.

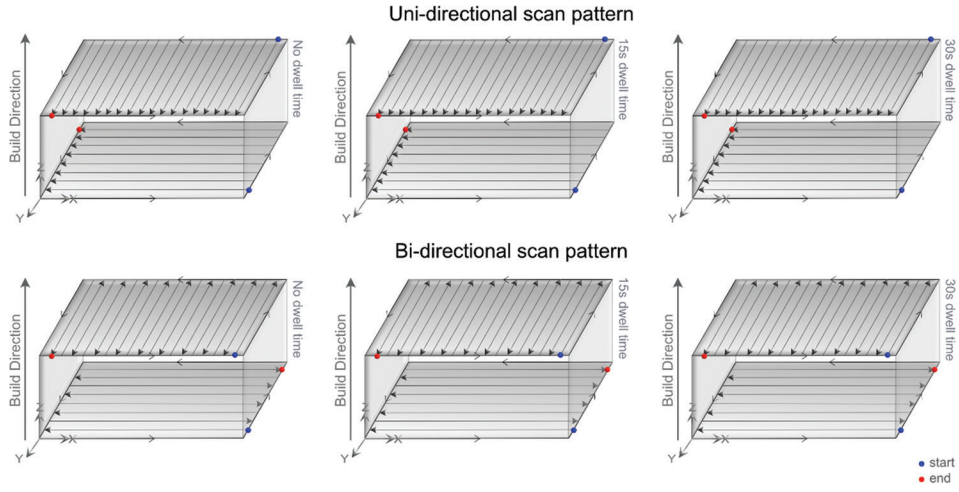

Figure 3. Schematic depicting the printed samples with different scan patterns and dwell times.

Two-dimensional X-ray diffraction (2D-XRD) analysis was conducted using a Bruker D8 DISCOVER instrument (BRUKER, USA) equipped with a Vantec 500 General Area Diffraction Detector (GADDS) (BRUKER, USA).[23,24] The samples were scanned using a Cu Kα radiation source with a wavelength (λ) of 1.54 Å, with an electrical voltage of 50 kV and a current of 1000 mA. A beam size of 0.5 mm was used for all scans. For the acquisition of rocking curve scans, a total of four sequential GADDS frames (detector positions) were captured, each frame having an exposure time of 240 s. Furthermore, {111} pole figure scans were performed, with the detector positioned at {111} orientation, while the sample was rotated about the surface normal (ϕ-scan) over a full 360° range in 1° increments, with each exposure lasting 10 s. To investigate the variation of crystallographic orientation along the build direction, each sample was scanned at two different positions, namely the top and bottom along the build direction.

Micro-indentation testing was conducted on the epoxy-mounted finished samples utilizing the Micro Combi Tester: MCT^3 indentation system. During this testing, a maximum loading force of 5 N was applied, with a loading and unloading rate set at 1000 mN/min. In addition, there was a 10-s dwell time at the maximum load point during each indentation. To ensure the reliability of the measured results, an average of five indentations were performed at three different locations: top, middle, and bottom sections along the build direction. The reduced elastic modulus (E*) was determined using the Oliver–Pharr method.[25,26] Tensile testing was performed using Instron 5969 at room temperature at 10^{-3} s^{-1} nominal strain rate using ASTM E8 standard. The cylindrical test specimens were printed vertically along the build direction. Before tensile testing, the gauge length of the tensile specimens was assessed for the internal defects analysis using a Skyscan 2214 Bruker micro-CT system coupled with 0.5 mm Cu filter at 1.75 µm pixel resolution under 140 kV source voltage and 52 µA current. To assess the layer-wise porosity and visualize any internal defects, a 3D model of the scanned samples was generated.[27,28] This involved masking the bulk metallic material and the air volume within the samples, ultimately allowing for the determination of the volume fraction of pores within the specimens.

3. Results

3.1. Relative density and surface roughness

As shown in Table 2, an average density >99% was obtained with slight improvement in bidirectional printed samples (*i.e.*, S4, S5, and S6) compared to unidirectional printed samples (*i.e.*, S1, S2, and S3). Table 2 also includes the average surface roughness (S_a) of the printed samples. The average S_a value was relatively lower for unidirectional scans compared to bidirectional samples, possibly due to the consistency of the toolpath in unidirectional printing and the absence of abrupt direction changes.[15]

3.2. Microstructure analysis

Figure 4 displays SEM images of two samples: unidirectional S1 (Figure 4A and B) and bidirectional S4 (Figure 4C and D). The microstructure harbors several sub-cellular structures comprising both elongated cell structures and equiaxed substructures, along with a minor presence of pores. These variations arise from differing thermal histories and rapid solidification during laser melting. The dashed line-circumscribed areas in Figure 4A and C are magnified in Figure 4B and D, respectively; locations of EDS measurements are indicated. EDS spot analysis at different locations showed a slight variation in elemental composition, as evident in Table 3. Compared to the cellular substructure (spots 2 and 5), domain boundaries (spots 1 and 4) exhibit a notable decrease in Fe content and a corresponding increase in Cr, Mo, and Si levels. EDS spots 3 and 6 are dark regions within the microstructure. A comparative study on microstructure analysis of all printed samples showed a similar sub-cellular structure with minor chemical segregation.

3.3. Two-dimensional X-ray diffraction analysis

Figure 5A shows the four-frame rocking curve-stitched 2D-XRD patterns of S1 (Figure 5A-i) and S4 (Figure 5A-ii) samples, and Figure 5B depicts the 2θ integration plot of all printed samples. The 316L SS phase is distributed randomly, as evidenced by the arbitrary distribution of χ angles of the diffraction peaks at the specified 2θ locations. A singular austenitic face-centered cubic (FCC) phase is observed with no detection of foreign phase peaks. The crystallographic planes {111}, {200}, {220}, and {311} were

Table 2. Relative density and surface roughness of as-printed samples

Parameters	Samples					
	S1	S2	S3	S4	S5	S6
RD (%)	99.72±0.18	99.15±0.12	99.13±0.14	99.94±0.13	99.92±0.19	99.86±0.16
S_a (µm)	15.45±0.68	14.37±0.11	14.85±0.18	19.77±0.12	18.22±0.21	17.10±0.19

Abbreviations: RD: Relative density; S_a: Surface roughness

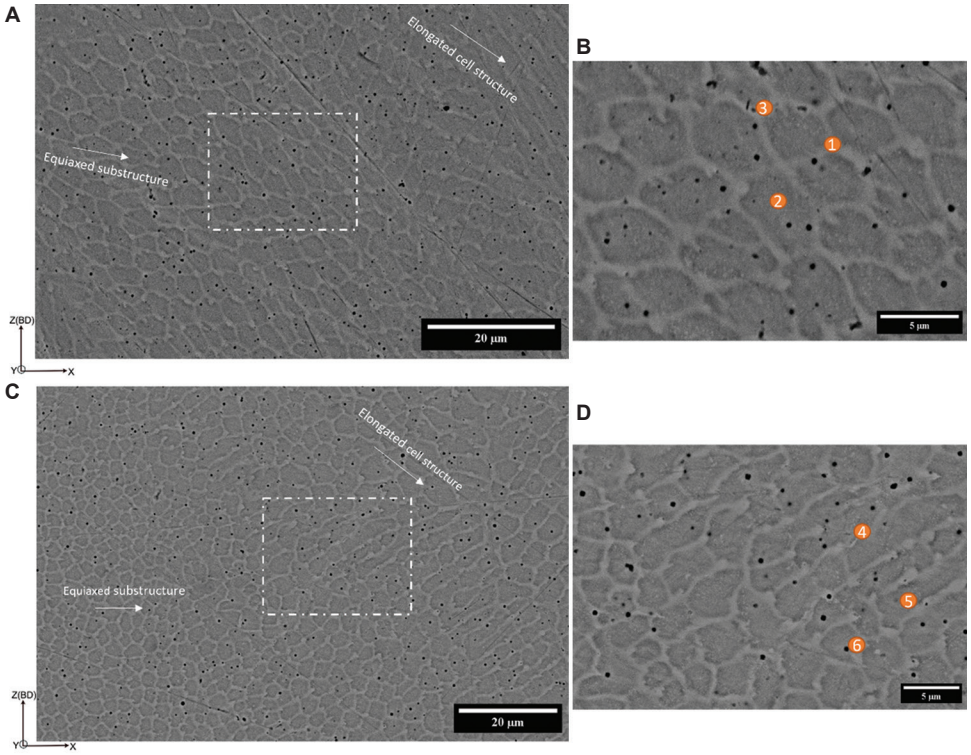

Figure 4. Scanning electron microscopy micrographs of S1 (A and B) and S4 (C and D) printed samples showing the presence of both elongated cell structure and equiaxed substructure along the build direction. Magnification: (A and C): ×1500; (B and D): ×5000.

Table 3. Energy dispersive X-ray spectroscopy spot analysis of the S1 and S4 samples

Spot no.	Elements (wt. %)					
	Fe	Cr	Ni	Mo	Si	Mn
1	60.2	20.3	14.3	2.5	2.2	0.6
2	64.8	18.4	13.7	0.4	1.3	1.3
3	62.7	18.2	11.0	1.8	3.2	3.2
4	65.0	17.4	14.1	1.9	0.9	0.8
5	64.5	19.6	12.2	2.1	0.7	0.9
6	64.7	18.5	13.2	2.2	0.8	0.6

identified at 2θ angles of 43.61°, 50.68°, 74.57°, and 90.50°, respectively. Using the Nelson–Riley and Williamson–Hall extrapolation methods, the lattice constants and micro-strains for S1 were determined to be 3.57 ± 0.003 Å and 3.61×10^{-3}, respectively, and the corresponding values for S4 were 3.59 ± 0.028 Å and 3.05×10^{-3}, respectively.

The pole figure of the {111} peak with a strong intensity at 2θ = 43.5° for various sections of the 316L metallic sample includes S1 bottom and top sections (Figure 6A and B) and S4 bottom and top sections (Figure 6C and D, respectively. The {111} peak texture of the S1 sample's top section (Figure 6B) displays a larger grain size, evident from a lower peak count and higher intensity, in contrast to the S1 bottom section (Figure 6A) where smaller grain size, higher grain count, and lower intensities are observed, consistent with findings by Pathak *et al.*[10] Comparable differences between the top and bottom sections are observed in Figure 6C and D for S4 sample. In addition, the top sections of S1 and S4 samples reveal multiple intense peaks, suggesting the presence of grain sizes larger than those in the bottom sections. The presence of intense peaks can be attributed to the processing conditions and cooling rates of the interlayer, whose temperature increases through the deposition.[10] Without preheating the substrate, the initial deposition of the print layer experiences a relatively lower temperature. As the build layers increase, heat accumulates, resulting in higher temperatures at the top section of the print samples. This may potentially lead to larger grain sizes at the top section than at the bottom section of the print samples.[10,29]

3.4. Internal defects analysis using X-ray micro-CT

X-ray computed tomography was employed for internal defects analysis of the printed samples before tensile testing. The reconstructed 3D images of the fracture sections of the S1 sample (Figure 7A) and the S4 sample (Figure 7B), with emphasis on the bulk part to highlight low-density internal

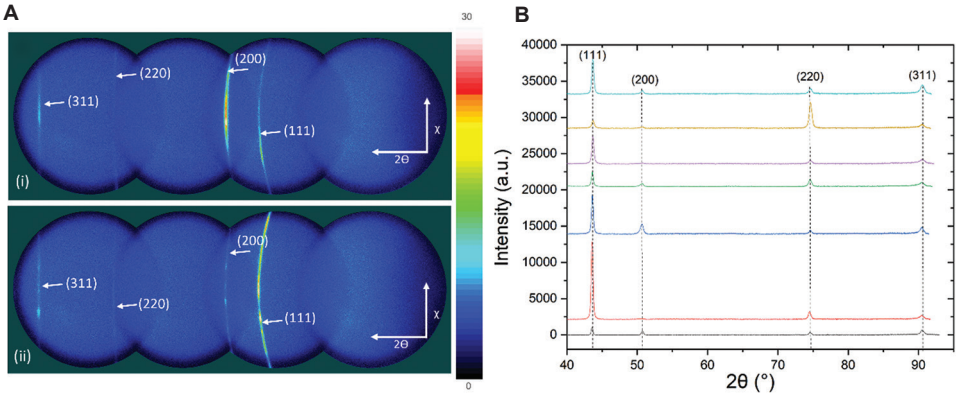

Figure 5. (A). Rocking curve 4-frame stitched two-dimensional X-ray diffraction patterns of 2θ versus χ (sample normal direction), (i) S1, (ii) S4; (B) Integrated 2θ versus intensity plot of 316 L SS powder and printed samples.

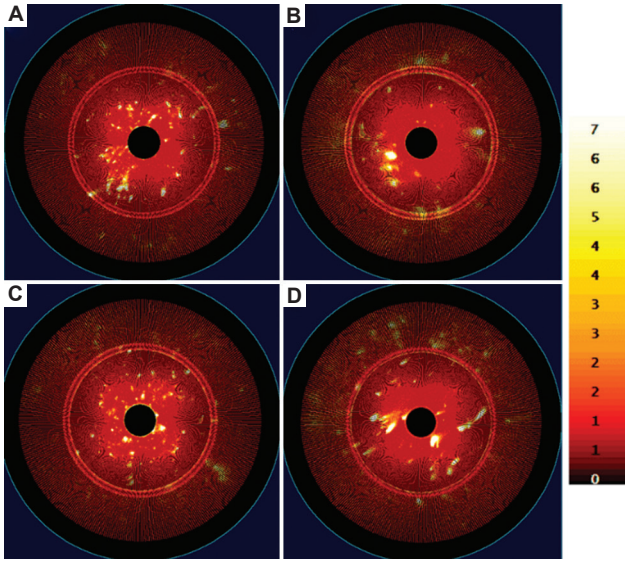

Figure 6. Pole figure of {111} peak at 2θ=43.5°. (A and B) S1 bottom and top sections, respectively; (C and D) S4 bottom and top sections, respectively.

defects, are presented. These images reveal the existence of two types of pores: gas-induced spherical pores and irregular-shaped lack-of-fusion pores. Pores induced by gas, commonly exhibiting a small spherical shape, arise from trapped gas within powder during vapor recoil keyhole laser melting.[30,31] In contrast, lack-of-fusion pores, characterized by irregular shapes, result from inadequate laser energy or suboptimal parameters, leading to the formation of a partially molten or unmolten powder melt pool.[31,32] Micro-cracks or inclusions (foreign elements) were not observed in any of the printed samples. It was observed that the number of pores formed at the initial print layers was slightly higher but decreased along the print build direction. One plausible explanation for this phenomenon is that during the deposition process when the initial powder metal pool of the print layer contacts the substrate, the disparity in temperature gradient between the print layer and substrate results in the scattering of some metal powder.[10,30] This, in turn, leads to the presence of unmelted particles in the initial print layers.

Table 4 provides information on the average porosity of the printed samples, where the entire gauge length of tensile specimens was considered to estimate the average pore fraction. In comparison to the unidirectional scan pattern (S1), the bidirectional scan (S4) exhibited a slightly higher porosity percentage. The variation in porosity for different dwell times between print layers was found to be minimal.

3.5. Mechanical properties analysis

3.5.1. Micro-hardness testing

The variation of average hardness and reduced elastic modulus (E*) of the printed samples is illustrated in Figure 8A. An average of 10 indents was performed in every sample to get a better accuracy. The unidirectional print sample (S1) showed a hardness and E* of 2.38 ± 0.058 GPa and 171.70 ± 2.94 GPa, respectively, whereas the bidirectional print sample (S4) exhibited the corresponding values of 2.22 ± 0.046 GPa and 168.65 GPa. The increase in dwell time between the print layers resulted in a declining trend of hardness and E* properties for both printed patterns, except for samples S1 and S2, as shown in Figure 8A.

3.5.2. Tensile test

The stress-strain plots of printed samples at room temperature are shown in Figure 8B. The unidirectional sample (S1) showed a yield strength (YS) of 360 MPa, ultimate tensile strength (TS) of 583 MPa, and elongation of 38.21%, whereas the same set of measurements, in the same order, for the bidirectional sample was 325 MPa

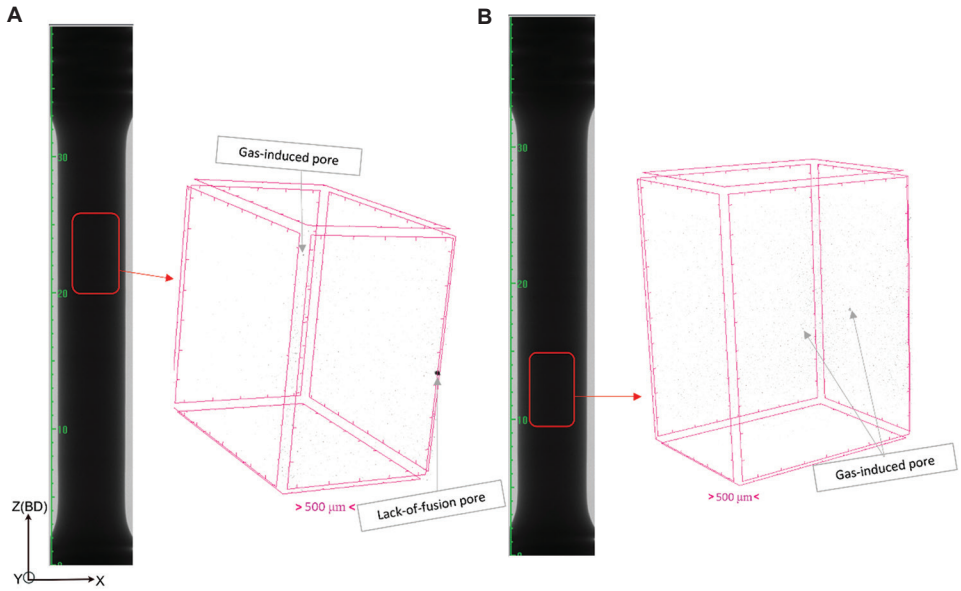

Figure 7. X-ray micro-computed tomography reconstructed 3D images of a fractured region of tensile test specimens, i.e., (A) S1 sample and (B) S4 sample, showing porosity distribution of tensile fractured gauge length region.

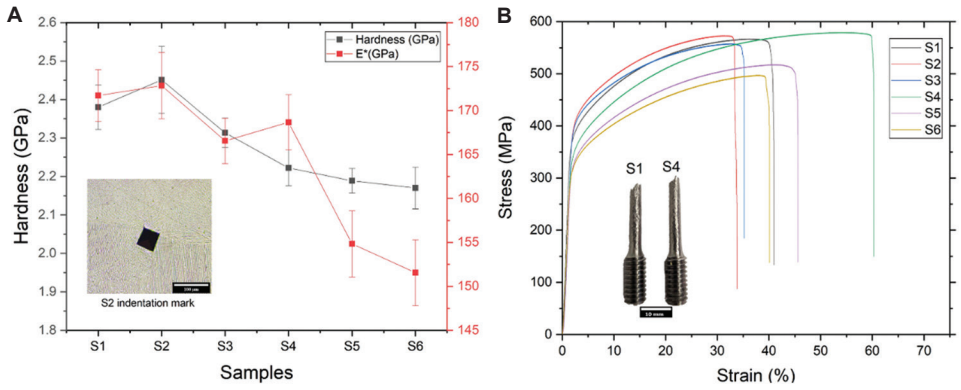

Figure 8. (A) Micro-hardness of printed samples; (B) stress-strain curve from tensile test.

Table 4. The average porosity of printed samples

Samples	Average porosity (%)					
	S1	S2	S3	S4	S5	S6
Average	0.12	0.15	0.27	0.29	0.33	0.49

(YS), 583 MPa (TS), and 50.27% (elongation) (Table 5). Compared to bidirectional printed samples, unidirectional printed samples showed a higher yield strength with a smaller elongation tradeoff. We observed that the ultimate tensile strength decreases with an increase in dwell time between print layers. However, such a trend was not found to be consistent with yield strength results.

A typical ductile facture of tensile specimens S1 and S4 is shown in Figure 9A and C, respectively. Higher-magnification SEM images of S1 and S4 samples are presented in Figure 9B and D, respectively. A typical dimple-featured microstructure showcasing minor voids, inclusion, and a small trace of unmelted region is also observed.

4. Discussion

4.1. Role of scan patterns on microstructure and properties

This study demonstrates the influence of customized scan patterns, specifically unidirectional and bidirectional printing, on the microstructure and corresponding properties of printed parts. It was observed that unidirectional printing introduces a higher content of elongated cellular and equiaxed grain structures,

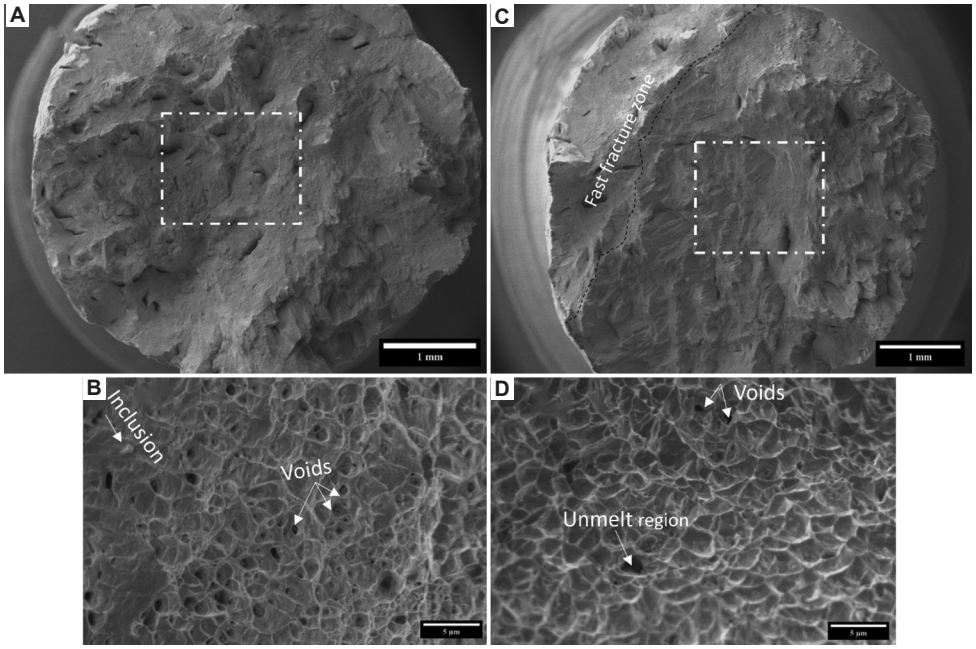

Figure 9. Scanning electron microscopy micrographs of tensile fractography section of S1 (unidirectional) sample (**A and B**) and S4 (bidirectional) sample (**C and D**). Magnification: (A and C): ×21; (B and D): ×3500.

Table 5. Tensile test results of printed samples

Samples	Yield strength (MPa)	Ultimate tensile strength (MPa)	Elongation (%)
S1	360	583	38.21
S2	379	579	30.39
S3	367	562	32.00
S4	325	583	50.27
S5	295	521	38.56
S6	320	501	33.26

whereas bidirectional printing results in a more uniform microstructure. The consistent toolpath in unidirectional printing, without abrupt changes in direction,[17] likely contributes to slightly lower surface roughness (S_a) compared to bidirectional printed samples, as characterized in Table 2. Unidirectional printed specimens also show lower porosity, owing to better control over the layering process and enhanced fusion between successive layers. This reduction in porosity in unidirectional prints minimizes the risk of voids or porosity in the deposition direction.

The lower porosity in unidirectional printed specimens has a notable influence on the mechanical properties, resulting in slightly improved tensile properties and hardness, as outlined in Table 4. These findings underscore the importance of customized scan patterns in tailoring microstructural features and properties of parts fabricated by metal AM.

4.2. Effect of dwell time between layers on print properties

The LENS-based DED AM process facilitates controlling the inter-layer print duration "dwell time" that can aid in controlling thermal gradient and inter-layer cooling rate.

Longer dwell time between successive print layers results in a higher cooling rate and a low-temperature gradient, which contribute to the production of a finer microstructure with relatively lower S_a, as evidenced by the numerical depiction of surface roughness of a series of specimens given in Table 2. Despite achieving a finer microstructure, the tradeoff is that the increase in dwell time and increased porosity, *i.e.*, lack-of-fusion (Table 4), likely yielded inferior mechanical properties shown in Table 5. In contrast to the findings by Denlinger *et al.*,[21] we did not observe any major distortion on printed specimens upon increasing the interlayer dwell time.

5. Conclusion

The role of customized scan pattern and interlayer dwell time on the microstructure and properties of 316L SS fabricated using a LENS-based DED process was investigated in this study. The resulting product after the DED process was a heterogeneous microstructure consisting of both columnar and equiaxed cellular substructure with minor inter-grain chemical segregation. Two-dimensional XRD results confirmed the presence of a

single-phase γ-austenitic FCC phase without any δ-ferrite phase. A more uniform microstructure was observed with a bidirectional scan pattern and an increase in interlayer dwell time. Internal defect analysis using computed tomography revealed a slightly higher lack-of-fusion porosity in specimens prepared with bidirectional scan patterns, and this porosity increased with longer interlayer dwell times. Despite the finer microstructure achieved with bidirectional scan patterns and extended interlayer dwell times, a slight deterioration in mechanical properties was observed due to the higher degree of porosity. This highlights a tradeoff between achieving a uniform microstructure and maintaining mechanical integrity, emphasizing the importance of optimizing scan patterns and interlayer dwell times for desired material properties in parts made by AM.

Acknowledgments

The authors would like to acknowledge the University of Houston Division of Research High Priority Area Research Large Equipment Grant I0503304 for establishing a state-of-the-art 2D-XRD facility used in this study.

Funding

This research received no specific grant from any funding agency.

Conflict of interest

The authors declare that they have no known competing financial interests or personal relationships that could have appeared to influence the work reported in this paper.

Author contributions

Conceptualization: Puskar Pathak
Data curation: Puskar Pathak, Goran Majkic
Methodology: Puskar Pathak
Supervision: Venkat Selvamanickam
Writing – original draft: Puskar Pathak
Writing – review & editing: Goran Majkic, Venkat Selvamanickam

Ethics approval and consent to participate

Not applicable.

Consent for publication

Not applicable.

Availability of data

Data are available from the corresponding author upon reasonable request.

Further disclosure

A part of this research work was presented at the International Conference of Advanced Manufacturing (ICAM), 2023, ASTM, Washington D.C.

References

1. Frazier WE. Metal additive manufacturing: A review. *J Mater Eng Perform*. 2014;23(6):1917-1928.

   doi: 10.1007/s11665-014-0958-z

2. DebRoy T, Wei HL, Zuback JS, *et al*. Additive manufacturing of metallic components -process, structure and properties. *Prog Mater Sci*. 2018;92:112-224.

   doi: 10.1016/j.pmatsci.2017.10.001

3. Sames WJ, List FA, Pannala S, Dehoff RR, Babu SS. The metallurgy and processing science of metal additive manufacturing. *Int Mater Rev*. 2016;61(5):315-360.

   doi: 10.1080/09506608.2015.1116649

4. Zhai X, Jin L, Jiang J. A survey of additive manufacturing reviews. *Mater Sci Addit Manuf*. 2022;1(4):21.

   doi: 10.18063/msam.v1i4.21

5. Turgut B, Gürol U, Onler R. Effect of interlayer dwell time on output quality in wire arc additive manufacturing of low carbon low alloy steel components. *Int J Adv Manuf Technol*. 2023;126(11-12):5277-5288.

   doi: 10.1007/s00170-023-11481-3

6. D'Andrea D. Additive manufacturing of AISI 316L stainless steel: A review. *Metals (Basel)*. 2023;13(8):1370.

   doi: 10.3390/met13081370

7. Thompson SM, Bian L, Shamsaei N, Yadollahi A. An overview of direct laser deposition for additive manufacturing; Part I: Transport phenomena, modeling and diagnostics. *Addit Manuf*. 2015;8:36-62.

   doi: 10.1016/j.addma.2015.07.001

8. Balhara H, Botcha B, Wolff SJ, Bukkapatnam STS. Ripple formations determine the heterogeneous microstructure of directed energy deposition (DED)-printed 316L components. *Mater Des*. 2023;227:2023.

   doi: 10.1016/j.matdes.2023.111756

9. Izadi M, Farzaneh A, Mohammed M, Gibson I, Rolfe B. A review of laser engineered net shaping (LENS) build and process parameters of metallic parts. *Rapid Prototyp J*. 2020;26(6):1059-1078.

   doi: 10.1108/RPJ-04-2018-0088

10. Pathak P, Majkic G, Erickson T, Chen T, Selvamanickam V. Two-dimensional X-ray diffraction (2D-XRD) and micro-computed tomography (micro-CT) characterization of additively manufactured 316L stainless steel. Available at SSRN 4529173 (2023).

doi: 10.2139/ssrn.4529173

11. Veiga F, Arizmendi M, Suarez A, Bilbao J, Uralde V. Different path strategies for directed energy deposition of crossing intersections from stainless steel SS316L-Si. *J Manuf Processes*. 2022;84:953-964.

doi: 10.1016/j.jmapro.2022.10.039

12. Amar E, Popov V, Sharma VM, Andreev Batat S, Halperin D, Eliaz N. Response surface methodology (RSM) approach for optimizing the processing parameters of 316L SS in directed energy deposition. *Materials (Basel)*. 2023;16(23):7253.

doi: 10.3390/ma16237253

13. Izadi M, Farzaneh A, Gibson I, Rolfe B. The Effect of Process Parameters and Mechanical Properties of Direct Energy Deposited Stainless Steel 316. In: *Solid Freeform Fabrication 2017: Proceedings of the 28th Annual International Solid Freeform Fabrication Symposium-an Additive Manufacturing Conference*; 2020. p. 1058-1067.

14. Kuzminova YO, Firsov DG, Konev SD, *et al*. Structure control of 316L stainless steel through an additive manufacturing. *Lett Mater*. 2019;9(4):551-555.

doi: 10.22226/2410-3535-2019-4-551-555

15. Karlapudy SP, Nancharaiah T, Rao VVS. Influence of different build orientation and laser scan strategies on surface quality, mechanical and material characteristics of 18 Ni-300 maraging steel processed through DMLS. *Aust J Mech Eng*. 2021;21(4):1381-1395.

doi: 10.1080/14484846.2021.2007620

16. Liu M, Kumar A, Bukkapatnam S, Kuttolamadom M. A review of the anomalies in directed energy deposition (DED) processes and potential solutions-part quality and defects. *Procedia Manuf*. 2021;53:507-518.

doi: 10.1016/j.promfg.2021.06.093

17. Ribeiro KSB, Mariani FE, Coelho RT. A study of different deposition strategies in direct energy deposition (DED) processes. *Procedia Manuf*. 2020;48:663-670.

doi: 10.1016/j.promfg.2020.05.158

18. Yadollahi A, Shamsaei N, Thompson SM, Seely DW. Effects of process time interval and heat treatment on the mechanical and microstructural properties of direct laser deposited 316L stainless steel. *Mater Sci Eng A*. 2015;644:171-183.

doi: 10.1016/j.msea.2015.07.056

19. Sciammarella FM, Najafabadi BS. Processing parameter doe for 316l using directed energy deposition. *J Manuf Mater Process*. 2018;2(3):61.

doi: 10.3390/jmmp2030061

20. Mohr G, Altenburg SJ, Hilgenberg K. Effects of inter layer time and build height on resulting properties of 316L stainless steel processed by laser powder bed fusion. *Addit Manuf*. 2020;32:101080.

doi: 10.1016/j.addma.2020.101080

21. Denlinger ER, Heigel JC, Michaleris P, Palmer TA. Effect of inter-layer dwell time on distortion and residual stress in additive manufacturing of titanium and nickel alloys. *J Mater Process Technol*. 2015;215:123-131.

doi: 10.1016/j.jmatprotec.2014.07.030

22. ASTM. *Standard Guide for Additive Manufacturing of Metal-Finished Part Properties-Methods for Relative Density Measurement 1*. Vol. 1. United States: ASTM; 2023. p. 1-6.

doi: 10.1520/F3637-23.2

23. He BB, Preckwinkel U, Smith KL. Stress and texture analysis with two-dimensional x-ray diffraction. *Mater Sci Forum*. 2002;404-407:109-114.

doi: 10.4028/www.scientific.net/msf.404-407.109

24. Rupert AN, McCausland PJ, Flemming RL. Ordinary chondrite shock stage quantification using *in situ* 2-D X-ray diffraction of olivine. *Meteorit Planet Sci*. 2020;55(10):2224-2240.

doi: 10.1111/maps.13572

25. Dzhurinskiy D, Babu A, Pathak P, Elkin A, Dautov S, Shornikov P. Microstructure and wear properties of atmospheric plasma-sprayed Cr3C2-NiCr composite coatings. *Surf Coatings Technol*. 2021;428:127904.

doi: 10.1016/j.surfcoat.2021.127904

26. Lama A, Sarvesha R, Garcia D, *et al*. Macroscale property assessment and indentation characteristics of thick section friction stir welded AL 5083. *Mater Sci Eng A*. 2023;880:145306.

doi: 10.1016/j.msea.2023.145306

27. Thompson A, Maskery I, Leach RK. X-ray computed tomography for additive manufacturing: A review. *Meas Sci Technol*. 2016;27(7):072001.

doi: 10.1088/0957-0233/27/7/072001

28. Zheng B, Haley JC, Yang N, *et al*. On the evolution of microstructure and defect control in 316L SS components fabricated via directed energy deposition. *Mater Sci Eng A*. 2019;764:138243.

doi: 10.1016/j.msea.2019.138243

29. Suwas S, Vikram RJ. Texture evolution in metallic materials during additive manufacturing: A review. *Trans Indian Natl Acad Eng*. 2021;6(4):991-1003.

doi: 10.1007/s41403-021-00271-6

30. Kim FH, Moylan SP. Literature review of metal additive

manufacturing defects. In: *NIST Advanced Manufacturing Series*. Gaithersburg, MD: National Institute of Standards and Technology; 2018. p. 1-17. Available from: https://nvlpubs.nist.gov/nistpubs/ams/NIST.AMS.100-16.pdf [Last accessed on 2018 May 01]

31. Kruth JP, Bartscher M, Carmignato S, Schmitt R, De Chiffre L, Weckenmann A. Computed tomography for dimensional metrology. *CIRP Ann*. 2011;60(2):821-842.

doi: 10.1016/j.cirp.2011.05.006

32. Shah P, Racasan R, Bills P. Comparison of different additive manufacturing methods using computed tomography. *Case Stud Nondestruct Test Eval*. 2016;6:69-78.

doi: 10.1016/j.csndt.2016.05.008

ACCSCIENCE PUBLISHING

Materials Science in Additive Manufacturing

ORIGINAL RESEARCH ARTICLE

Using agglomerate-free nanopowder as sliding friction reducer between alumina platelets in an ultraviolet-curable slurry for vat polymerization additive manufacturing

Ming Xuan Gan[1]*, Lijie Zhang[1,2], Guanjin Li[1], Tao Li[3], Beng Wah Chua[3], and Jiansheng Liu[2]

[1]Department of Mechanical Engineering, National University of Singapore, Singapore

[2]Department of Mechanical Engineering, School of Advanced Manufacturing, Nanchang University, Nanchang, Jiangxi, China

[3]Singapore Institute of Manufacturing Technology, Agency for Science, Technology and Research (A*STAR), Singapore

Abstract

Nature's ability to adapt and survive the harshest environment offers humankind an important source of muses in the efforts to create and improve existing materials. In this study, we demonstrated a concept of using agglomerate-free nanopowder as a sliding friction reducer between alumina platelets in a slurry. An ultraviolet-curable slurry containing predominantly alumina platelets exhibited favorable rheological characteristics to align the platelets with a coating blade in a vat polymerization printer. Consequently, a ceramic part with nacre-like structure could be printed and infiltrated with a secondary phase. Microscopy study on the fracture surfaces revealed various toughening mechanisms such as severing of the bridges between platelets and crack deflection by the platelets. Fracture of a three-point bent part mainly occurred due to the pull-out of platelets and failure of the polymer phase. The findings of this study suggest promising avenues for future research, including the additive manufacturing of larger objects consisting of nacre-like microstructures.

Keywords: Alumina; Platelets; Nacre-inspired; Vat polymerization; Ceramics

***Corresponding author:**
Ming Xuan Gan
(mxgan@nus.edu.sg)

Citation: Gan MX, Zhang L, Li G, *et al.* Using agglomerate-free nanopowder as sliding friction reducer between alumina platelets in an ultraviolet-curable slurry for vat polymerization additive manufacturing. *Mater Sci Add Manuf.* 2024;3(1):2711. doi: 10.36922/msam.2711

Received: January 11, 2024

Accepted: February 19, 2024

Published Online: March 14, 2024

1. Introduction

Nature's resiliency to always find its way to evolve and adapt to the environment to overcome challenges is inspiring to humankind. For instance, hierarchical structures that form microscopically and naturally in organisms often possess exceptional mechanical properties. Such fascinating constructions that happen naturally, yet are difficult to replicate, have motivated humankind to research on their intricacies with the hopes of creating stronger and tougher man-made structural materials.[1-4] One of such notable examples is nacre. Nacre, found in shells of mollusks, is distinguished by the organized brick-and-mortar arrangement of aragonite platelets (95 vol.%) and organic lamellae (5 vol.%).[5] This particular architecture of platelets and organic layer imparted impressive strength and ductility through energy redistribution made possible by

limited deformation induced by various mechanisms such as breaking of mineral bridges, inhibited sliding by nano-asperities, and bonding between the two phases.[6,7] These mechanisms were established to be the main reasons that crack deflection occurred during crack propagation, which dissipated energy to toughen the shell. Such exceptional properties of nacre have encouraged many studies and efforts to synthesize materials (from one-dimensional to three-dimensional [3D]) with microstructures replicating that of a nacre.[8]

Additive manufacturing comprises technologies that enable the freeform fabrication of various materials, such as metals and plastics, into 3D objects, overcoming design and manufacturing constraints caused by geometrical complexities faced in conventional manufacturing. However, the direct additive manufacturing of ceramics remains a challenge due to the inherent properties of ceramics, such as brittleness and high melting temperatures.[9,10] As such, indirect additive manufacturing, such as binder jetting, direct ink writing, and vat polymerization, are the most common methods used to fabricate ceramic parts at present. For instance, we can infuse a solvent such as ultraviolet (UV)-curable resin with ceramic filler to create a ceramic slurry before curing it with a suitable light to obtain a 3D part.[11] The printed part is then subjected to debinding and sintering in a furnace to finally obtain a ceramic part. However, such a process is not without its issues. Infusing a resin with ceramic filler often results in the thickening of the slurry and increasing the viscosity.[12,13] This increased viscosity complicates the process as the slurry resists to flow during the printing process, unless a coating system is used in the printer. As a result, the amount of ceramic filler that can be used is limited which also results in shrinkages after sintering.

Nevertheless, additive manufacturing is still an adequate method for fabricating ceramic parts, especially for nature-inspired structures. By capitalizing on the advantages of a suitable additive manufacturing process, nature-inspired structures such as nacre can be mimicked. A study that closely exemplifies the mimicking of nature-inspired structures has been reported, investigating the effect of alumina platelets on the rheological properties of a ceramic slurry.[14] However, this study prepared relatively low platelets to the nanopowder ratio in the slurry to print a nacre-mimicking structure. Furthermore, shear thinning in such a case is expected as the slurry contains a higher proportion of regular-shaped nanoparticles. Another study used boron nitride platelets to prepare a slurry, which exhibited relatively high viscosity to 3D-print a nacre-inspired structure.[15] However, a pre-sintering test revealed that the mechanical properties were largely reliant on the polymer phase. In another study, four-dimensional (4D) printing of alumina platelets was accomplished with direct ink writing method.[16] The resultant alumina platelets, comprising a high platelet content of 95 wt.%, exhibited excellent mechanical properties and thermal properties.

In the present study, we investigated the concept of using alumina powder (nano- to micron-sized) to achieve various characteristics observed in a nacre. The first objective was to reduce the viscosity of a slurry containing alumina platelets to additively manufacture nacre-inspired structures. This concept explored the use of powders of different morphologies added into the slurry to separate and act as wheels to reduce sliding friction between the platelets when a shearing force is applied on the slurry during the coating phase of a vat polymerization printing process. The second objective involved determining a suitable sintering temperature to promote the formation of bridges to mimic the mineral bridges present in a nacre. Furthermore, the powder was added to create spaces between the platelets such that a secondary phase can be infiltrated, in essence, to mimic the organic phase of a nacre. Last but not least, we aimed to prepare a UV-curable slurry with an appropriate platelet-to-powder ratio, based on the best result composition, suitable for vat polymerization. To align the platelets such that they replicate the microstructure of a nacre, we used a vat polymerization printer equipped with a coating blade to spread material to every layer.

2. Materials and methods

In this study, four types of slurry were prepared. Of the four, three slurries contain the alumina platelets and an alumina powder obtained from either Taimei (100 nm, regular and agglomerate-free nanopowder [NS]), NLM (1 μm, regular micron-sized powder [MR]), and Sigma (10 μm, irregular micron-sized powder [MI]) and one contains purely the platelets. Figure 1A–D depicts the size and morphology of the powders used in this study. The alumina platelets (purity ≥ 99%; White Sapphire RonaFlair®, Merck KGaA, Germany) were obtained from Sigma Aldrich and had a particle size (d50) of approximately 10.5 μm. The effects of these powders were then compared by characterizing the rheological properties of the slurry. Each slurry contains alumina platelets (PL) and one type of powder (NS or MR or MI) in a ratio of 3:1. In addition, 1 wt.% of dispersant and 0.3 wt.% of photo-initiator were added to reduce the viscosity and make the slurry UV-curable, respectively.

The preparation of each slurry begins with dissolving the dispersant in the photo-monomer HDDA. Afterward, the powders (NS, MI, and MR) were each added and

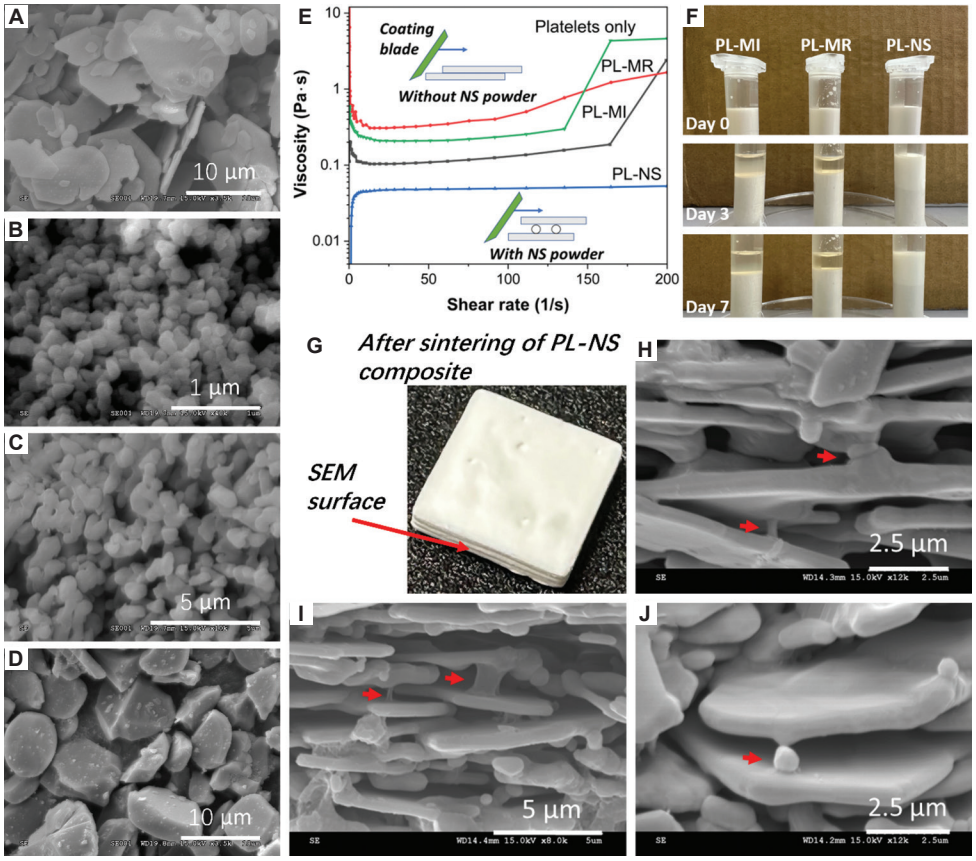

Figure 1. Initial study on the effects of powder type on platelet slurry properties. (A–D) Scanning electron microscope (SEM) images of alumina platelets (PL), nanopowder (NS), regular micron-sized powder (MR), and irregular micron-sized powder (MI). (E) The viscosity of each slurry. (F) Sedimentation behavior of the slurry containing platelets with NS, MI, or MR. (H–J) SEM images of the sintered sample in (G).

dispersed. Alumina platelets were subsequently added and mixed to obtain a 35 vol.% slurry. The proportion of each additive was measured based on the total solid loading of 35 vol.% in this study. Photo-initiator was added last and before fabrication to prevent premature curing of the slurry. All of the mixing steps were carried out on a planetary mixer at 2000 rpm for 5 min each. As a result, the total time needed to prepare the slurry takes <40 min.

Additive manufacturing of this composite was conducted on a vat polymerization system (Cerafab 8500, Lithoz, Austria). The printer equipped with a coating blade provided additional aid to align the platelets in an orientation that mimics the nacre structure. The wavelength of the projector is approximately 450 nm, and the build volume of the printer is 115 mm × 64 mm × 200 mm.

ImageJ was used to measure the particle sizes. Rheological properties were characterized by measuring the viscosity and observing the stability of the slurry over 7 days. The viscosity of each slurry was measured on a rheometer (HAAKE Mars III) with a parallel plate set-up of a gap of 0.4 mm from shear rates of 0 – 200 s^{-1} at an ambient temperature of 25°C. Each slurry was prepared and left untouched over a period of 7 days to observe the sedimentation of the powder.

The porosity (P) of sintered ceramic samples was calculated by:

$$p = 1 - \frac{\rho}{\rho_s} \quad \text{(I)}$$

Where ρ is the density of samples, and ρ_s is the density of alumina (3.97 g/cm^3). Three-point bending test was performed on an Instron 8874 system (Instron®, US). The support span for the test setup was 40 mm, and the sample was loaded at a rate of 0.1 mm/min until failure. The fracture surface was then examined under a scanning electron microscope (SEM; Hitachi S-4300, Hitachi High-Tech Corporation, Japan) after gold coating at 20 mA for 60 seconds.

3. Results

Figure 1A–D shows the morphologies of alumina platelets and different alumina powders. Examination of these images revealed that the alumina platelets possess an average diameter of 8.19 ± 2.50 μm and a thickness of 0.53 ± 0.12 μm. The nanopowder possessed a significantly smaller mean diameter of 0.45 ± 0.02 μm but was comparable to the thickness of alumina plates. Furthermore, the diameters of MR and MI were measured at 1.09 ± 0.93 μm and 7.36 ± 1.51 μm, respectively. An initial study conducted to examine the characteristics of the three types of slurry showed that the agglomerate-free nanopowder NS effectively reduces and stabilizes the viscosity of the slurry to around 0.045 Pa·s even at high shear rates of up to 200 /s (Figure 1E). The other slurries containing the other two types of powder and without containing any exhibited a shear thickening behavior at high shear rates.

This shear thickening behavior of a slurry under high shear rates is undesirable in a vat polymerization AM system, which uses a coating system. During the coating phase, the blade moves in at an angle to spread the slurry, as illustrated in Figure 1E. This angle of attack pushes the slurry forward and downward, generating a shearing stress between the platelets. The resulting shear thickening behavior at high shear rates implies that the printing process would be slower due to the slower coating speed required. Furthermore, at a higher shear rate, the slurry experiences greater resistance to flow as it hardens. This recorded behavior resembles that of a non-Newtonian cornstarch-water mixture under stress. The addition of the NS powder also showed better stability of the slurry as compared to the other two. In contrast, the powder in the other two slurries settled relatively quickly by day 3, as shown in Figure 1F. Based on these prior results, we fabricated and sintered a simple sample (Figure 1G) with the alumina platelet (PL)-NS slurry to inspect the microstructure and the orientation of the platelets. As shown in Figure 1H–J, the alignment of the platelets can clearly be seen under the SEM. Furthermore, the images also revealed that the nanoparticles formed bridges, which contribute as a toughening mechanism, between the platelets on sintering. The long-range forces generated by van der Waals interactions are universal and always attract particles of the same kind to each other.[17] By creating a bridge effect between the platelets, the addition of NS powder can successfully lower the van der Waals forces between them, causing a drop in viscosity. This suggests that the NS powder is not only primed for reducing the viscosity effectively and ensuring the alignment of the platelets by preventing the shear thickening of the slurry when subjected to shearing stress by the coating blade but also facilitating the formation of bridges between the platelets.

As shown in Figure 2A–C, the SEM images also revealed that the NS particles did occupy the space between the platelets to provide a form of wheeling mechanism for the platelets to slide over when stress is applied. When subjected to high shearing stress during the coating phase, the platelets slide over the nanoparticles in a way similar to large and heavy objects being moved on wheels or rollers by humans in ancient times. Without these nanoparticles, the platelets would be forced to slide against one another, generating friction that prevented the slurry from flowing fluidly, as observed in the other two slurries. This mechanism, made possible by the addition of the nanopowder, allowed the slurry to inhibit shear thickening under high shearing rates and ensured the alignment of the platelets during the coating phase of printing.

As shown in Figure 2A and 2C, at sintering temperatures of 1300°C and 1400°C, the nanopowder remained relatively small at approximately 100 nm. As the temperature increased to 1500°C and above, the nanopowder and platelets could be seen to have undergone growth, and bridges began to form between the enlarged platelets at 1600°C (Figure 2D and E). In all the samples, the pore sizes did not seem to differ much, except that they became smaller when sintered at 1600°C. This is due to the growth in size of the platelets and nanopowder, which leads to a reduction of the pore size. Moreover, sintering at 1600°C promoted the formation of bridges by the nanopowder between the platelets. The bridge between plates can dissipate energy through breakage, thereby enhancing toughness. This mechanism is similar to the toughening mechanism in nacre.[18]

After sintering at 1600°C, the porosity of ceramic parts was 0.34 ± 0.02. The sintered parts were then subsequently infiltrated with UV-curable HDDA in a vacuum chamber at negative pressure for 24 h and sheltered from lights. The degree of infiltration relative to the sintering temperature was then examined at the cross-section under SEM. SEM images (Figure 2A–H) show that the UV-curable HDDA could be infiltrated and cured, regardless of the temperature, the samples were sintered. This is most likely due to the gaps between the platelets created by the nanopowder, which obstructed the sintering of the platelets to one another. The gaps may also offer an explanation about the similarity in pore sizes, which indicates that we can sinter at 1600°C to create a stronger (due to bridges formed) yet porous part while allowing the infiltration of a second phase. This also suggests that, in addition to the mechanical properties imparted from the infiltrated second phase, the toughness

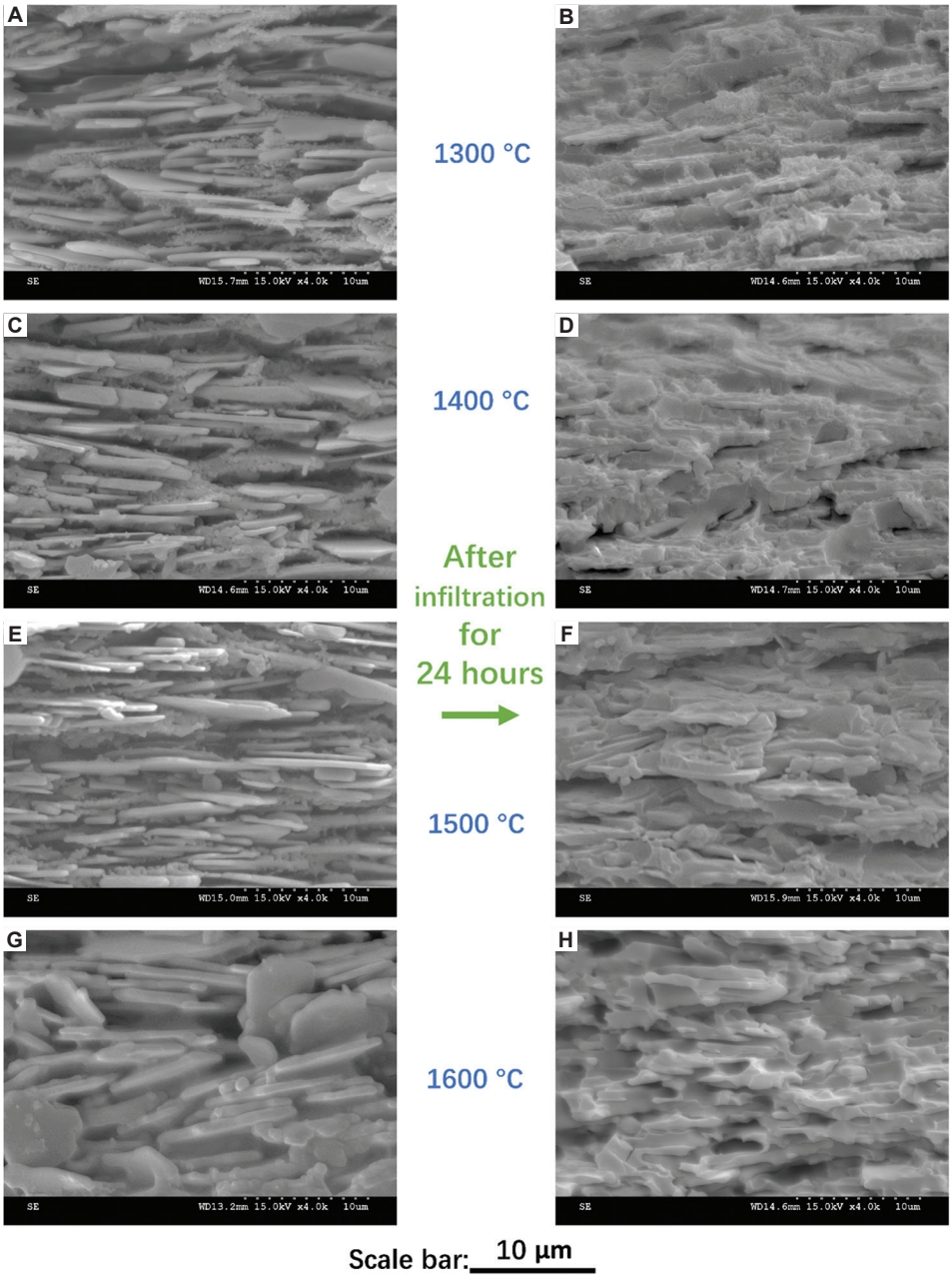

Figure 2. (A–H) Influence of sintering temperature on pore sizes and the extent of infiltrating a secondary polymeric phase. Scale bar applies to all panel images.

of this composite could also be improved by promoting the formation of bridges between the platelets, which contribute to the toughening mechanism.

Furthermore, the nanopowder that did not form the bridges can also induce inelastic shearing resistance like another toughening mechanism of the nacre, which is enabled by the presence of nanoasperities.[8] These characteristics of synthetic nacre-like structures have never been reported in other studies on the fabrication of nacre-inspired bulk 3D structures, as most of them focused on creating an aligned platelet structure through various methods.

Based on the initial study, we additively manufactured samples in the same way as described above for three-point bending tests.

Figure 3 illustrates the whole process from additive manufacturing of the alumina platelet samples to the infiltration of a secondary phase. The layer thickness of

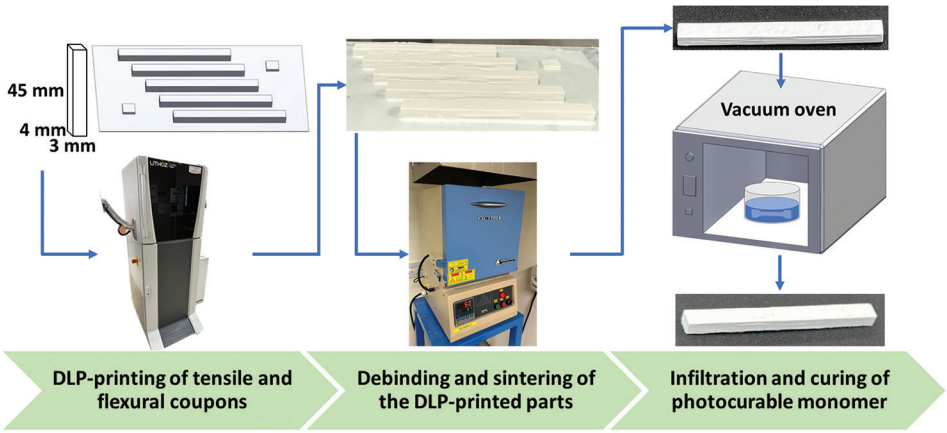

Figure 3. Fabrication process of the nacre-inspired samples for the three-point bending test.

each print was 100 µm. The dimensions of the samples for bending test measure 45 mm × 3 mm × 4 mm. In the second part of this study, we sintered the samples at 1600°C before infiltration.

Figure 4A illustrates a simple three-point bending test with the applied load perpendicular to the aligned platelets until failure. The flexural stress and strain (Figure 4B) were then calculated from the applied load and displacement with Equations II and III, respectively.

$$s = \frac{3FL}{2bd^2} \quad \text{(II)}$$

$$\varepsilon = \frac{6Dd}{L^2} \quad \text{(III)}$$

Observations from the composite (Figure 4C) under the SEM revealed several types of defects that contributed to the failure of the sample, as depicted in Figure 4D–F. The majority of these defects included platelets pull-out, platelets peeled away from the polymer phase, and severed bridges that formed from the sintering of the nanoparticles. The absence of fractured platelets suggests that only the platelet-polymer interface and bridges sustained the load, which contributed to the flexural strength of the composite. However, since the flexural strength of the HDDA was reported to be approximately 20 MPa, the calculated stress of more than 50 MPa suggested that there are other toughening mechanisms.[19] For instance, in addition to the energy dissipation from the fracturing of the bridges, cracks from the polymer phase could be seen deflected by the platelets in Figure 4F, which prevented crack propagation directly through the sample. According to the bending tests, the fabrication of this composite based on the above-described additive manufacturing method yielded a strength lower than expected. We consider a couple of factors that may have contributed to the low flexural strength.

First, the sintering temperature at 1600°C did not fully densify the printed part, which resulted in poor or little bonding between the alumina platelets and nanoparticles. Moreover, the presence of nanoparticles between the platelets also prevented a full densification of the printed part. Furthermore, obtaining a fully dense part would likely restrict the infiltration of a secondary phase. Nevertheless, sintering at a higher temperature or reducing the amount of nanopowder may improve the flexural strength of the part due to greater mass diffusion and, hence, sintering of the powders.

The second reason for the low strength is due to the type of polymer used for the secondary phase. Aside from the weaker mechanical properties of HDDA, we suspect that the weak interfacial bonding between the alumina phase and the polymer phase led to the peeling of the platelets. This failure mode is shown in Figure 4D and F. In general, the interface damage mechanism is governed by the attraction forces to polymer chains from the alumina phase 19. When compared to the polymer phase, these attraction forces from the alumina phase to the polymer chains are found to be weaker. Therefore, this weak interfacial bonding possibly served as a preferential manner of energy dissipation and failure when loaded despite there being no obvious defects at the interface, as shown in Figure 2F.

The last probable cause of the weak composite is attributed to the defects from additive manufacturing, such as delamination between layers. The delamination between layers would create huge pores in the part after sintering, which would then be filled with the polymer, as depicted in Figure 4G. This resulted in a composite consisting more of a weaker polymer, hence lowering the strength. Furthermore, the greater surface contact area between the polymer and ceramic phase as a result of this defect also offered a preferential location for failure, such as peeling of the

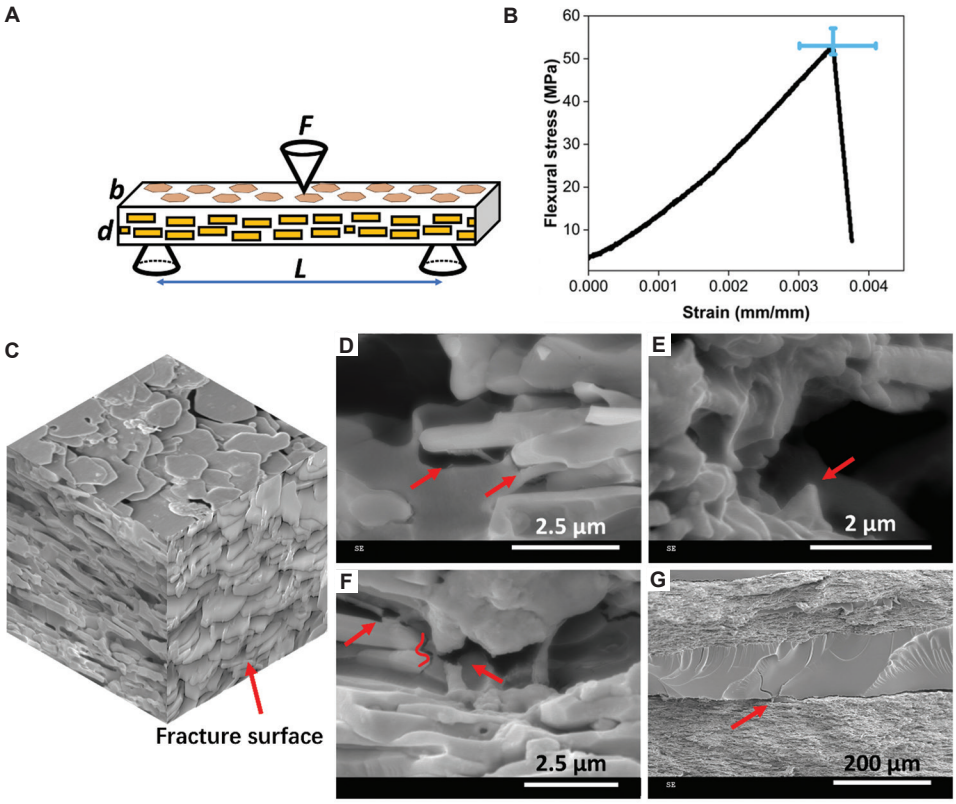

Figure 4. (A) Set-up of three-point bending test and the representation of measurements used to calculate flexural stress and strain. (B) Flexural stress of the composite plotted against strain. (C) 3D image of the composite. (D–G) Various defects found at the fracture surface, such as peeling of platelets off the polymer, platelets pull-out, and breakage of the bridges.

ceramic phase due to poor interfacial bonding since there is no contact between the platelets on the opposite surfaces. Therefore, the strength in such a region relies heavily on the properties of a polymer, as there are no toughening mechanisms imparted by the alumina platelets available.

4. Discussion

Naturally occurring construction of stronger materials from different weaker constituents is an aspect we can learn from to synthesize new stronger materials. For instance, despite the high brittle content in a nacre, a 5 vol.% of organic phase is sufficient to improve the overall properties by several magnitude. In this study, we demonstrated the process from slurry preparation to additive manufacturing and created a nacre-inspired structure using the vat polymerization technology. This was made possible due to the wheel effect achieved by the addition of nanopowder, which thereby improves the rheological properties. Furthermore, the spaces created between the platelets due to the inclusion of the nanopowder allowed infiltration of a secondary phase despite sintering at 1600°C.

Despite the lower-than-expected flexural strength of the composite, we demonstrated in this study a method to additively manufacture a nacre-like structure with a slurry that predominantly contains alumina platelets. On overcoming the undesirable rheological properties with the addition of nanopowder, the slurry could be coated with a blade, which is essential to align the platelets to replicate the nacre structure. Furthermore, the slurry preparation process takes less than an hour to complete.

5. Conclusion

This study offers a method capable of producing products consisting of nacre-like structures on a vat polymerization system by virtue of the greater resolution it affords to the products and the geometrical conformance of the products to the intended design. Nevertheless, improvements to the mechanical properties of this composite are warranted in future research.

Acknowledgment

None.

Funding

This research is partially supported by the Advanced Research and Technology Innovation Centre (ARTIC), the National University of Singapore under Grant (project number: A-0005947-31-00), and is supported by A*STAR under its IAF PP Grant (Project No. M22K4a0044) under the work package of "Thermal Management of Motor with Ferrofluid Composite Particles," and the Natural Science Foundation of Jiangxi Province funded project No. of 20232BCJ22058, entitled "Research on Key Technologies of Metal Ultrathin Plates for High-Power Hydrogen Fuel Cells for Multi-Source Energy Equipment."

Conflict of interest

The authors declare that they have no competing interests.

Author contributions

Conceptualization: Ming Xuan Gan
Formal analysis: Tao Li, Beng Wah Chua
Investigation: Lijie Zhang, Guanjin Li
Methodology: Jiansheng Liu
Writing – original draft: Ming Xuan Gan
Writing – review & editing: Beng Wah Chua

Ethics approval and consent to participate

Not applicable.

Consent for publication

Not applicable.

Availability of data

Data are available from the corresponding author on reasonable request.

References

1. Gao H, Ji B, Jager IL, Arzt E, Fratzl P. Materials become insensitive to flaws at nanoscale: Lessons from nature. *Proc Natl Acad Sci U S A*. 2003;100(10):5597-600.

   doi: 10.1073/pnas.0631609100

2. Gibson LJ, Ashby MF, Karam G, Wegst U, Shercliff H. The mechanical properties of natural materials. II. Microstructures for mechanical efficiency. *Proc R Soc London A*. 1997;450(1938):141-162.

   doi: 10.1098/rspa.1995.0076

3. Ashby MF, Gibson LJ, Wegst U, Olive R. The mechanical properties of natural materials. I. Material property charts. *Proc R Soc London A*. 1995;450(1938):123-140.

   doi: 10.1098/rspa.1995.0075

4. Mayer G. Rigid biological systems as models for synthetic composites. *Science*. 2005;310(5751):1144-1147.

   doi: 10.1126/science.1116994

5. Wegst UG, Bai H, Saiz E, Tomsia AP, Ritchie RO. Bioinspired structural materials. *Nat Mater*. 2015;14(1):23-36.

   doi: 10.1038/nmat4089

6. Wang R, Suo Z, Evans A, Yao N, Aksay IA. Deformation mechanisms in nacre. *J Mater Res*. 2001;16(9):2485-2493.

   doi: 10.1557/JMR.2001.0340

7. Rabiei R, Bekah S, Barthelat F. Failure mode transition in nacre and bone-like materials. *Acta Biomater*. 2010;6(10):4081-4089.

   doi: 10.1016/j.actbio.2010.04.008

8. Zhao H, Yang Z, Guo L. Nacre-inspired composites with different macroscopic dimensions: Strategies for improved mechanical performance and applications. *NPG Asia Mater*. 2018;10(4):1-22.

   doi: 10.1038/s41427-018-0009-6

9. Gan MX, Wong CH. Properties of selective laser melted spodumene glass-ceramic. *J Eur Ceram Soc*. 2017;37(13):4147-4154.

   doi: 10.1016/j.jeurceramsoc.2017.04.060

10. Gan MX, Wong CH. Experimental studies on the properties of selectively laser melted alumina-spodumene composite. *Ceram Int*. 2018;44(15):19008-19015.

    doi: 10.1016/j.ceramint.2018.07.144

11. Griffith ML, Halloran JW. Freeform fabrication of ceramics via stereolithography. *J Am Ceram Soc*. 1996;79(10):2601-2608.

    doi: 10.1111/j.1151-2916.1996.tb09022.x

12. Lee YH, Lee JB, Maeng WY, Koh YH, Kim HE. Photocurable ceramic slurry using solid camphor as novel diluent for conventional digital light processing (DLP) process. *J Eur Ceram Soc*. 2019;39(14):4358-4365.

    doi: 10.1016/j.jeurceramsoc.2019.05.069

13. Zhang K, Xie C, Wang G, He R, Ding G, Wang M, *et al*. High solid loading, low viscosity photosensitive Al_2O_3 slurry for stereolithography based additive manufacturing. *Ceram Int*. 2019;45(1):203-208.

    doi: 10.1016/j.ceramint.2018.09.152

14. Wu X, Zhang Z, Ma D, Lu X, Chen Z, Gao Y, *et al*. Influence of Al_2O_3 platelets addition on ceramic slurry and local flow induced platelets alignment in ceramic mask stereolithography process. *Ceram Int*. 2022;48(9):13134-13143.

    doi: 10.1016/j.ceramint.2022.01.190

15. Yang Y, Wang Z, He Q, Li X, Lu G, Jiang L, *et al*. 3D printing of nacre-inspired structures with exceptional mechanical and flame-retardant properties. *Research (Wash DC)*.

2022;2022:e9840574.

doi: 10.34133/2022/9840574

16. Li T, Liu Q, Qi H, Zhai W. Prestrain programmable 4D printing of nanoceramic composites with bioinspired microstructure. *Small*. 2022;18(47):e2204032.

doi: 10.1002/smll.202204032

17. Lewis JA. Colloidal processing of ceramics. *J Am Ceram Soc*. 2004;83(10):2341-2359.

doi: 10.1111/j.1151-2916.2000.tb01560.x

18. Song F, Soh AK, Bai YL. Structural and mechanical properties of the organic matrix layers of nacre. *Biomaterials*. 2003;24(20):3623-3631.

doi: 10.1016/s0142-9612(03)00215-1

19. Goswami A, Umarji AM, Madras G. Thermomechanical and fractographic behavior of poly (HDDA-co-MMA): A study for its application in microcantilever sensors. *Polym Adv Technol*. 2012;23(12):1604-1611.

doi: 10.1002/pat.3035

ACCSCIENCE PUBLISHING

Materials Science in Additive Manufacturing

ORIGINAL RESEARCH ARTICLE

Effect of bioactive borate glass on printability and physical properties of hydrogels

Fateme Fayyazbakhsh[1,2,3]*, Mehedi H. Tusar[1], Yue-Wern Huang[3,4], and Ming C. Leu[1,2,3]

[1]Department of Mechanical and Aerospace Engineering, Missouri University of Science and Technology, Rolla, Missouri, United States of America

[2]Intelligent System Center, Missouri University of Science and Technology, Rolla, Missouri, United States of America

[3]Center for Biomedical Research, Missouri University of Science and Technology, Rolla, Missouri, United States of America

[4]Department of Biological Sciences, Missouri University of Science and Technology, Rolla, Missouri, United States of America

Abstract

Hydrogels are a key component in bioinks and biomaterial inks for bioprinting due to their biocompatibility and printability at room temperature. The research described in the present paper contributes to the advancement of bioprinting by studying the effect of bioactive borate glass (BBG) incorporated into hydrogels on printability and physical properties. In this study, we fabricated 3D-printed hydrogel scaffolds using gelatin and alginate hydrogel mixture incorporated with various amounts of BBG, a bioceramic rich in therapeutic ions including boron, calcium, copper, and zinc. We investigated the effect of incorporating BBG on the density, viscosity, physical interactions, chemical structure, and shear thinning behavior of gelatin-alginate hydrogel biomaterial ink at different temperatures. After 3D printing and crosslinking of scaffolds, we measured mechanical properties and printing outcomes. The near-optimal extrusion temperature and pressure for uniform extrusion of hydrogel filaments at various BBG contents were determined. We compared the printing outcomes by quantifying the uniformity of printed filaments and shape fidelity of printed scaffolds. The rheological analysis showed that the addition of BBG increased the viscosity of the biomaterial inks and Young's modulus of the 3D-printed scaffolds. Biomaterial inks with a dynamic viscosity within the range of 4.5 – 6.5 Pa·s showed the best printability across all samples. In conclusion, the inclusion of BBG contributes to a substantial improvement in the physical properties and printability of 3D-printed gelatin-alginate hydrogels.

Keywords: Bioprinting; Hydrogel; Bioactive glass; Extrudability; Printability; Shape fidelity

***Corresponding author:**
Fateme Fayyazbakhsh
(f.fba@mst.edu)

Citation: Fayyazbakhsh F, Tusar MH, Huang Y, *et al.* Effect of bioactive borate glass on printability and physical properties of hydrogels. *Mater Sci Add Manuf.* 2024;3(1):2845.
doi: 10.36922/msam.2845

Received: January 30, 2024

Accepted: March 11, 2024

Published Online: March 22, 2024

1. Introduction

Three-dimensional (3D) bioprinting, a transformative technology in tissue engineering, uses layer-by-layer deposition of various bioink and biomaterial ink formulations to fabricate living tissues and biomimetic structures.[1,2] As per the terminology proposed by Groll *et al.*, the term "bioink" generally describes a formulation of cells suitable for

processing by automated biofabrication technologies. Aqueous formulations of polymers or hydrogel precursors containing biological factors are categorized as biomaterial inks that can become bioinks upon the addition of cells to the formulation.[3]

By employing hydrogels as the primary bioink material, extrusion-based 3D bioprinting, the most commonly used type of 3D printing in tissue engineering applications, enables the placement of biological materials typically within a supportive matrix, mimicking the environment of native tissues for a variety of applications.[1,4-6] Hydrogels are hydrophilic polymer materials with several advantages for 3D bioprinting, including biocompatibility, tunable extrudability and printability, biodegradability, and the ability to encapsulate and deliver bioactive molecules and living cells. These features make hydrogels ideal for creating functional biomimetic constructs that promote cellular response, tissue regeneration, and specific functions aligned with the intended objectives.[7,8] Hydrogels are often characterized by their high percentage of water content, which contributes to their softness and flexibility. While this property makes them suitable for 3D printing, encapsulation, tissue regeneration, and angiogenesis, it compromises their mechanical strength and stiffness, biodegradation rate, and dimensional accuracy.[9,10] Figure 1 illustrates the advantages and disadvantages associated with hydrogel materials.

Most physically crosslinked hydrogels exhibit shear thinning behavior, where their viscosity decreases under increased shear rate, allowing them to flow smoothly through bioprinting nozzles and deposit onto the print surface. The presence of hydrophilic moieties such as carboxyl, amide, amino, and hydroxyl groups contributes to the high hydrophilicity of hydrogels and absorbing relatively large amounts of fluids. This high water content results in a low density of polymer chains per unit volume, which leads to weak interactions between adjacent chains and ultimately results in poor mechanical properties in hydrogels. In particular, the weak physical interactions in physically crosslinked hydrogels result in poor resistance against gravitational sagging and poor stabilization of the ink after dispensing.[10-13] The obtained filaments spread fairly easily in 3D-bioprinted constructs composed of these hydrogels, leading to poor shape retention. This affects the subsequently printed layers and, consequently, the whole structure, as the first few printed layers are prone to collapse or deformation under the weight of the upper layers. Shear-thinning hydrogels can be extruded at room temperature, minimizing harm to encapsulated cells and preserving temperature-sensitive biomolecules. However, most physically crosslinked hydrogels, such as gelatin, face technical challenges in 3D bioprinting, including: (i) temperature-dependent extrudability, where the viscosity of the hydrogel changes with temperature, affecting extrudability; (ii) poor dimensional accuracy due to surface tension and interfacial forces, leading to layer fusion, particularly exacerbation in smaller parts; (iii) shrinkage and swelling that occur in response to crosslinking and environmental changes, altering construct dimensions and other properties; and (iv) poor shape fidelity after 3D printing.[6,14-20] Beyond hydrogel's inherent limitations, the current practices for evaluating printing outcomes often rely on subjective visual inspection of printability.[6] Researchers are actively addressing these challenges through various strategies, including modifying hydrogel composition with reinforcing agents, optimizing crosslinking methods, and applying post-printing treatments.[5,21-28]

Gelatin is a heterogeneous mixture of polypeptides obtained by controlled hydrolysis of collagen with cell-adhesive ligands such as the tripeptide Arg-Gly-Asp (RGD) sequence. Gelatin is a low-cost biodegradable protein with molecular weight ranging from 15 to 400 kDa.[29] It exhibits shear thinning behavior, and its viscosity is dependent on temperature because the hydrogen bonds that hold the triple-helix conformation of gelatin together are weakened by increased temperature. It undergoes physical gelation below room temperature, which can restore collagen-like triple helix structures at 25 – 35°C, and above this range, the triple helix dissociates, allowing the solvation of gelatin chains.[30-32] Various gelatin-based bioinks have been formulated to improve biocompatibility and enable the thermal crosslinking of the compound at room temperature.[31,33]

Alginate is a naturally occurring, low-cost, non-toxic, and biodegradable linear anionic heteropolysaccharides composed of (1 – 4)-linked β-d-mannuronic (M) and α-l-guluronic (G) acids, arranged in the homogeneous (MM or GG) and heterogeneous (MG or GM) blocks. The ionic crosslinking of alginate occurs when calcium ions interact with the carboxyl groups (COO-) present in both G and M blocks. Calcium ions form bridges between the carboxyl groups of adjacent G blocks, linking them together to form a 3D network structure, also known as the egg-box mode mechanism. The aqueous solution of sodium alginate can be easily extruded and, afterward, form hydrogels when crosslinked with calcium ions to immobilize the hydrogel and improve its mechanical properties at room temperature.[34-37]

Although extensive research has demonstrated the biocompatibility and performance of 3D-bioprinted hydrogels, the incorporation of additional components can further enhance their properties, broadening their

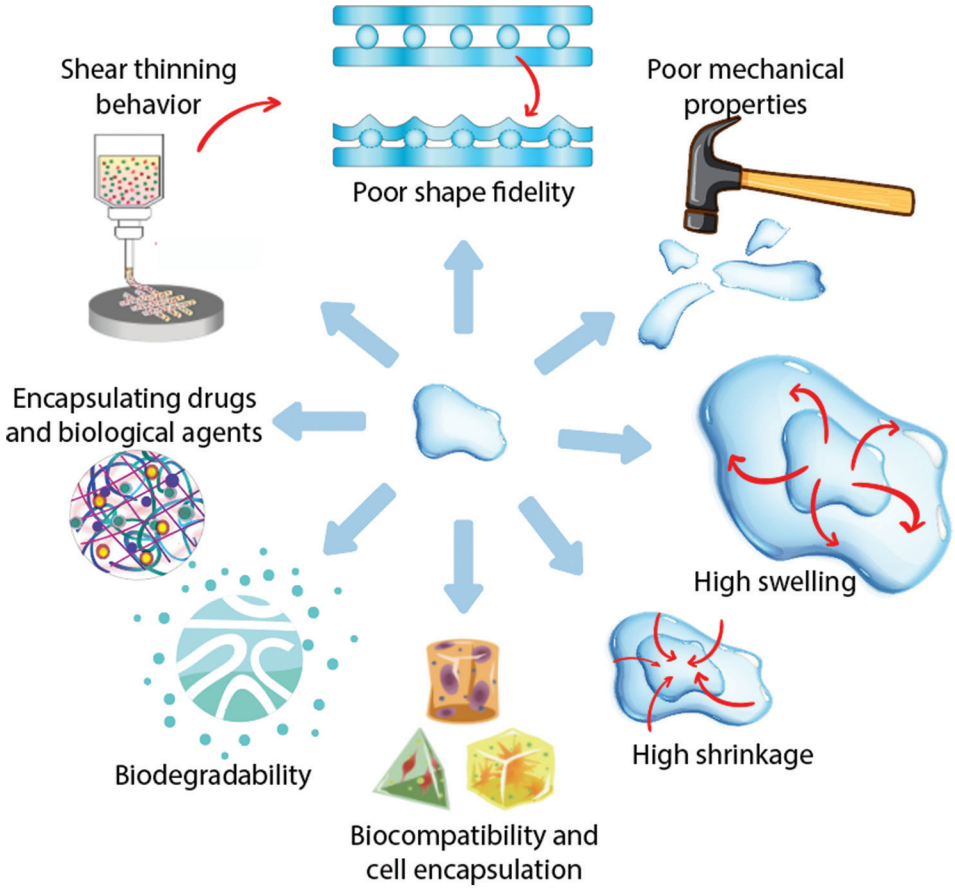

Figure 1. Schematic of hydrogels features. Despite biocompatibility and high encapsulation capacity, hydrogels face challenges in tissue engineering, including unstable dimensional accuracy, poor mechanical properties, and fast degradation.

applicability in tissue engineering and regenerative medicine. In our previous research, we have explored the incorporation of various ceramics such as silicate glass, borate glass, and transition metal carbides into hydrogels to enhance mechanical properties, conductivity, stimuli-responsiveness, and therapeutic potential.[8,38-42] Our preclinical studies have demonstrated promising results in dermal tissue regeneration.[21] Bioactive borate glass (BBG)-incorporated hydrogels have exhibited biocompatibility, bioactivity, tunable therapeutic ion release, and favorable mechanical properties,[43-49] making them suitable bioinks and biomaterial inks for 3D printing. BBG is a bioactive glass with promising properties for tissue engineering and regenerative medicine. Its incorporation into hydrogels has been shown to enhance mechanical properties and biocompatibility. The therapeutic ion release, printability, and mechanical properties of BBG-incorporated hydrogels can be fine-tuned by controlling the amount of BBG in the hydrogel for different applications. This tunability makes hydrogel-BBG compound an attractive biomaterial ink for 3D printing applications. However, there is a knowledge gap regarding the specific effects of BBG on the hydrogel's extrudability and printability.

In this study, we investigated the effect of BBG on hydrogel's physical properties and printability for 3D bioprinting applications. We prepared biomaterial ink formulations using gelatin, alginate, and varying amounts of BBG (0, 10, 15, and 20 wt%). The density, chemical structure, rheological behavior, and mechanical properties of the biomaterial inks were measured. Printability was assessed considering extrudability, filament uniformity, and shape fidelity. The results showed that BBG incorporation enhanced the mechanical properties and printability of the hydrogels, with higher BBG concentrations resulting in increased Young's modulus and enhanced extrudability, filament uniformity, and shape fidelity of the printed constructs.

2. Materials and methods

2.1. Materials

Gelatin (type B, gel strength ~ 225 g Bloom), sodium alginate (alginic acid sodium salt from brown algae, Brookfield

viscosity ≥2 Pa·s at 2% in water at 25°C, molecular weight of 200 kDa), bromothymol blue, and anhydrous calcium chloride were purchased from Sigma Aldrich (Missouri, USA). The bioactive borate glass (BBG 1605, microspheres at particle size <20 μm) was supplied by ETS Wound Care (Missouri, USA). Deionized water was used in biomaterial ink preparation and other experiments.

2.2. Biomaterial ink preparation

As described in our previous work,[8,21] biomaterial ink formulations were prepared by alginate, gelatin, and BBG. The 1605 bioactive borate glass (BBG) utilized in this research is composed of 51.6 wt% B_2O_3, 20 wt% CaO, 6 wt% Na_2O, 5 wt% MgO, 4 wt% P_2O_5, 12 wt% K_2O, 1 wt% ZnO, and 0.4 wt% CuO. This BBG demonstrates high solubility and rapid degradation compared to silicate glass such as Bioglass 45S5 and 1393 borate glass.[50] First, 1 L of 20 mg/mL glass suspension was prepared by dissolving 20 g BBG powder in 1 L of deionized water. The obtained suspension was filtered (pore size <0.22 μm) and centrifuged at 2000 rpm for 2 min. The obtained BBG suspension was then diluted with DI water to obtain 0, 10, 15, and 20 mg/mL concentrations of BBG. Gelatin powder (500 mg) was added to each BBG suspension (10 mL each) and stirred at 600 rpm at 40°C, followed by the addition of 2.5 mg of pH-sensitive dye (bromothymol blue) to the mixture. After 10 min, 300 mg sodium alginate was added to the mixture drop-wise and stirred at 1200 rpm for 20 min. The concentration of gelatin and alginate was set at 50 mg/mL and 30 mg/mL, respectively, as our previous research showed that the 5:3 gelatin-alginate ratio demonstrates Young's modulus in the range of human skin with the best biocompatibility and wound healing outcome.[8,21] The coding of the samples was established based on the weight percentage (wt%) of dry material for each component. In the biomaterial inks, the concentrations of gelatin, alginate, and BBG were set at 5%, 3%, and 0 – 2%, respectively. Then each biomaterial ink sample was poured into 3D printing cartridges (Nordson, Ohio, USA). Cartridges were centrifuged at 2000 rpm for 2 min and incubated at 37°C for 1 h to debubble the inks. We did not include biomaterial inks with BBG content >20 mg/mL in this research because it was found from our preliminary tests that gelatin-alginate hydrogel inks incorporated with BBG higher than 20 mg/mL were not extrudable.

2.3. Three-dimensional printing

The 3D-printed scaffolds were fabricated using an extrusion-based bioprinter (Inkredible+, CellInk Corp., Sweden), which allows control over printing parameters, including nozzle temperature, layer height, and printing speed. The G-code defined a scaffold printing pattern that consisted of square-shaped pores. The print bed temperature was set at 19°C, and the biomaterial inks were deposited at a speed of 3600 mm/min for linear patterns and 1200 mm/min curve patterns. All samples were printed with the same-size nozzles (0.41 mm inner diameter, Nordson, USA). The print head nozzle temperature was set at each of 25°C, 30°C, 35°C, and 40°C. Extrusion pressure ranged from 15 to 125 kPa. After printing 21 layers, the printed scaffold was immersed in $CaCl_2$ solution (1 mol/L) for 10 min to form crosslinks, thereby enhancing the scaffold's mechanical properties. After cross-linking, the scaffold underwent multiple rinses with deionized water to wash away the remaining calcium ions. The crosslinked scaffolds were stored at 4°C for further characterization.

2.4. Characterization

The crosslinked scaffolds were characterized in this study in terms of their density, chemical structure, rheological behavior, and mechanical properties.

2.4.1. Density

The density of each biomaterial ink formulation was measured by weighing 2 mL batches at five replications.

2.4.2. Chemical structure

The Fourier transform infrared spectroscopy (FTIR) was conducted using a Nicolet iS50 spectrophotometer (Thermo Scientific, USA), outfitted with a mid-IR range (4000 – 400 cm^{-1}) diamond crystal cell for attenuated total reflection. Spectra were acquired at a 4 cm^{-1} resolution, totaling 32 scans per spectrum with a data interval of 0.482 cm^{-1}. To prepare for measurement, 500 μL of the hydrogel sample was spread thinly over the crystal to form a film on the splitter area. To maintain accuracy, a new reference spectrum was captured every five scans to correct the subsequent spectra. Analysis of the spectra was performed using the OMNIC software version 9.2.41 from Thermo Fisher Scientific (USA). The results were presented as a percentage of transmittance versus the wavenumber (cm^{-1}). Reference IR spectrum data from Sigma Aldrich were employed to pinpoint the characteristic chemical bonds present in gelatin, alginate, and water.

2.4.3. Rheological behavior

Dynamic viscosity (μ) was determined at various temperatures using a rotational rheometer (Kinexus Ultra+, Malvern Panalytical Ltd., U.K.) equipped with a cone and plate setup (CP4/40) and a lower fixture (PED40) for sample handling. The apparatus was set to a 40 mm-diameter cone with a 4° angle. A solvent trap was employed to minimize sample evaporation. The loading and working gaps were

set to 70 mm and 0.5 mm, respectively. After calibration and temperature setting of the lower fixture, samples were carefully placed and enclosed by a hood. Dynamic viscosity of hydrogel-BBG inks was taken as the average of the data for shear rate ($\dot{\Upsilon}$) in the range of $1 < \dot{\Upsilon} < 10\ s^{-1}$, at temperatures including 25, 30, 35, and 40°C. The shear thinning behavior of the dressings was measured through a shear rate ramp from 0.1 to 1000 s^{-1} over a 10-min duration at 25, 30, 35, and 40°C.

2.4.4. Mechanical properties

The mechanical properties of the 3D-printed scaffolds were measured utilizing an Instron 5969 Universal Testing System (USA). A dual-column apparatus designed for tensile tests was used in accordance with ASTM F2150-8 standard. Specimens were stretched at the rate of 5 mm/min until ruptured at 20°C. Young's modulus for the specimens was determined from the stress-strain curve. The BlueHill Universal testing software was employed for test control and data analysis. A total of five repetitions (n = 5) were conducted for each set of parameters.

2.5. Printability measurement

In this study, the printability measurement involved the assessment of various printing outcomes in terms of extrudability, filament uniformity, and scaffold shape fidelity, as described below. We studied the effects of ink composition (with varying BBG content) and printing parameters, including nozzle (ink) temperature and extrusion pressure, on printing outcomes.

2.5.1. Extrudability

Ouyang *et al.* categorized hydrogel extrudability based on gelation conditions of the extruded filament: over-gelation, ideal gelation, and under-gelation.[51] Achieving ideal gelation is crucial for extrudability, which is characterized by a consistent flow with a smooth filament. Over-gelation is characterized by inconsistent lumpy flow, resulting in irregular filament shape and poor layer attachment. Under-gelation is characterized by a state akin to that of a liquid, or in some instances, the formation of droplets. Under-gelation may result in the merging of adjacent layers and the formation of pores with a predominantly circular rather than square morphology.[52]

2.5.2. Filament uniformity

A series of single-layer straight lines were printed to assess the uniformity of the printed filaments, similar to what was previously described in literature.[8] Filaments were printed at 25, 30, 35, and 40°C, with three replications for each ink composition and printing parameter set. The width of each printed filament was measured at 20 random points at three replications. The filament uniformity is defined using the following equations:

$$\text{Cofficient of variation (CV)} = \frac{\text{SD}(W_i)_{i=1,n}}{\frac{\sum_i^n W_i}{n}} \quad \text{(I)}$$

$$\text{Filament uniformity (FU)} = 1 - \text{Coefficient of variation (CV)} \quad \text{(II)}$$

where W_i and SD (W_i) are the filament width measured at each random point and the standard deviation of filament widths at the random points, respectively. A lower coefficient of variation (CV) means a higher filament uniformity.

2.5.3. Shape fidelity

Following the work of Ouyang *et al.*[51] and Kyle *et al.*,[52] we define shape fidelity (SF) as a measure of how closely scaffold pores, intended to be square-shaped, resemble perfect squares. This is characterized using the following equation:

$$\text{Shape fidelity (SF)} = \frac{P^2}{16A} \quad \text{(III)}$$

where A is the pore area, and P is the pore perimeter. As illustrated in Figure 2, in a porous scaffold designed with square-shaped pores, the actual pore shape may appear in a different shape (such as an oval shape), deviating from the intended square shape. We measured the area and perimeter for each pore using ImageJ software, and then obtained the shape fidelity as the average of shape fidelity values calculated, using Equation III, for 10 randomly selected pores in each scaffold, with three replications, for each ink composition at corresponding desired temperature and extrusion pressure. Note that SF is equal to 1 for a perfect square, and a pore with a lower SF value has a larger deviation from the square shape.

2.6. Statistical analysis

All experiments in this study were conducted with a minimum of three replications for each sample per test. All data are expressed as mean ± standard deviation (SD). One-way analysis of variance (ANOVA) was employed to determine statistical differences among different groups. This statistical test enables the evaluation of overall group differences and determines if there are significant differences between the means of these groups. Significance was set at the $P < 0.05$. Statistical analyses were performed using Microsoft Excel.

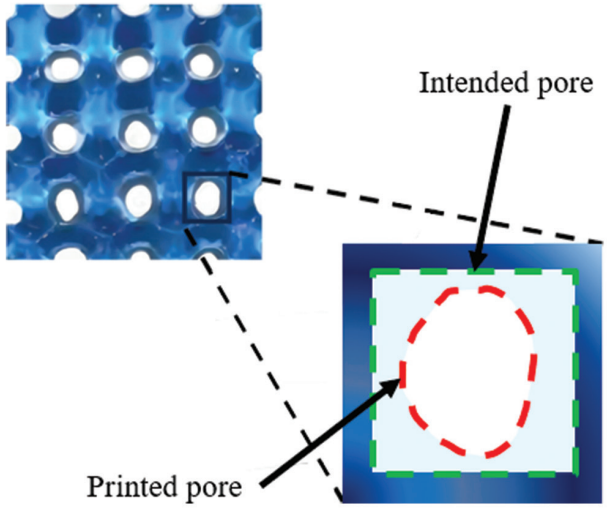

Figure 2. Illustration of an oval-shaped pore (red dashed line) that is intended to be a square pore (green dashed line) in a scaffold design.

3. Results and discussion

3.1. Effect of BBG content on physical crosslinking and mechanical properties

The rheological behavior and printability of hydrogel-BBG samples are driven by their degree of crosslinking and physical parameters (printing temperature, pressure, *etc.*). Figure 3A depicts the FTIR spectra of the 3D-printed scaffolds with various BBG amounts. The incorporation of BBG into the gelatin-alginate hydrogel introduces a higher concentration of metallic oxides, as denoted by the blue box in Figure 3A. Introducing the divalent cations such as Ca^{2+} and Mg^{2} released from BBG facilitates the ionic crosslinking of alginate due to the interactions between these ions with the carboxyl groups. The divalent ions link the carboxyl groups of adjacent G blocks together to form a 3D network structure in the alginate chains.[34,36] The increase in crosslinking density in the alginate chains can be evidenced by (i) the shift to the right on the metallic bonds, indicating the increased bond energy, which can potentially increase the physical interactions with carboxyl groups present in alginate, and (ii) the sharper C=O valleys with a slight shift to the right, demonstrating increased attractions between negatively charged carboxyl groups and Ca^{2+} with other divalent cations. The increase in the degree of ionic crosslinking results in higher rigidity in the alginate.[53,54] On the other hand, the physical interactions between the ions released from BBG and various functional groups present in gelatin, such as carboxyl, amide, amino, and hydroxyl groups and ions released from BBG can decrease the free volume in the hydrogel network and the total volume of the hydrogel-BBG mixture. The spectrum indicates that as BBG content is increased, the metallic bonds become more prevalent and shift to the right, indicating the increase in physical interactions between various components of the biomaterial inks. The increased secondary bonds within the gelatin network can affect its temperature-dependent shear thinning behavior and viscosity. The added intermolecular physical interactions, along with the intramolecular hydrogen bonds, affect the conformation of the triple-helix within gelatin. Therefore, the dissociation of the triple helix requires more energy and the temperature of physical gelation increases. The changes in the physical crosslinking of alginate and physical interactions in gelatin can contribute to the further enhancement of mechanical strength and may influence the stability, water permeability, and swelling capacity, as reported in our previous work and other research.[17,54] A higher density of crosslinking can result in the rigidity of the biomaterial inks due to the increased resistance to flow and the friction between hydrogel chains.

Figure 3B shows the density of the scaffolds with varying BBG amounts. The density increases in scaffolds with increased BBG amount due to (i) BBG's higher density compared to the hydrogel, (ii) the reduction in free volume caused by the formation of crosslinks between the hydrogel chains, and (iii) the formation of secondary bonds between BBG ions and hydrogel chains. After ion exchange between sodium ions and bivalent metals released from BBG, the shorter bond length reduces the free volume within the hydrogel network and increases the evacuation of water molecules, resulting in hydrogel solidification and, therefore, increased density. The mechanical stiffness of 3D-printed scaffolds, as indicated by Young's modulus measurements, is displayed in Figure 3C, showing the addition of BBG increases Young's modulus of the hydrogel. It is a result of the ionic crosslinking of alginate chains within the hydrogel network in the presence of the divalent ions released from BBG.

The stiffness of natural human skin was reported in the range of 0.45 – 0.85 MPa.[55] Our scaffold samples incorporating BBG fall within this range for all of the hydrogel-BBG (H-BBG) tested, *i.e.*, H-BBG10, H-BBG15, and H-BBG20. This indicates that these scaffolds exhibit a level of elasticity that resembles the properties of natural skin. This finding suggests that the hydrogel scaffold incorporating BBG up to 20 wt% possesses a degree of elasticity that is well-suited for potential applications in soft tissue engineering, such as in skin wound treatment. However, it should be noted that, as demonstrated in this study, incorporating BBG at concentrations higher than 20 wt% into the gelatin-alginate (with a ratio of 5:3) hydrogel compound can significantly impede the bioprinting process.

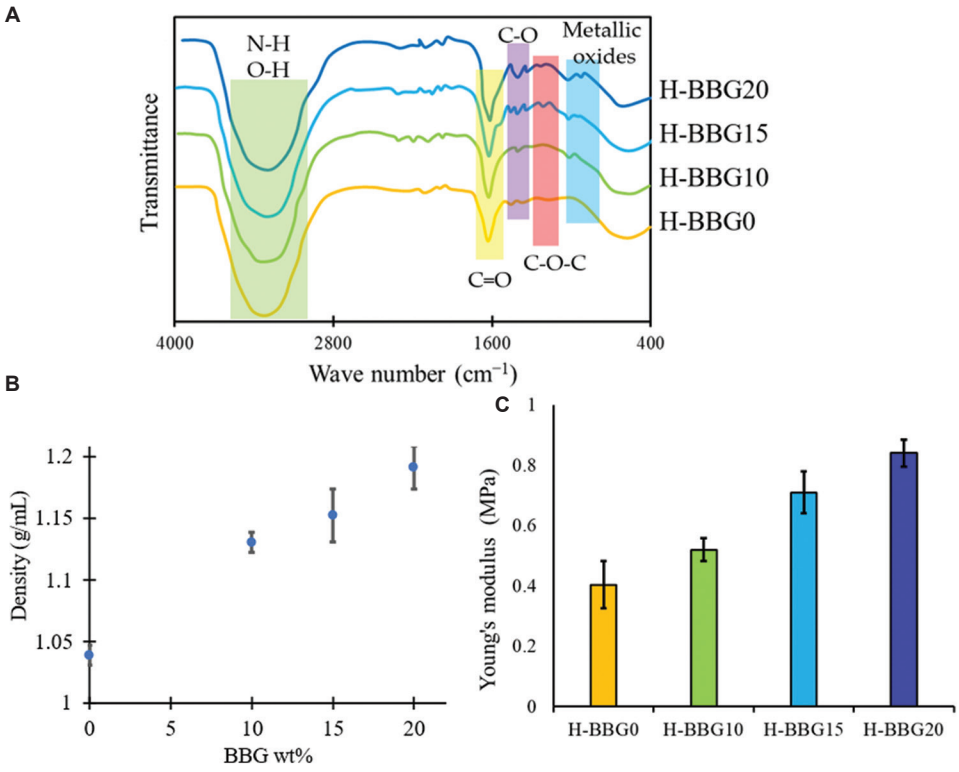

Figure 3. (A) FTIR spectra of hydrogel-BBG scaffolds. (B) The density of hydrogel-BBG inks increases with BBG content. (C) Young's modulus of hydrogel-BBG scaffolds, showing its increase with the addition of BBG.
Abbreviations: H-BBG: Hydrogel-bioactive borate glass; FTIR: Fourier transform infrared.

3.2. Effect of temperature, pressure, and BBG content on viscosity

To identify the relationship between printability and biomaterial ink composition, we first quantified the dynamic viscosity (μ) of the biomaterial inks. Figure 4 depicts the dynamic viscosity of the formulated hydrogel-BBG samples at 25, 30, 35, and 40°C. Higher viscosity was observed at 25°C across all samples, which showed a significant drop in viscosity when the temperature was increased from 25 to 40°C. While H-BBG10 ink showed relatively small changes in viscosity at the higher temperatures of 35 and 40°C from 30°C, H-BBG15 and H-BBG20 showed substantial drops in viscosity at these higher temperatures.

Temperature can significantly impact the viscosity of gelatin solutions by affecting the conformational state of the triple helix. In general, the reduced viscosity at higher temperatures results from the transition in hydrogel chain orientation from chains in a random direction to align with the direction of the applied shear. At the molecular level, the decrease in viscosity of hydrogels at higher temperatures is attributed to the elevated kinetic energy in the hydrogel network, increasing its mobility. This increased mobility allows the hydrogel chains to slide past each other more easily, reducing the resistance to flow. At lower temperatures, gelatin molecules tend to adopt a more ordered triple helical structure, which contributes to higher viscosity due to increased molecular entanglement and intermolecular interactions. As temperature increases, the thermal energy disrupts these ordered structures, causing gelatin chains to dissociate the triple helix, resulting in decreased viscosity. In our previous research, we observed that gelatin solutions transition from a gel-like state to a more fluid-like state with increasing temperature.

In addition, the intermolecular forces and interactions between gelation and alginate chains with each other and BBG ions are responsible for the 3D integrity of the hydrogels. At higher temperatures, the increased entropy weakens these forces, allowing for easier chain movement and higher flowability of the hydrogel, *i.e.*, lower viscosity.

In contrast with elevated temperature, the presence of BBG strengthens the hydrogel network and increases the resistance of hydrogel chains to alignment in the direction of applied shear stress. Therefore, the hydrogel chains require higher kinetic energy for the transition from random fibers to aligned structures. As a result, the

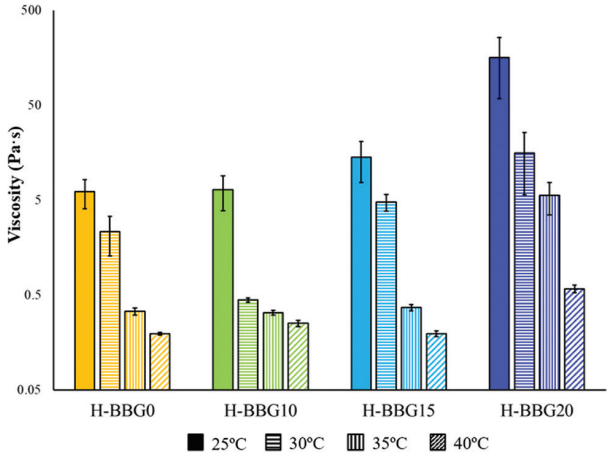

Figure 4. Dynamic viscosity of hydrogel-BBG (H-BBG) inks at various temperatures was taken as the average of the shear rate data for 1<shear rate<10 s^{-1}.

observed drop in gelatin-alginate viscosity is influenced by the concentration of BBG, as shown in Figure 4. Unlike H-BBG10, we observed a significant impact of thermal energy, *i.e.*, the elevated temperature on the drop of viscosity in H-BBG15 and H-BBG20. These findings suggest that the concentration of BBG is a key factor in determining its effectiveness in modulating the hydrogel viscosity.

The applied extrusion pressure affects the flow rate of hydrogel-BBG inks through a nozzle in the printing process. Therefore, the ink's shear rate is a function of pressure[56] and viscosity (which is influenced by temperature). Figure 5 shows the shear thinning behavior of biomaterial inks with various BBG amounts (H-BBG0, H-BBG10, H-BBG15, and H-BBG20) across the shear rate range from 0.1 to 1000 s^{-1} and different temperatures including 25, 30, 35, and 40°C. All samples exhibited shear thinning behavior, featuring the rheological behavior of non-Newtonian fluids whose viscosity decreases with increasing shear rate.[57] Our data here consistently showed a decrease in viscosity as a result of an increase in shear rate across all temperatures in all samples with various BBG contents. At 25°C, they exhibited the highest level of viscosity, which decreased rapidly as the shear rate increased. However, this decrease in viscosity was less sharp when the temperature was raised to 30, 35, and 40°C across all samples. H-BBG20 ink, which has the highest amount of BBG, exhibited the highest viscosity among all samples. This sample also showed the largest drop in viscosity as temperature increased from 25 to 40°C. It indicates that BBG modifies the rheological behavior of the gelatin-alginate hydrogel, which is caused by alteration to the chain alignment and the strength of intermolecular bonds in the hydrogel chain crosslinks.

3.3. Evaluation of printing outcomes

We evaluated the 3D printing outcomes by first testing the extrudability of each hydrogel-BBG sample to determine the ideal printing temperature for each biomaterial ink. Once ideal gelation was achieved at a certain temperature, filaments were printed to study filament uniformity, measured by filament line width variation as defined in Equations I and II. Filament uniformity was used to establish the desired extrusion pressure for each set of biomaterial ink composition and nozzle temperature. Afterward, scaffolds were printed using H-BBG0, H-BBG10, H-BBG15, and H-BBG20, each at the desired nozzle temperature and extrusion pressure. Subsequently, the shape fidelity of printed scaffolds was measured to identify the effect of BBG content on printability.

Figure 6 shows the extrusion tests performed at the temperature of 20, 25, 30, 35, and 40°C for H-BBG0 and H-BBG20 inks at the extrusion pressure of 35 and 75 kPa, respectively, to study the extrudability of these samples due to temperature-dependent gelation behavior. Among the various temperatures tested, H-BBG0 ink exhibited the best extrudability at 25°C, with continuous flow and no droplet formation. Therefore, the desired extrusion temperature for H-BBG0 was determined to be 25°C. At higher temperatures, the viscosity of H-BBG0 decreased substantially, resulting in the formation of ink droplets, which should be avoided. The addition of BBG to gelatin-alginate hydrogel in H-BBG20 led to a significant increase in viscosity and, thus a different result from the extrusion test. At the lower temperatures of 20 and 25°C, the high viscosity resulted in over-gelation, causing irregular filament formation that could be detrimental to the printing process. The gelation state was improved at 30°C, and H-BBG20 reached an ideal gelation state at 35°C, resulting in a viscosity suitable for extrusion and high extrudability, indicating that the biomaterial ink at this temperature achieves a desired balance between fluidity and rigidity for printing. At 40°C, the viscosity of H-BBG20 substantially decreased, leading to the formation of droplets, an indication of under-gelation. Therefore, the desired extrusion temperature for H-BBG20 was determined to be 35°C. From the extrusion test results, which are not included in Figure 6, we also found a near-optimal extrusion temperature of 25°C for H-BBG10 and 30°C for H-BBG15.

Visual assessment of the filament quality for H-BBG0, H-BBg10, H-BBG15, and H-BBG20 is depicted in Figure 7, for different extrusion pressures at the identified temperature for each ink through the extrudability study described above. Uniform, high-quality prints are marked with blue dash-line borders in Figure 7. As can

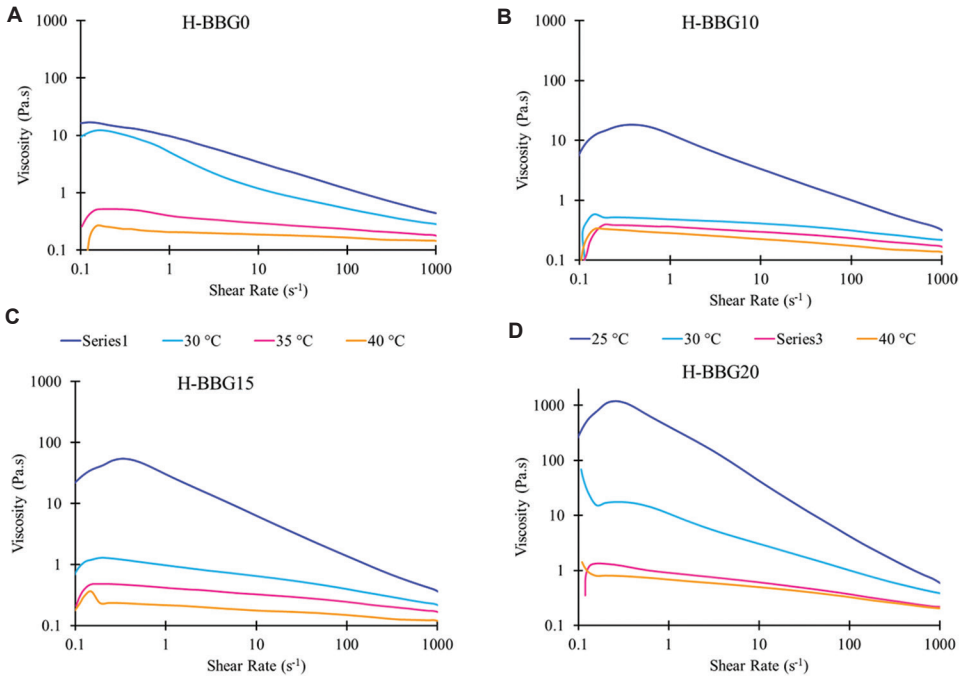

Figure 5. Shear thinning behavior of the hydrogel-BBG inks. Logarithmic plot of viscosity version shear rate for 0.1< < 1000 s^{-1} for (A) H-BBG0, (B) H-BBG10, (C) H-BBG15, and (D) H-BBG20.
Abbreviation: H-BBG: Hydrogel-bioactive borate glass.

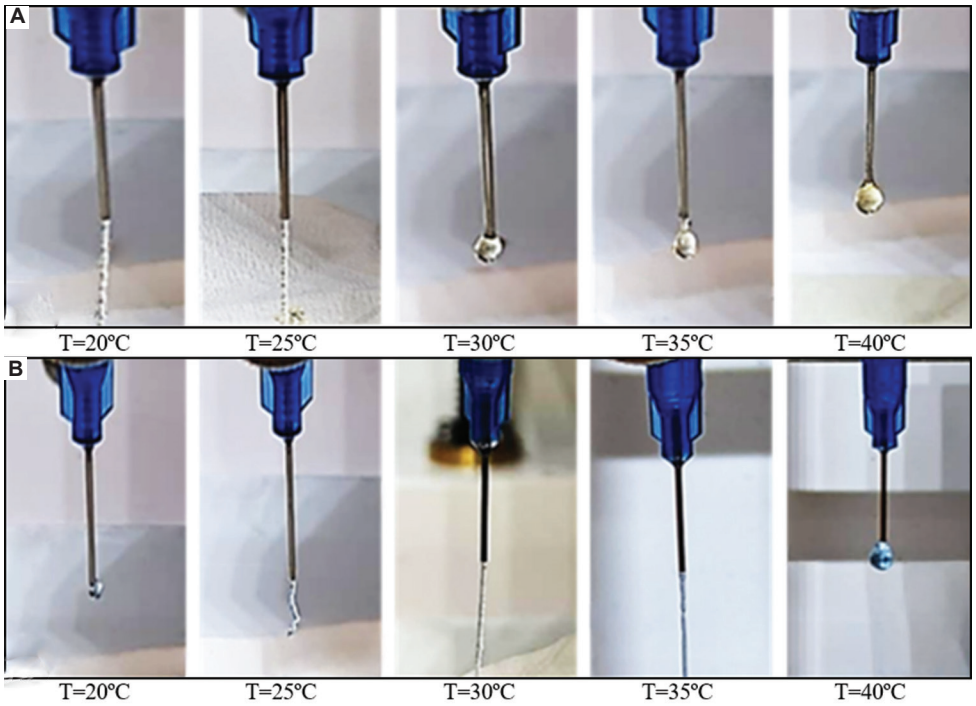

Figure 6. Extrusion test results for (A) H-BBG0 at 20, 25, 30, 35, and 40°C and P = 35 kPa, and for (B) H-BBG20 at 20, 25, 30, 35 and 40°C and P = 75 kPa. H-BBG0 and H-BBG20 showed ideal gelation at 25 and 35°C, respectively.
Abbreviation: H-BBG: Hydrogel-bioactive borate glass.

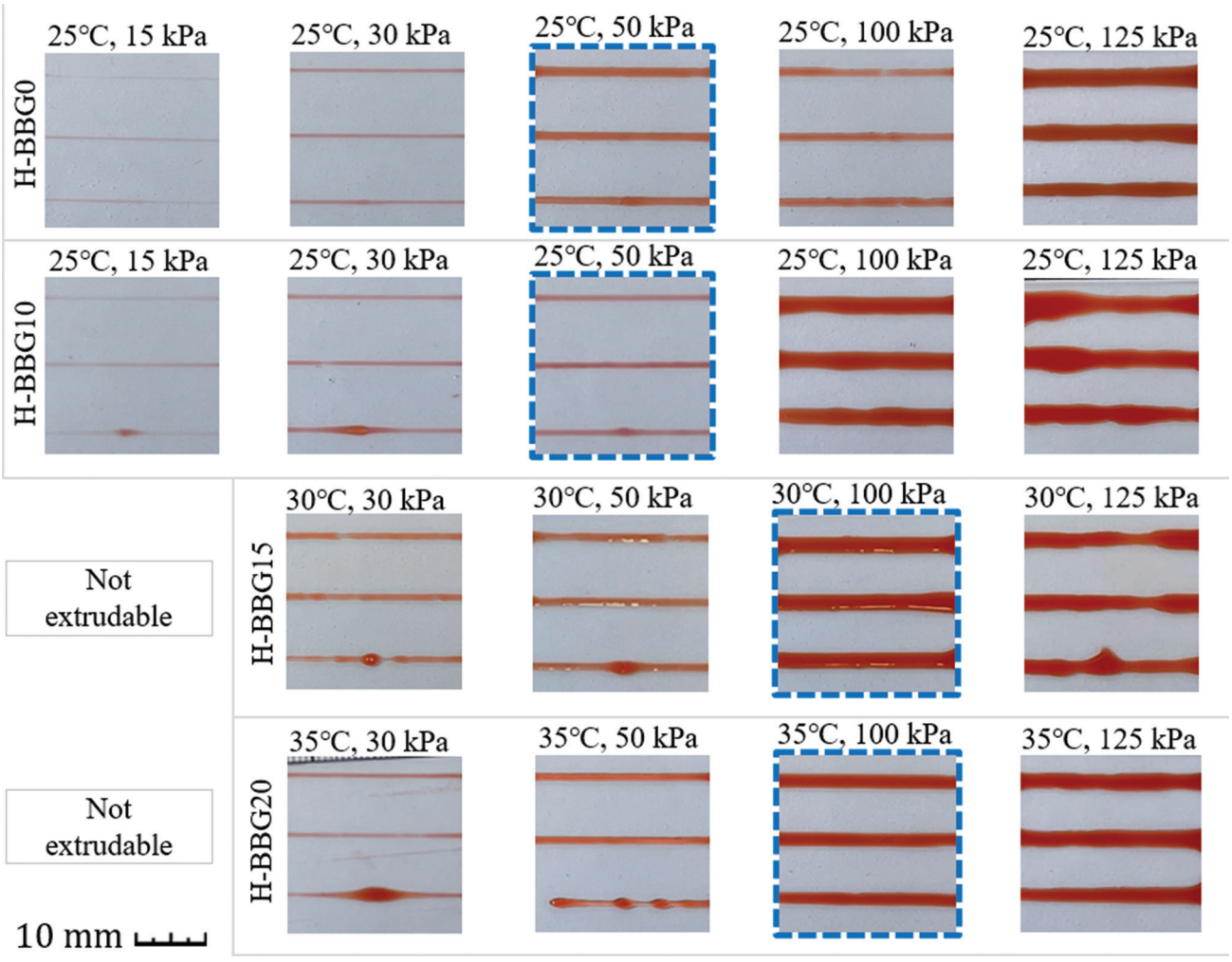

Figure 7. Filament uniformity test at various extrusion pressures using the temperature of best extrudability identified for the hydrogel samples with different BBG percentages. The highest-quality line prints are highlighted with blue, dash-line borders.
Abbreviation: BBG: Bioactive borate glass.

be seen from this figure and the filament widths plotted in Figure 8A, all samples show an increase in filament width when extrusion pressure is higher. Figure 8B shows the filament uniformity for each ink extruded at the desired temperature under various extrusion pressures. H-BBG0 and H-BBG10 showed the highest uniformity at the extrusion pressure of 50 kPa at 25°C, while H-BBG15 and H-BBG20 exhibited the highest uniformity at the extrusion pressure of 100 kPa at 30 and 35°C, respectively. These prints indicate near-optimal extrusion of the biomaterial ink, while the other prints at other extrusion pressures suggest suboptimal conditions, leading to either over-gelation or under-gelation, which could compromise the 3D printing outcomes. Together, Figures 6-8 clearly indicate a particular set of nozzle temperature and extrusion pressure for each ink to achieve the ideal gelation and thus filament uniformity. The identified near-optimal sets of nozzle temperature and extrusion pressure result in the best extrudability and filament uniformity for each of the biomaterial inks including H-BBG0, H-BBg10, H-BBG15, and H-BBG20.

The outcomes of printed scaffolds, as shown in Figure 9, exhibit substantial differences across the hydrogel inks with different BBG contents. Displayed in this figure is the intended scaffold geometry with square-shape pores for evaluating the outcomes of scaffold printing with H-BBG0, H-BBG10, H-BBG15, and H-BBG20 at the most desirable nozzle temperature and extrusion pressure for each of the biomaterial inks. The H-BBG0 and H-BBG10 scaffolds exhibit suboptimal, non-uniform pore geometry with substantial deviation from the intended square-shaped pores. In contrast, the 3D-printed scaffolds with

H-BBG15 and H-BBG20 demonstrate improved printing outcomes, with more consistent geometries and closer to square pores. These differences in print outcomes can be attributed to the rheological behavior of the biomaterial inks. Note that the 3D-printed H-BBG0 scaffold, despite obvious irregularities in pore geometry, still maintains the mesh structure. As shown in Figures 4 and 5, the H-BBG0 ink exhibits the lowest viscosity. From Figure 9, it becomes evident that the lower viscosity leads to the higher surface tension of the hydrogel after printing,[8] contributing to more fusion between adjacent layers and resulting in lower shape retention and formation of more deviated pore shapes at the scaffold corners. The notable viscosity increase in H-BBG15 and H-BBG20 inks correlates with improved shape fidelity at their respective near-optimal temperatures of 30°C and 35°C. Thus, the higher BBG content in H-BBG-15 and H-BBG20 inks contributes to significant enhancement in the hydrogel printability.

Figure 10 depicts the shape fidelity of 3D-printed scaffolds at various nozzle (ink) temperatures (not just the most desirable temperatures) for H-BBG0, H-BBG10, H-BBG15, and H-BBG20. The figure shows the highest shape fidelity at 25, 25, 30, and 35°C for H-BBG0, H-BBG10, H-BBG15, and H-BBG20, respectively. We compared the printability of these four biomaterial inks by using the highest shape fidelity for each of them. The addition of BBG appears to increase the printability, with higher BBG concentrations improving the biomaterial ink's printability, *i.e.*, its ability to form and retain the desired geometry. H-BBG20 showed a slight improvement in shape fidelity compared to H-BBG15, while both samples showed significant improvement (P <0.05) in shape fidelity compared to H-BBG10 and H-BBG0 (plain hydrogel). The printability improvement is attributed to BBG's effect on improving the biomaterial ink's rheological properties.

Table 1 provides data on viscosity, shape fidelity, and filament uniformity obtained from various tests at 25, 30, 35, and 40°C for H-BBG0, H-BBG10, H-BBG15, and H-BBG20, with the data represented by the mean and standard deviation for each set of temperature and BBG content. A plot of shape fidelity versus viscosity based on the mean values for all the data points is shown in

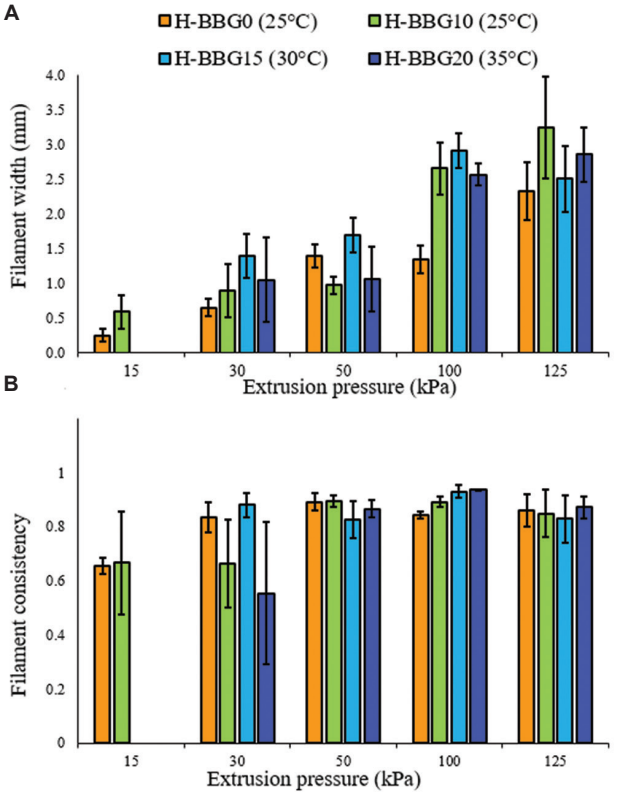

Figure 8. Filament width (A) and filament uniformity (B) obtained for printed filaments at various extrusion pressures with the temperature of best extrudability identified for the hydrogel biomaterial ink incorporating different BBG content.
Abbreviation: BBG: Bioactive borate glass.

Table 1. Viscosity, shape fidelity and filament uniformity for each biomaterial ink composition extruded and printed at 25, 30, 35, and 40°C

Biomaterial ink	25°C		30°C		35°C		40°C	
	Mean	SD	Mean	SD	Mean	SD	Mean	SD
H-BBG0								
Vis	6.01	2.09	2.33	1.04	0.33	0.03	0.19	0.01
SF	0.57	0.29	0.11	0.04	-	-	-	-
FU	0.89	0.03	-	-	-	-	-	-
H-BBG10								
Vis	6.34	2.57	0.44	0.21	0.32	0.02	0.25	0.01
SF	0.7	0.22	0.16	0.08	0.12	0.08	0.33	0.22
FU	0.89	0.02	-	-	-	-	-	-
H-BBG15								
Vis	14.12	6.47	4.88	0.95	0.37	0.02	0.19	0.01
SF	0.47	0.17	0.75	0.17	0.67	0.16	0.22	0.12
FU	-	-	0.93	0.02	-	-	-	-
H-BBG20								
Vis	158.15	99.64	15.74	10.08	4.68	2.09	0.58	0.05
SF	0.5	0.7	0.49	0.15	0.83	0.07	0.57	0.12
FU	-	-	-	-	0.94	0	-	-

Notes: The viscosity (Vis, unit: Pa·s) and shape fidelity (SF) for each biomaterial ink composition extruded and printed at 25, 30, 35, and 40°C are given. The filament uniformity (FU) for each sample is reported at the near-optimal extrusion temperature and pressure: 25°C and 50 kPa for H-BBG0 and H-BBG10; 30°C and 100 kPa for H-BBG0; and 35°C and 100 kPa for H-BBG20.
Abbreviation: H-BBG: Hydrogel-bioactive borate glass.

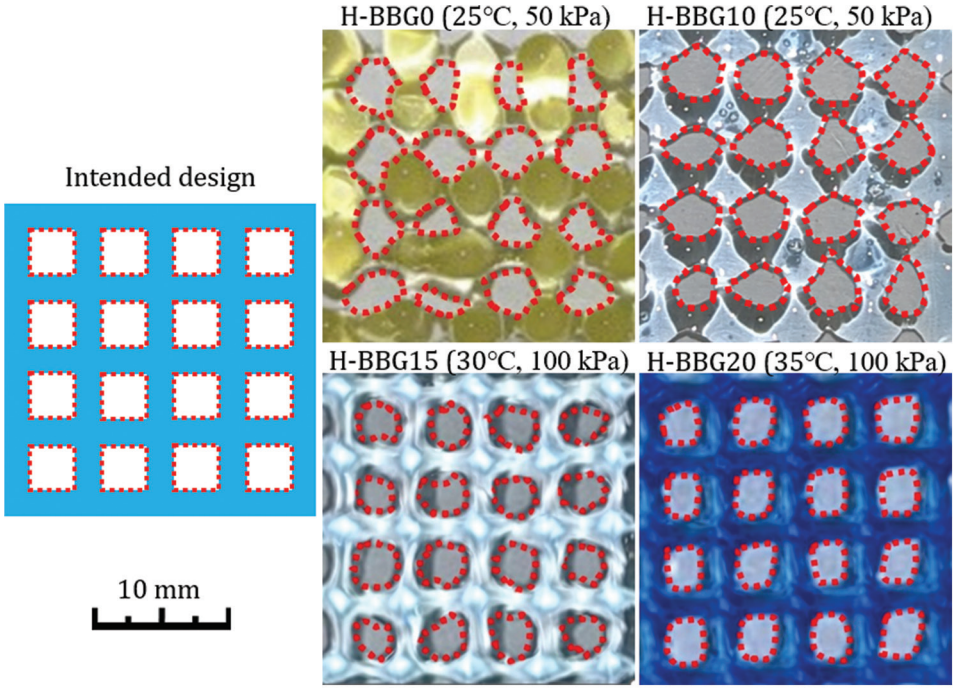

Figure 9. Scaffold appearance after 3D printing at near-optimal ink temperature and extrusion pressure for hydrogels with various BBG content.
Abbreviation: BBG: Bioactive borate glass.

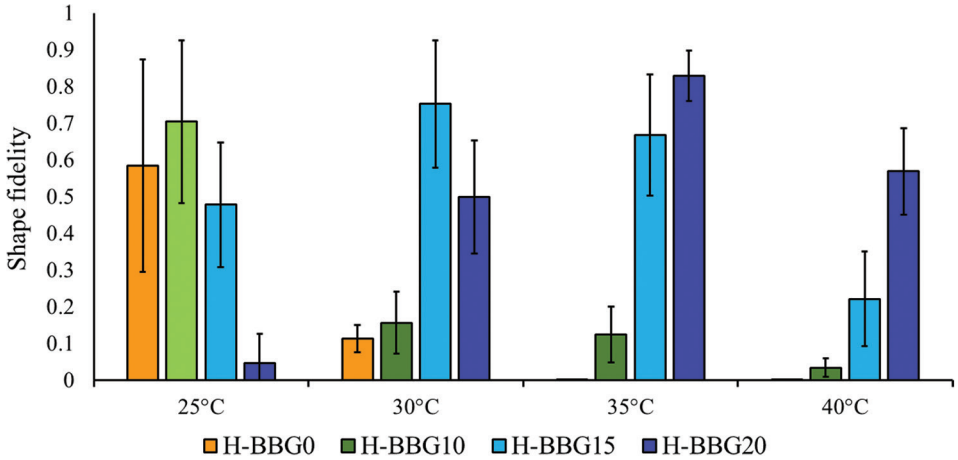

Figure 10. Shape fidelity of 3D-printed scaffolds at different temperatures for hydrogels with different BBG contents. H-BBG15 and H-BBG20 showed significant improvement in shape fidelity compared to the plain hydrogel (H-BBG0).
Abbreviation: H-BBG: Hydrogel-bioactive borate glass.

Figure 11. According to Table 1 and Figure 11, the highest shape fidelity falls within the range of 4.5 – 6.5 Pa·s, which exhibits the highest printability (most favorable printing conditions) for all gelatin-alginate hydrogel biomaterial inks incorporated with BBG.

As reported by He *et al.*, in general, materials with a viscosity lower than 0.3 Pa·s are more suitable for spreading rather than extrusion; however, for materials with a viscosity greater than 30 Pa·s, a large pressure is required to extrude the hydrogel out of a nozzle.[17] Suitable biomaterial inks and bioinks for extrusion-based 3D printing should possess both smooth flow and shape retention properties. Consistent with this research result, our findings suggested that there is a range of viscosity in that biomaterial inks and

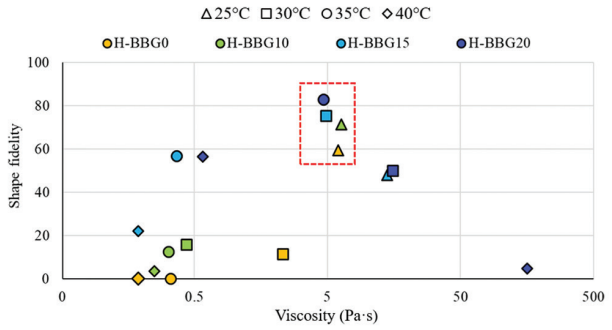

Figure 11. Shape fidelity versus viscosity plot. The best shape fidelity across all samples was observed within a dynamic viscosity range of 4.5 – 6.5 Pa·s, at 1< shear rate <10 (s^{-1}). This viscosity range exhibited the most favorable condition in all gelatin-alginate-BBG compositions for extrudability and maintaining shape characteristics.
Abbreviation: BBG: Bioactive borate glass.

bioinks exhibit the best printability. According to this study, for the hydrogel-BBG hydrogel inks, the best outcome of extrusion-based 3D printing occurs at a viscosity of the biomaterial ink in the range of 4.5 – 6.5 Pa·s.

Our data showed that, among H-BBG0, H-BBG10, H-BBG15, and H-BBG20, 3D-printed H-BBG20 scaffolds had the highest shape fidelity followed by H-BBG15 scaffolds. The stronger hydrogel network in these samples, characterized by reduced free volume and higher Young's modulus, contributed to increased viscosity and improved shear thinning behavior during the extrusion of the biomaterial ink, enhancing post-printing filament uniformity and scaffold shape fidelity. Also, as demonstrated in this research, modulating the concentration of BBG allows for control over the physical and mechanical characteristics of the biomaterial inks. The enhancement in mechanical integrity and shape fidelity of the hydrogel-BBG scaffolds along with the inherent bioactive properties positions BBG as a critical component in the development of advanced tissue constructs.

4. Conclusion

This study investigated the effect of BBG on physical properties and printability when incorporated into gelatin-alginate hydrogel biomaterial inks. Inks with higher BBG content showed higher density and viscosity. The addition of BBG enhanced the mechanical properties of 3D-printed hydrogels, evidenced by the increase in Young's modulus in samples with higher BBG contents. The temperature-dependent shear thinning behavior of the hydrogel biomaterial inks is improved by the addition of BBG, enabling better control over ink gelation and the printing process. The increased viscosity due to higher BBG content improves the hydrogel's printability as evidenced by improved uniformity in the printed filaments and enhanced shape fidelity in the printed scaffolds. Due to the higher viscosity, the printing process of hydrogel with more BBG requires higher extrusion pressure. These insights highlight the impact of BBG concentration on hydrogel viscosity and underscore the importance of optimizing temperature and pressure settings to achieve the desired extrusion characteristics. The quantitative assessments of printing outcomes indicated that hydrogel-BBG biomaterial inks with viscosity in the range of 4.5 – 6.5 Pa·s are desirable for extrusion-based 3D printing and that 15 – 20 wt% BBG concentrations in the hydrogels result in improved shape fidelity in the printing outcomes. This research highlights the ability of BBG to refine the capabilities of 3D bioprinting of hydrogels and suggests its significant role in advancing tissue engineering and regenerative medicine.

Acknowledgments

The authors extend their sincere gratitude to Drs. Douglass Bristow, Nathan Leigh, and Gregory Hilmas for their consultation advice and infrastructure support. Special thanks are extended to Jyothiswaroop Gowdappagari for his assistance in mechanical testing and to Abid Hasan Rafi and Lekhana Gurijala for their contributions to rheology testing. This work was funded by the Midwest Biomedical Accelerator Consortium (MBArC), an NIH Research Evaluation and Commercialization Hub (REACH) and by the Center for Biomedical Research.

Funding

This work was funded by the Midwest Biomedical Accelerator Consortium (MBArC), an NIH Research Evaluation and Commercialization Hub (REACH) and by the Center for Biomedical Research.

Conflict of interest

The authors declare they have no competing interests.

Author contributions

Conceptualization: All authors
Data curation: Fateme Fayyazbakhsh, Mehedi Hasan Tusar
Formal analysis: Fateme Fayyazbakhsh, Mehedi Hasan Tusar
Funding acquisition: Fateme Fayyazbakhsh, Ming C. Leu
Investigation: All authors
Methodology: Fateme Fayyazbakhsh, Yue-Wern Huang, Ming C. Leu
Project administration: Ming C. Leu
Writing – original draft: Fateme Fayyazbakhsh, Mehedi Hasan Tusar
Writing – review & editing: Yue-Wern Huang, Ming C. Leu

Ethics approval and consent to participate

Not applicable.

Consent for publication

Not applicable.

Availability of data

Data is available from the corresponding author upon reasonable request.

References

1. Theus AS, Ning L, Hwang B, *et al*. Bioprintability: Physiomechanical and biological requirements of materials for 3D bioprinting processes. *Polymers (Basel)*. 2020;12(10):2262.

   doi: 10.3390/polym12102262

2. Matai I, Kaur G, Seyedsalehi A, McClinton A, Laurencin CT. Progress in 3D bioprinting technology for tissue/organ regenerative engineering. *Biomaterials*. 2020;226:119536.

   doi: 10.1016/J.BIOMATERIALS.2019.119536

3. Groll J, Burdick JA, Cho DW, *et al*. A definition of bioinks and their distinction from biomaterial inks. *Biofabrication*. 2019;11(1):013001.

   doi: 10.1088/1758-5090/aaec52

4. Fatimi A, Okoro OV, Podstawczyk D, Siminska-Stanny J, Shavandi A. Natural hydrogel-based bio-inks for 3D bioprinting in tissue engineering: A review. *Gels*. 2022;8(3):179.

   doi: 10.3390/gels8030179

5. Mancha Sánchez E, Gómez-Blanco JC, López Nieto E, *et al*. Hydrogels for bioprinting: A systematic review of hydrogels synthesis, bioprinting parameters, and bioprinted structures behavior. *Front Bioeng Biotechnol*. 2020;8:776.

   doi: 10.3389/fbioe.2020.00776

6. Gillispie G, Prim P, Copus J, *et al*. Assessment methodologies for extrusion-based bioink printability. *Biofabrication*. 2020;12(2):022003.

   doi: 10.1088/1758-5090/ab6f0d

7. Fayyazbakhsh F, Leu MC. A brief review on 3D bioprinted skin substitutes. *Procedia Manuf*. 2020;48:790-796.

   doi: 10.1016/j.promfg.2020.05.115

8. Fayyazbakhsh F, Khayat MJ, Leu MC. 3D-printed gelatin-alginate hydrogel dressings for burn wound healing: A comprehensive study. *Int J Bioprint*. 2022;8(4):618.

   doi: 10.18063/ijb.v8i4.618

9. Mantha S, Pillai S, Khayambashi P, *et al*. Smart hydrogels in tissue engineering and regenerative medicine. *Materials* (*Basel*). 2019;12(20):3323.

   doi: 10.3390/MA12203323

10. Ho TC, Chang CC, Chan HP, *et al*. Hydrogels: Properties and applications in biomedicine. *Molecules*. 2022;27(9):2902.

    doi: 10.3390/MOLECULES27092902

11. El-Sherbiny IM, Yacoub MH. Hydrogel scaffolds for tissue engineering: Progress and challenges. *Glob Cardiol Sci Pract*. 2013;2013(3):316-342.

    doi: 10.5339/gcsp.2013.38

12. Lin X, Zhao X, Xu C, Wang L, Xia Y. Progress in the mechanical enhancement of hydrogels: Fabrication strategies and underlying mechanisms. *J Polym Sci*. 2022;60(17):2525-2542.

    doi: 10.1002/pol.20220154

13. Maciel BR, Baki K, Oelschlaeger C, Willenbacher N. The influence of rheological and wetting properties of hydrogel-based bio-inks on extrusion-based bioprinting. *Chem Ing Tech*. 2022;94(3):393-401.

    doi: 10.1002/cite.202100139

14. Unagolla JM, Jayasuriya AC. Hydrogel-based 3D bioprinting: A comprehensive review on cell-laden hydrogels, bioink formulations, and future perspectives. *Appl Mater Today*. 2020;18:100479.

    doi: 10.1016/j.apmt.2019.100479

15. Gillispie GJ, Copus J, Uzun-Per M, *et al*. The correlation between rheological properties and extrusion-based printability in bioink artifact quantification. *Mater Des*. 2023;233:112237.

    doi: 10.1016/j.matdes.2023.112237

16. Lee SC, Gillispie G, Prim P, Lee SJ. Physical and chemical factors influencing the printability of hydrogel-based extrusion bioinks. *Chem Rev*. 2020;120(19):10834-10886.

    doi: 10.1021/acs.chemrev.0c00015

17. He Y, Yang F, Zhao H, Gao Q, Xia B, Fu J. Research on the printability of hydrogels in 3D bioprinting. *Sci Rep*. 2016;6:29977.

    doi: 10.1038/srep29977

18. Mondal A, Gebeyehu A, Miranda M, *et al*. Characterization and printability of sodium alginate-Gelatin hydrogel for bioprinting NSCLC co-culture. *Sci Rep*. 2019;9(1):19914.

    doi: 10.1038/s41598-019-55034-9

19. Pepelanova I, Kruppa K, Scheper T, Lavrentieva A. Gelatin-methacryloyl (GelMA) hydrogels with defined degree of functionalization as a versatile toolkit for 3D Cell culture and extrusion bioprinting. *Bioengineering* (*Basel*). 2018;5(3):55.

    doi: 10.3390/BIOENGINEERING5030055

20. Schwab A, Levato R, D'Este M, Piluso S, Eglin D, Malda J. Printability and shape fidelity of bioinks in 3D bioprinting.

Chem Rev. 2020;120(19):11028-11055.

doi: 10.1021/acs.chemrev.0c00084

21. Fayyazbakhsh F, Khayat MJ, Sadler C, Day D, Huang YW, Leu MC. 3D-printed hydrogels dressings with bioactive borate glass for continuous hydration and treatment of second-degree burns. *Int J Bioprint*. 2023;9(6):0118.

doi: 10.36922/IJB.0118

22. Simorgh S, Alasvand N, Khodadadi M, *et al*. Additive manufacturing of bioactive glass biomaterials. *Methods*. 2022;208:75-91.

doi: 10.1016/J.YMETH.2022.10.010

23. Kolan KCR, Semon JA, Bromet B, Day DE, Leu MC. Bioprinting with human stem cell-laden alginate-gelatin bioink and bioactive glass for tissue engineering. *Int J Bioprint*. 2019;5(2.2):204.

doi: 10.18063/ijb.v5i2.2.204

24. Heid S, Boccaccini AR. Advancing bioinks for 3D bioprinting using reactive fillers: A review. *Acta Biomater*. 2020;113:1-22.

doi: 10.1016/j.actbio.2020.06.040

25. Herrada-Manchón H, Fernández MA, Aguilar E. Essential guide to hydrogel rheology in extrusion 3D printing: How to measure it and why it matters? *Gels*. 2023;9(7):517.

doi: 10.3390/GELS9070517

26. Han D, Lu Z, Chester SA, Lee H. Micro 3D printing of a temperature-responsive hydrogel using projection micro-stereolithography. *Sci Rep*. 2018;8(1):1963.

doi: 10.1038/s41598-018-20385-2

27. Fischer B, Schulz A, Gepp MM, Neubauer J, Gentile L, Zimmermann H. 3D printing of hydrogels in a temperature controlled environment with high spatial resolution. *Curr Dir Biomed Eng*. 2016;2(1):109-112.

doi: 10.1515/cdbme-2016-0027

28. Jo Y, Kim JY, Kim SY, *et al*. 3D-printable, highly conductive hybrid composites employing chemically-reinforced, complex dimensional fillers and thermoplastic triblock copolymers. *Nanoscale*. 2017;9(16):5072-5084.

doi: 10.1039/c6nr09610g

29. Julie Chandra CS, Sasi S, Bindu Sharmila TK. Material applications of gelatin. In: *Handbook of Biopolymers*. Singapore: Springer; 2023.

doi: 10.1007/978-981-16-6603-2_28-1

30. De Farias BS, Rizzi FZ, Ribeiro ES, *et al*. Influence of gelatin type on physicochemical properties of electrospun nanofibers. *Sci Rep*. 2023;13(1):15195.

doi: 10.1038/s41598-023-42472-9

31. Asim S, Tabish TA, Liaqat U, Ozbolat IT, Rizwan M. Advances in gelatin bioinks to optimize bioprinted cell functions. *Adv Healthc Mater*. 2023;12(17):2203148.

doi: 10.1002/adhm.202203148

32. Mu X, Agostinacchio F, Xiang N, *et al*. Recent advances in 3D printing with protein-based inks. *Prog Polym Sci*. 2021;115:101375.

doi: 10.1016/j.progpolymsci.2021.101375

33. Gregory T, Benhal P, Scutte A, *et al*. Rheological characterization of cell-laden alginate-gelatin hydrogels for 3D biofabrication. *J Mech Behav Biomed Mater*. 2022;136:105474.

doi: 10.1016/j.jmbbm.2022.105474

34. Abka-khajouei R, Tounsi L, Shahabi N, Patel AK, Abdelkafi S, Michaud P. Structures, properties and applications of alginates. *Mar Drugs*. 2022;20(6):364.

doi: 10.3390/md20060364

35. Axpe E, Oyen ML. Applications of alginate-based bioinks in 3D bioprinting. *Int J Mol Sci*. 2016;17(12):1976.

doi: 10.3390/ijms17121976

36. Piras CC, Smith DK. Multicomponent polysaccharide alginate-based bioinks. *J Mater Chem B*. 2020;8(36):8171-8188.

doi: 10.1039/d0tb01005g

37. Lou L, Rubinsky B. Temperature-controlled 3D cryoprinting inks made of mixtures of alginate and agar. *Gels*. 2023;9(9):689.

doi: 10.3390/gels9090689

38. Kolan KCR, Semon JA, Bindbeutel AT, Day DE, Leu MC. Bioprinting with bioactive glass loaded polylactic acid composite and human adipose stem cells. *Bioprinting*. 2020;18:e00075.

doi: 10.1016/j.bprint.2020.e00075

39. Kolan K, Liu Y, Baldridge J, *et al*. Solvent based 3D printing of biopolymer/bioactive glass composite and hydrogel for tissue engineering applications. *Procedia CIRP*. 2017;65:38-43.

doi: 10.1016/j.procir.2017.04.022

40. Caroline Murphy, Kolan K, Li W, Semon J, Day D, Leu M. 3D bioprinting of stem cells and polymer/bioactive glass composite scaffolds for bone tissue engineering. *Int J Bioprint*. 2017;3(1):005.

doi: 10.18063/IJB.2017.01.005

41. Zakeri Siavashani A, Haghbin Nazarpak M, Fayyazbakhsh F, Toliyat T, McInnes SJP, Solati-Hashjin M. Effect of amino-functionalization on insulin delivery and cell viability for two types of silica mesoporous structures. *J Mater Sci*. 2016;51(24):10897-10909.

doi: 10.1007/s10853-016-0301-1

42. Siavashani AZ, Nazarpak MH, Bakhsh FF, Toliyat T, Solati-Hashjin M. Preparation of mesoporous silica nanoparticles

for insulin drug delivery. *Adv Mat Res*. 2014;829:251-257.

doi: 10.4028/www.scientific.net/AMR.829.251

43. Mehrabi T, Mesgar AS, Mohammadi Z. Bioactive glasses: A promising therapeutic ion release strategy for enhancing wound healing. *ACS Biomater Sci Eng*. 2020;6(10):5399-5430.

doi: 10.1021/acsbiomaterials.0c00528

44. Solanki AK, Lali FV, Autefage H, *et al*. Bioactive glasses and electrospun composites that release cobalt to stimulate the HIF pathway for wound healing applications. *Biomater Res*. 2021;25(1):1.

doi: 10.1186/s40824-020-00202-6

45. Chen YH, Rao ZF, Liu YJ, *et al*. Multifunctional injectable hydrogel loaded with cerium-containing bioactive glass nanoparticles for diabetic wound healing. *Biomolecules*. 2021;11(5):702.

doi: 10.3390/biom11050702

46. Ege D, Zheng K, Boccaccini AR. Borate bioactive glasses (BBG): Bone regeneration, wound healing applications, and future directions. *ACS Appl Bio Mater*. 2022;5(8):3608-3622.

doi: 10.1021/acsabm.2c00384

47. Bi L, Rahaman MN, Day DE, *et al*. Effect of bioactive borate glass microstructure on bone regeneration, angiogenesis, and hydroxyapatite conversion in a rat calvarial defect model. *Acta Biomater*. 2013;9(8):8015-8026.

doi: 10.1016/j.actbio.2013.04.043

48. Lin Y, Brown RF, Jung SB, Day DE. Angiogenic effects of borate glass microfibers in a rodent model. *J Biomed Mater Res A*. 2014;102(12):4491-4499.

doi: 10.1002/jbm.a.35120

49. Zhao S, Li L, Wang H, *et al*. Wound dressings composed of copper-doped borate bioactive glass microfibers stimulate angiogenesis and heal full-thickness skin defects in a rodent model. *Biomaterials*. 2015;53:379-391.

doi: 10.1016/j.biomaterials.2015.02.112

50. Homaeigohar S, Li M, Boccaccini AR. Bioactive glass-based fibrous wound dressings. *Burns Trauma*. 2022;10:tkac038.

doi: 10.1093/burnst/tkac038

51. Ouyang L, Yao R, Zhao Y, Sun W. Effect of bioink properties on printability and cell viability for 3D bioplotting of embryonic stem cells. *Biofabrication*. 2016;8(3):035020.

doi: 10.1088/1758-5090/8/3/035020

52. Kyle S, Jessop ZM, Al-Sabah A, Whitaker IS. 'Printability' of candidate biomaterials for extrusion based 3D printing: State-of-the-art. *Adv Healthc Mater*. 2017;6(16):1700264.

doi: 10.1002/adhm.201700264

53. Cano-Vicent A, Tuñón-Molina A, Bakshi H, *et al*. Biocompatible alginate film crosslinked with Ca^{2+} and Zn^{2+} possesses antibacterial, antiviral, and anticancer activities. *ACS Omega*. 2023;8(27):24396-24405.

doi: 10.1021/acsomega.3c01935

54. Matyash M, Despang F, Ikonomidou C, Gelinsky M. Swelling and mechanical properties of alginate hydrogels with respect to promotion of neural growth. *Tissue Eng Part C Methods*. 2014;20(5):401-411.

doi: 10.1089/ten.tec.2013.0252

55. Pailler-Mattei C, Bec S, Zahouani H. *In vivo* measurements of the elastic mechanical properties of human skin by indentation tests. *Med Eng Phys*. 2008;30(5):599-606.

doi: 10.1016/j.medengphy.2007.06.011

56. Khalil S, Sun W. Biopolymer deposition for freeform fabrication of hydrogel tissue constructs. *Mater Sci Eng C*. 2007;27(3):469-478.

doi: 10.1016/j.msec.2006.05.023

57. Loebel C, Rodell CB, Chen MH, Burdick JA. Shear-thinning and self-healing hydrogels as injectable therapeutics and for 3D-printing. *Nat Protoc*. 2017;12(8):1521-1541.

doi: 10.1038/nprot.2017.053

Materials Science in Additive Manufacturing

Special Issue Alerts

Invitation for Special Issue Proposals

Organizing and editing for a Special Issue helps Guest Editors gain editorial experience and improve academic profile, in addition to being a part of organizing scientific communication of contemporary topics.

If you are published researcher and have an idea for a Special Issue, please write in via email to our Managing Editor (msam.office@accscience.sg). Please provide your CV, professional profile page and a topic of interest in your email. Our colleague will guide you in the process of writing a Special Issue proposal.

Frequently Asked Questions

1. **Are Special Issue submissions processed in the same way how Regular Issue papers are being pre-screened and reviewed?**
   Yes, all full-length article submissions to a Special Issue will go through the same editorial and peer-review process. The distinct difference here is that the Guest Editors will replace the usual editors and get involved in the making professional decisions on papers after peer review. Note that the specific roles of a Guest Editor could vary across Special Issues.

2. **How many Guest Editors are required to organize a Special Issue?**
   There is no fixed number; however, we suggest no more than 4 Guest Editors per Special Issue. More importantly, all Guest Editors should have excellent publication track records and demonstrated expertise in the topic(s) being proposed.

3. **Is the Special Issue governed by important deadlines?**
   Yes.

Benefits of Being A Guest Editor

- A chance to get involved in the conception and development of a specialty, contemporary topic that is of interest to the readers
- A chance to expand your professional network to the scholars and researchers who are similarly involved in the research of specialty topic
- A chance to hone your editorial skills
- A chance to gain first-hand experience of editing a thematic issue publication, which is a very valuable experience for those who aspire to edit their own journal in future
- A chance to improve your academic profile and help establish your academic influence within your discipline

Our Journals

International Journal of Bioprinting is an international journal covering the technology, science and clinical application of the broadly defined field of Bioprinting. Bioprinting is defined as the use of 3D printing technology with materials that incorporate viable living cells or biological elements to produce tissue or biotechnological products. We are interested in the scientific topics spanning all stages of bioprinting process from concept creation to fabrication and beyond. Knowledge generated in these researches must be related to bioprinting. *IJB* covers subject areas, including but not limited to the following:

- Information technologies and basic research
- Materials and formulation
- Cell source and biotechnology for additive manufacturing
- 3D Bioprinting technologies
- New design and fabrication paradigm
- Applied research purpose & evaluation of 3D printed products
- Associated social implications

International Journal of AI for Materials and Design is an international, peer-reviewed open-access journal that aims to bridge the cutting-edge research between AI and materials, AI and design. In recent years, the tremendous progress in AI is leading a radical shift of AI research from a mainly academic endeavor to a much broader field with increasing industrial and governmental investments. The maturation of AI technology brings about a step change in the scientific research of various domains, especially in the world of materials and design. Machine learning (ML) algorithms enable researchers to analyze extensive datasets on material properties and accurately predict their behavior in different conditions. This subsequently impact the industry to leverage on big data and advanced analytics to build scientific strategies, scale operational performance of processes and drive innovation. In addition, AI and ML are uniquely positioned to enable advanced manufacturing technologies across the value chain of different industries. Integration of multiple and complementary AI techniques, such as ML, search, reasoning, planning, and knowledge representation, will further accelerate advances in scientific discoveries, engineering excellence and the future of cyber-physical systems manufacturing.

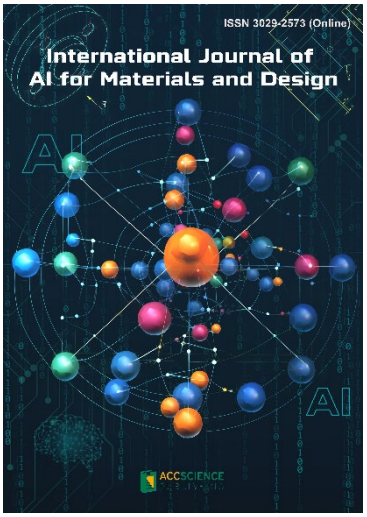

International Journal of AI for Materials and Design covers the following topics: AI or machine learning for material discovery, AI for process optimization, AI and data-driven approaches for product or systems design, application of AI in advanced manufacturing processes such as additive manufacturing, IoT, sensors, robotics, cloud-based manufacturing, intelligent manufacturing for various applications, autonomous experiments, material intelligence, energy intelligence, and AI-linked decarbonization technologies.

Start a new journal

Write to us via email if you are interested to start a new journal with AccScience Publishing. Please attach your CV, professional profile page and a brief pitch proposal in your email. We shall inform you of our decision whether we are interested to collaborate in starting a new journal.

Contact: info@accscience.com

https://accscience.com/journal/MSAM

Access Science Without Barriers

Contact

www.accscience.com
8 Burn Road, #15-03 Trivex, Singapore 369977
E-mail: editorial@accscience.com
Phone: +65 8182 1586